

Composition studies of Ultra High Energy Cosmic Rays using Data of the Pierre Auger Observatory

Zur Erlangung des akademischen Grades eines
DOKTORS DER NATURWISSENSCHAFTEN
von der Fakultät für Physik des
Karlsruher Institut für Technologie
(KIT)

genehmigte DISSERTATION

von Dipl.-Phys. Karen Salomé Caballero Mora
aus Mexiko D.F. (Mexiko)

Tag der mündlichen Prüfung: 16.04.2010
Referent: Prof. J. Blümer
Korreferent: Prof. G. Quast

*For my parents,
my sister
and my friends*

Abstract

The subject of this work is to estimate the mass composition of Ultra High Energy Cosmic Rays recorded by the surface detector of the Pierre Auger Observatory. The time traces of the surface detector stations are explored to obtain a new observable sensitive to the mass composition. This observable is based on the time it takes for the integrated signal recorded by each one of the stations of the surface detector, to rise from 10% to 50% of the final value, which is known as the risetime, $t_{1/2}$. The new observable, called Δ_{1000} is calculated for high quality hybrid events and calibrated with the most mass-sensitive observable recorded by the fluorescence detector, namely the depth of the shower maximum, X_{\max} . This is the depth in the atmosphere at which the maximum number of particles in the shower is reached. It is demonstrated that with this method one takes advantage of the high statistics provided by the surface detector (100% duty cycle) to obtain a new estimation for the depth of the shower maximum, X_{\max}^{SD} . The details of the calibration method, estimations of systematic uncertainties and discussions about fluctuations of the data are presented. Deductions on mass composition, based on comparisons with simulations are presented as well. The results on mass composition obtained by the fluorescence detector (around 13% duty cycle) are corroborated by the surface detector on average basis, pointing to an increase of the mass composition with the energy. Due to the large statistics of the surface detector, the energy range of the Observatory for measuring X_{\max} could be extended to energies of 80 EeV, i.e. by a factor of 2.3 with respect to the range reached with the analysis of fluorescence data. The mass composition corresponding to energies above $10^{19.6}$ eV is found to get heavier but still remains in a mixed mass composition.

Zusammenfassung

Bestimmung der Elementzusammensetzung der hochenergetischen kosmischen Strahlung mit dem Detektorfeld des Pierre Auger Observatoriums

Das Thema dieser Arbeit ist die Bestimmung der Elementzusammensetzung der hochenergetischen kosmischen Strahlung mit dem Detektorfeld des Pierre Auger Observatoriums. Die zeitliche Struktur der Detektorsignale wird untersucht um eine neue masseabhängige Observable zu definieren. Die Observable wird aus der sogenannten Anstiegszeit hergeleitet, die Zeit die das integrierte Signal braucht um von 10% bis 50% des Gesamtwertes zu steigen. Die neue Observable, Δ_{1000} , wird für qualitativ hochwertige Ereignisse berechnet. Daraufhin wird Δ_{1000} mit der Tiefe des Schauermaximums (X_{\max}) kalibriert. Die Tiefe des Schauermaximums ist definiert als die Tiefe in der Atmosphäre, wo die maximale Teilchenzahl des Luftschauers erreicht ist. X_{\max} ist die am stärksten massenabhängige Observable, die der Fluoreszenzdetektor messen kann. Die ausschließliche Verwendung von SD-Daten für eine neue Bestimmung des Schauermaximums X_{\max}^{SD} nutzt höhere Statistik, da die Betriebszeit nahezu 100% beträgt. Die Details der Kalibrierungsmethode sowie die Bestimmung der systematischen Unsicherheit und statistische Fluktuationen werden diskutiert. Die Elementzusammensetzung wird durch Vergleich mit Simulationen hergeleitet. Die vom SD bestimmte Elementzusammensetzung ist konsistent mit Ergebnissen aus FD-Messungen (ca. 13% Betriebszeit) und weist auf einen Anstieg der durchschnittlichen Masse mit zunehmender Energie hin. Aufgrund der hohen Statistik des Detektorfeldes wurde der Energiebereich der Messungen von X_{\max} bis 80 EeV ausgedehnt und somit um einen Faktor

2.3 höher als der Energiebereich, der durch die Analyse von FD-Daten erreicht wird. Die Analyse zeigt, dass die Primärmasse bei Energien über $10^{19.6}$ eV zunimmt, jedoch liegt in diesem Energiebereich weiterhin gemischte Massenzusammensetzung vor.

Resumen

Estudios de composición de Rayos Cósmicos Ultraenergéticos medidos con el detector de superficie del Observatorio Pierre Auger

El objetivo de este trabajo es estimar la composición de los Rayos Cósmicos Ultraenergéticos medidos con el detector de superficie del Observatorio Pierre Auger. Las trazas temporales del detector de superficie son investigadas para obtener una nueva observable sensitiva a la composición. Esta observable se basa en el tiempo que la señal integrada de cada estación del detector de superficie necesita para subir del 10% al 50% de su valor total, lo cual es conocido como el risetime, $t_{1/2}$. La nueva observable, llamada Δ_{1000} es calculada para eventos híbridos de alta calidad y calibrada con la observable más sensitiva a la composición medida con el detector de fluorescencia, la profundidad del máximo del chubasco, X_{\max} . Ésta se define como la profundidad en la atmósfera a la cual se alcanza el máximo número de partículas producidas en un chubasco. Se demuestra que con este método se puede aprovechar la enorme cantidad de datos proporcionados por el detector de superficie (100% de servicio activo) para obtener una nueva estimación de la profundidad del máximo del chubasco, X_{\max}^{SD} . Los detalles del método de calibración, estimaciones de las incertidumbres sistemáticas así como discusiones acerca de las fluctuaciones de los datos son presentados en este trabajo. Deducciones acerca de la composición basadas en comparaciones con simulaciones se presentan también. Los resultados acerca de composición obtenidos por el detector de fluorescencia (13% de servicio activo) son confirmados, en promedio, por el detector de superficie apuntando a un aumento de la masa con la energía. Debido a la enorme estadística del detector de superficie, el rango de medición para X_{\max} , alcanzado por el Observatorio podría extenderse a energías de 80 EeV, es decir, un factor de 2.3 con respecto del rango alcanzado con el análisis de datos de fluorescencia. Se encuentra que la composición correspondiente a energías sobre $10^{19.6}$ eV tiende a ser pesada pero aun permanece siendo una mezcla.

Contents

Introduction	1
1 Ultra high energy cosmic rays	3
1.1 A brief history of the study of cosmic rays	3
1.2 The energy spectrum of cosmic rays	4
1.3 Acceleration mechanisms and propagation of cosmic rays	7
1.4 Origin and source identification	8
1.5 Extensive air showers	10
1.6 Mass composition of cosmic rays	12
2 The Pierre Auger Observatory	17
2.1 Surface Detector	18
2.2 Fluorescence Detector	30
3 Studies of mass composition of ultra high energy cosmic rays with the Pierre Auger observatory	41
3.1 The depth of the shower maximum, X_{\max}	41
3.2 Ratio of muon to electromagnetic particles in the shower	44
3.3 The lateral development of the shower	45
3.4 Radius of curvature R_c	46
3.5 Time structure of the signal of air shower particles	46
4 The Risetime $t_{1/2}$, its uncertainty and asymmetry	53
4.1 Uncertainty of risetime $\sigma_{t_{1/2}}$	53
4.2 Asymmetry correction	62
4.3 Parameterisation of risetime	66
4.4 $t_{1/2}(1000 \text{ m})$ as a mass composition parameter	72

CONTENTS

5	Δ_{1000} as a mass composition sensitive parameter	77
5.1	Definition	77
5.2	Calibration of Δ_{1000} with X_{\max}	82
5.3	The SD depth of the shower maximum, X_{\max}^{SD}	86
5.4	Estimation of Uncertainties in X_{\max}^{SD}	89
6	Estimation of the mass composition of ultra high energy cosmic rays using Δ_{1000}	99
6.1	Determination of the mass composition of cosmic rays using the Elongation Rate, D_{10}	99
6.2	A Monte Carlo Study of Δ_{1000}	103
6.3	Determination of the mass composition of cosmic rays using $\langle \ln A \rangle$	109
6.4	Analysis on AGN correlated events	111
	Summary and conclusions	115
	Bibliography	119
	Acronyms	127
A	Validation of risetime results for data used in Δ_{1000} analysis	129
B	Information about simulated showers for studies of Δ_{1000} parameter	133
C	Comparison of results of $\langle \ln A \rangle$	135

Introduction

The discovery of cosmic rays at the end of 19th century opened a new subject in physics from which invaluable information about the most energetic particles coming from the space can be obtained. There is a feedback between physics of cosmic rays and particle physics to try to understand the mechanisms of their interactions with matter and at the same time giving the possibility to develop the fundamental theories of physics from its macroscopic and microscopic perspective, respectively. The origin and production mechanisms of cosmic rays above 10^{18} eV, the so called Ultra High Energy Cosmic Rays (UHECRs), is still unknown. Information about the nature of the cosmic rays, i.e. the mass composition, constitutes one of the characteristics that can help to understand the processes that create them. It might also allow to constrain the sources of such kind of cosmic rays as well as to have a properly interpretation of the energy spectrum. However, mass composition studies at such high energies are difficult due to the low flux of cosmic rays observed, which is about $1 - 100 \text{ km}^{-2} \text{ century}^{-1}$. Moreover, even the most recent accelerators built in the earth, such as the Tevatron [1] or the Large Hadron Collider (LHC) [2] reach only center of mass energies of the order of 1-10 TeV, making the development of interaction models at higher energies uncertain. High technological requirements are needed to collect reasonably good statistics from arriving cosmic rays with that low flux. An effective area of thousands of square kilometers is necessary. Those requirements are now available for the first time using the advantages of the Pierre Auger Observatory. This is a hybrid detector, consisting on an area of 3000 km^2 and two kind of detectors, fluorescence telescopes (fluorescence detector, FD) and water Cherenkov stations (surface detector, SD). Studies on mass composition of UHECRs using mass-sensitive observables from both kind of detectors are presented in this work.

The time traces of the surface detector are analysed to define a new mass-sensitive observable called Δ_{1000} . This is based on a feature of the time trace called risetime, $t_{1/2}$, which is the time it takes for the integrated signal to rise from 10% to 50% of the final value. The characterization of Δ_{1000} and all necessary treatments of the time trace to define it such as the parameterisation of a measurement uncertainty, $\sigma_{1/2}$, the correction of the azimuthal asymmetry and a reliable parameterisation of $t_{1/2}$ as a function of the distance of the station from the shower core, are performed.

The parameter Δ_{1000} is calibrated with the depth of the shower maximum, X_{max} , which is measured with the fluorescence detector and is the most mass-sensitive parameter available in the Pierre Auger Observatory. The goal is to obtain an estimation of this from SD measurements, $X_{\text{max}}^{\text{SD}}$. The advantage of this method lies on the high statistics available from the SD (100% duty cycle), in comparison with the one from the FD (around 13% duty

CONTENTS

cycle). That means that similar results on mass composition obtained already from studies with FD can be reproduced with high statistics. Specially comparisons with the results on the rate of change of X_{\max} with the energy, the elongation rate, D_{10} , reported by the Pierre Auger Collaboration in Ref. [3] are presented.

Studies about fluctuations of Δ_{1000} to estimate the uncertainties in X_{\max}^{SD} as well as estimations of systematics coming from the calibration procedure, for understanding the reliability of X_{\max}^{SD} on an event-by-event basis, are performed. The uncertainties from the calibration procedure are also estimated by using Monte Carlo simulations for testing the effectiveness of the Δ_{1000} method to reproduce X_{\max}^{MC} , which is the value given by the simulations. The corresponding results of X_{\max}^{SD} are compared with predictions of different hadronic interaction models.

Once the X_{\max}^{SD} parameter is obtained, the mass composition of cosmic rays of energies above 3 EeV, the energy at which the SD reaches the full efficiency, is determined by using the new observable. For this purpose, the corresponding D_{10} , and the mean logarithmic mass, $\langle \ln A \rangle$, are calculated and considered in the same sense as they are when the usual X_{\max} observable is used.

The method proposed in this work gives the possibility to have a value for X_{\max} for measured events even if they are not hybrid. In this sense, the highest energy cosmic rays used by the Pierre Auger Collaboration for studies of anisotropy of their arrival direction, which demonstrates their extragalactic origin reported in Ref. [4], are analysed. Deductions about their mass composition are made.

Chapter 1

Ultra high energy cosmic rays

Cosmic rays are particles with energies between 10^9 and 10^{20} eV that reach the Earth from interstellar space. Most of them consist of fully charged nuclei and protons plus a steady flux of electrons, gammas and anti-matter [5]. The nature of cosmic rays above 10^{15} eV is nevertheless still not well known, especially the origin and production mechanisms above 10^{18} eV. In this chapter the main characteristics of UHECRs and the relevance of studies on mass composition are described.

1.1 A brief history of the study of cosmic rays

The discovery of cosmic rays is the result of observations made by Charles Wilson at the end of 19th century [6–8]. Wilson observed that electroscopes lost charge without any apparent reason. Trying to explain that effect, Wulf developed the ionization chamber [6–8], which was used by Victor Hess in 1912 to measure the increase or decrease of the radiation which should cause the ionization, at different heights. He concluded that such radiation should come from the space [9]. In 1913 and 1914 Werner Kohlhörster and Walther Bothe found that at heights of 9300 m the effects were fifty times greater than on the ground [6–8]. From 1923 to 1926 Robert Andrew Millikan and his collaborators made measurements also under the water corroborating that the origin of the radiation was extraterrestrial. Millikan gave to that radiation the name "cosmic rays" [10]. In 1927 Skobelczyn found that trajectories produced by gamma rays behave like cosmic rays [11]. Meanwhile Kohlhörster and Bothe measured in 1929 a flux of atomic and subatomic particles using coincidences between two Geiger Müller counters. That flux explained the effects of the high energy radiation. Bothe established in 1930 in Postdam the first research center dedicated to cosmic rays. A latitudinal effect on the flux was also observed, because particles with low energies were not detected near to the equator [6–8]. In 1930 A. H. Compton and collaborators confirmed the latitudinal [12] effect (already observed also by Clay in 1927 [13]), which was directly correlated with the geomagnetic latitude. C. Störmer considered the Earth as a magnetic dipole and studied trajectories of charged particles. He was able to set areas for each point on the Earth, where it was not possible to measure a great amount of cosmic rays with positive charge (from the East), and others where the cosmic rays with negative charge were limited (from the West) [6–8]. His study was complemented with calculations made by Manuel Sandoval Vallarta in

Mexico, O. Lemaitre in Belgium, and with measurements made by Luis Álvarez in Mexico City [6–8]. In 1938 Pierre Auger made measurements on the Alps, he observed that detectors which were separated large distances from each other, registered particles at the same time. He concluded that there were showers of secondary particles produced by the interaction of primary particles with the molecules of the atmosphere. The primary particles should have energies of the order of 10^{15} eV to be able to produce such extensive air showers [14]. After the discovery of new particles, it was possible to continue identifying them as cosmic rays, as for example with the muon μ . The nature of the low energy radiation arriving at the Earth was determined at the end of the forties, using photographic emulsions at large heights. It was found that the primary particles consist of protons, α particles and heavier nuclei. Measurements of particle interactions made in accelerators has been very important to develop models which can be compared with measurements of cosmic rays, but for UHECRs there are not yet such kind of measurements available, maybe the expected data from the Large Hadron Collider (LHC) can help to extrapolate more accurately the current models to higher energies. The cosmic ray spectrum of energies between $3 \cdot 10^{15}$ and 10^{18} eV was determined during the years 1954 and 1957 with an experiment of 0.9 m^2 at Harvard Agassiz [15]. For studying the origin of cosmic rays with energies of 10^{17} eV an observatory with scintillator detectors was built by Bruno Rossi's group at the Massachusetts Institute of Technology [16]. Later, in 1960, an array of 19 scintillators with an area of 3.3 m^2 arranged on a 884 m grid was built at Volcano Ranch, New Mexico, directed by David Linsley. With this array it was possible to conclude that cosmic radiation at these energies is isotropic. Also in 1962 a cosmic ray of 10^{20} eV was detected [16]. From that discovery on, arrays with areas of more than 8 km^2 were built. Some of them are Haverah Park (England, 12 km^2 , water Cherenkov tanks), Yakutsk (Russia, 18 km^2 , scintillators, atmospheric Cherenkov detectors, muon counters) and AGASA (Japan, 100 km^2 , scintillators, muon counters). In 1966 it was predicted a cut-off in the flux of cosmic rays at energies greater than $5 \cdot 10^{19}$ eV [17, 18]. This prediction was set by Keneth Greisen, Valdem Kuz'min and Georgi Zatsepin and is known as the "GZK cut-off". Studies on that demand the necessity of new measurement techniques. Suga and Chudakov suggested the possibility of using the atmosphere as an enormous scintillator. In 1976, at Volcano Ranch, rudimentary fluorescence detectors were used. After that the Fly's Eye experiment was built in the USA, which used fluorescence detectors too. This array measured very high energetic events ($3 \cdot 10^{20}$ eV). In 1994 also AGASA and Yakutsk measured events with energies of $2 \cdot 10^{20}$ eV [6–8]. Another example of experiments using high resolution fluorescence detectors is HiRes in Utah [19]. The combination of both, fluorescence and surface detectors set on a big area, is now being used by the Pierre Auger Observatory [20]. Its hybrid condition allows to obtain almost model-independent data and to dispose of a large aperture in comparison with previous experiments.

1.2 The energy spectrum of cosmic rays

The energy spectrum of cosmic rays shows the flux, J , of particles as a function of energy, as it is observed on Earth. It extends from the solar cosmic rays scale of a few GeV to above 10^{20} eV. Acceleration mechanism together with propagation processes through the interstellar medium can explain qualitatively the whole energy range but the acceleration sites are still to be explained. The energy spectrum has some features which are easily distinguishable because of its similarity with a human leg, the knee and the ankle. Those features might be interpreted

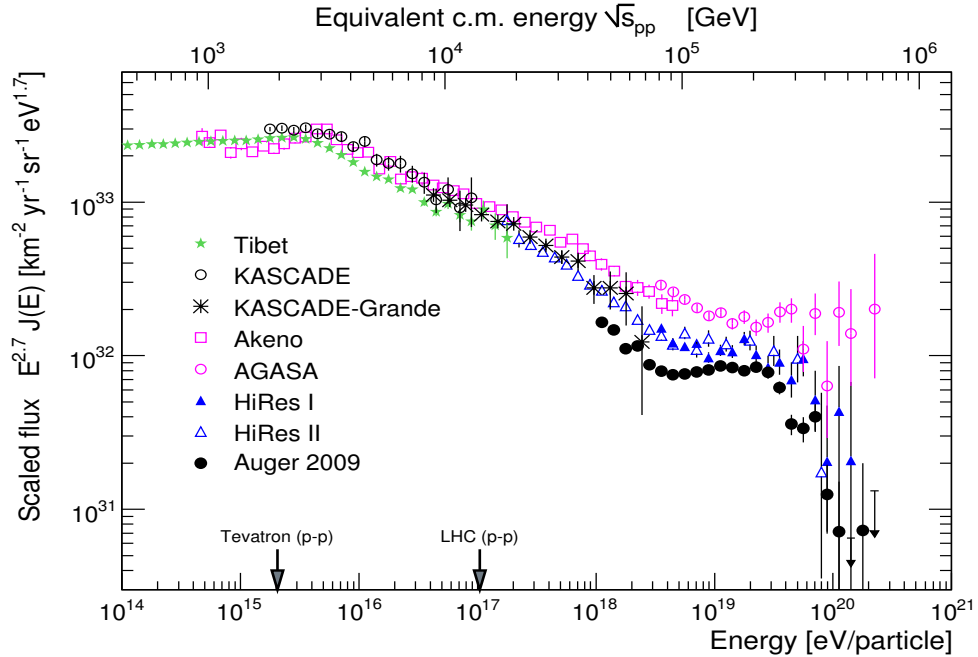


Figure 1.1: Cosmic ray energy spectrum as measured by many experiments over a wide range in energy. The lower axis reflects the energy of the primary cosmic ray nuclei E_{lab} , the upper axis denotes the corresponding center-of-mass energy per nucleon and some typical energies, which can be accessed by accelerators, are emphasized [21].

either as a change of the acceleration mechanism at sources, as a propagation effect or as a change of the hadronic interaction cross sections with increasing energy. Figure 1.1 shows the spectrum multiplied by $E^{2.7}$ to remove the enormous slope over 15 orders in magnitude of the flux and to point out the changes of the spectral index (γ), which are identified with the different features observed. At lower energies the flux is well described by $J \propto E^{-2.7}$ and appears flat. The visible changes and the highest energy region are described in the next paragraphs.

The knee It is observed at about $3 \cdot 10^{15}$ eV [22] where the power-law slope changes from $\gamma \simeq 2.7$ to $\gamma \simeq 3.0$. It is considered that cosmic rays with energies below the knee are accelerated through diffusive shock acceleration in expanding supernova remnants (SNRs) located within our galaxy [23]. There is also a coincidence of the knee with a rapid increase of the mean primary mass. The knee is thus explained to be caused by the galactic cosmic ray accelerators reaching their maximum energy, or also to be due to the limitation of the galactic magnetic fields to confine the nuclei in the Galaxy when they reach a given energy. Since acceleration depends on the charge of particles Z , the knee energy is also proportional to it. Another concurrent scenario assumes that the knee might be caused by a sudden change of the hadronic interactions at these energies [24,25]. In this case the energy of the knee for individual elements would scale with their mass number A and not with Z . The knee can be interpreted also as a propagation result due to a change in the regime of diffusion in the galactic magnetic field [26,27]. The Karlsruhe Shower Core and Array DEtector (KASCADE)

experiment has studied the knee region obtaining energy spectra for different primary mass groups (proton, helium and CNO) and showing that the position of the individual knees is shifted to higher energies with increasing atomic number and giving a big support for those scenarios [28]. This also supports the idea of cosmic rays of this region having a galactic origin.

A second discontinuity has been observed at energies around $4 \cdot 10^{17}$ eV and $6 \cdot 10^{17}$ eV [29–32], the *second knee*, where the spectral index turns to $\gamma \simeq 3.3$. KASCADE-Grande and IceTop [33] experiments will clarify this energy range of the cosmic ray flux in the near future.

It is expected that in the region between the knee and the ankle there is a drop of the heavy components at an energy scaled with the charge or with the mass and a transition region from the galactic to extra-galactic origin of cosmic rays.

The ankle It is observed at around 10^{18} eV [34], where the spectral slope turns again to $\gamma \simeq 2.7$. There are several theories trying to explain this feature. One of them assumes that at these energies a transition from the galactic to extra-galactic origin of the cosmic rays occurs [35–37]. The extra-galactic component is expected to have a pure proton composition. The position of the ankle would be the energy where the two components contribute equally to the total flux. The ankle can also be explained considering that the tail of the flux has a mixed composition and the ankle is still a transition region (Fig. 1.2(a)) [38, 39]. Nuclei with energies greater than 10^{19} eV are disintegrated while they are propagating through the medium. The ankle can also be explained by the hypothesis that the extra-galactic component composed mainly of protons starts to dominate at lower energies. Thus, in this model, the transition from galactic to extra-galactic origin occurs at lower energies than the ankle, where there is no more galactic component (Fig. 1.2(b)) [40, 41]. Protons propagate through the *cosmic microwave background* (CMB) over extra-galactic distances and loose energy due to the Bethe-Heitler e^+e^- pair production. The resulting flux suppression at higher energies is identified with the ankle. This is known as the *dip model*.

Region of ultra-high energies At the end of the spectrum, the flux of cosmic rays decreases to about $1 - 100 \text{ km}^{-2} \text{ century}^{-1}$. This cut-off was already predicted after the discovery of the CMB. It is known as the “GZK cut-off” after the original authors [17, 18]. The prediction explains that ultra-high energy nucleons ($E \gtrsim 50 \text{ EeV}$) traveling through extra-galactic space interact with photons of the CMB photon field via the formation of resonances (i.e. $N + \gamma_{CMB} \rightarrow \Delta \rightarrow N + \pi$), which leads to the emission of pions. This effect corresponds to an energy loss via pion emission, leading to a strong flux suppression above about 50 EeV (Fig. 1.3). Due to the lack of statistics in this region, it was not possible to confirm the observation of the cut-off for many years [42, 43]. Nevertheless, from recent results of the HiRes [44] and Auger [45] experiments show that a GZK-like feature can now be clearly identified within the corresponding spectra (Fig. 1.1). However, it is still not clear, whether the observed flux suppression is entirely due to the GZK-effect. Another plausible explanation of the cut-off at ultra-high energies is that the extra-galactic cosmic ray accelerators run out of power.

1.3 Acceleration mechanisms and propagation of cosmic rays

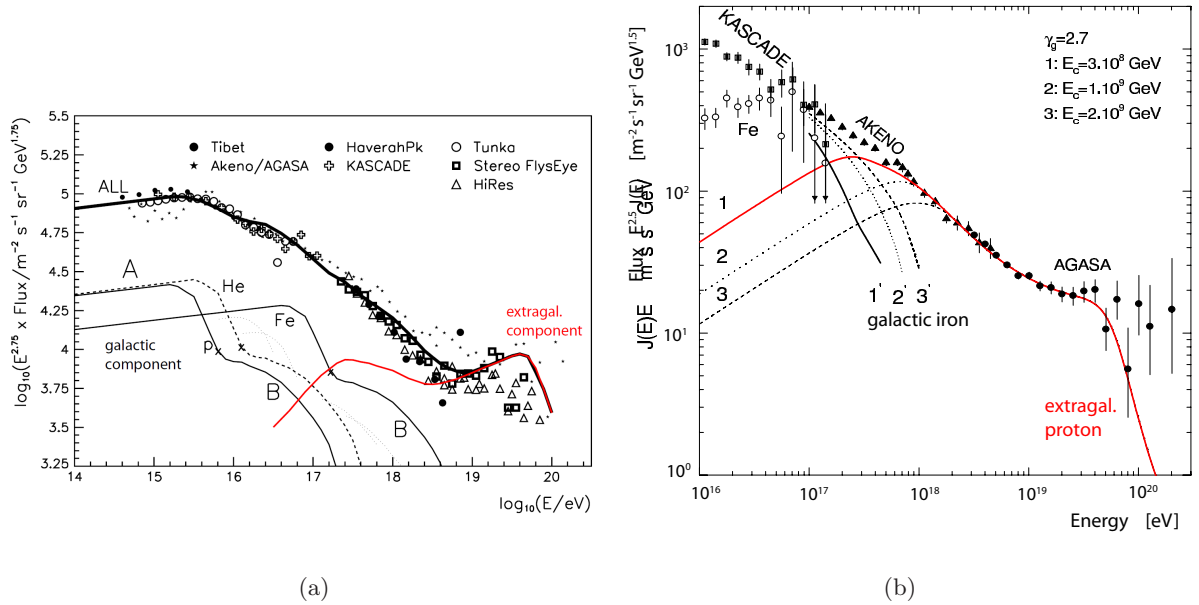


Figure 1.2: (a) The extra-galactic mixed composition scenario (taken from [35] and modified). (b) The dip model taken from [40].

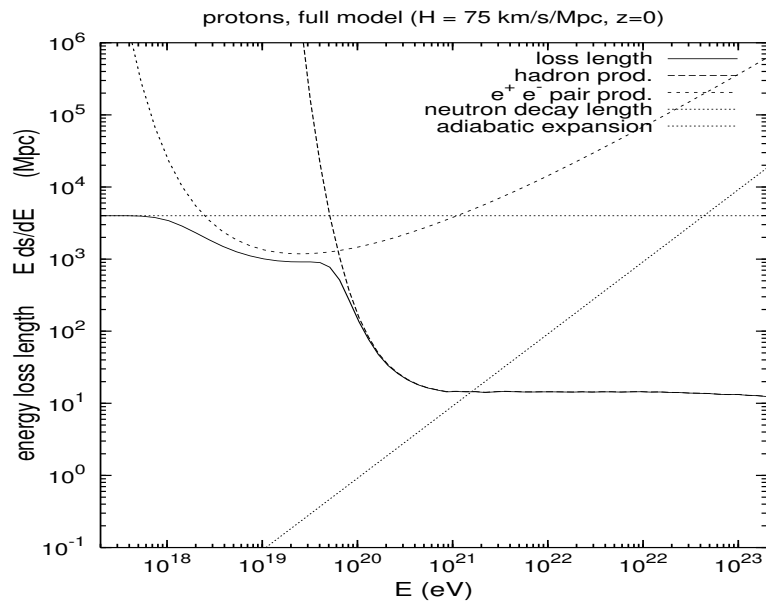


Figure 1.3: Energy loss length for extra-galactic cosmic ray propagation [46].

1.3 Acceleration mechanisms and propagation of cosmic rays

Acceleration of cosmic rays is usually explained with the first-order Fermi acceleration, also known as Diffusive Shock Acceleration (DSA), in shocks produced by astrophysical objects.

This mechanism was first proposed in the 1970s [47], based on the original work developed by Enrico Fermi in 1949 [48]. It demonstrated that particles gain energy stochastically when they pass through a magnetic cloud. On average, cosmic rays gain energy with an efficiency proportional to β ($\beta = u/c$, u = shock velocity). If encounters of particles with shock fronts are considered, particles are diffusively accelerated while they cross and then re-cross the shock front many times, due to the deflection of charged particles by magnetic anomalies. DSA is an extremely efficient mechanism for accelerating cosmic rays because up to 10% of the shock energy is transferred to the particles. The maximum energy attainable by a particle due to this process is given by [49, 50]:

$$E_{\max} = kZeB\beta_s R \quad (1.1)$$

where E is in eV, Z is the atomic number of the nucleus, e is the electron charge, B is the magnetic field strength in the region of the shock, β_s is the velocity of the shock front through the interstellar medium, $k < 1$ and R is the size of the shock region. From this mechanism, particles emerge out with a characteristic power-law spectrum [51, 52].

Propagation of cosmic ray through space is affected by several interaction processes. One of them is the already mentioned GZK-effect which produces a suppression of the flux of cosmic rays above energies around $5 \cdot 10^{19}$ eV.

Protons also interact with the CMB through pair production with an energy threshold of about 10^{18} eV ($p + \gamma_{\text{CMB}} \rightarrow p + e^+ + e^-$), this interaction is thought to be the dominating process in the region between the second knee and the ankle (Fig. 1.3).

Heavy nuclei also interact with CMB and intergalactic Infrared Background Radiation (IBR) through photo-disintegration and pair production with similar energy thresholds ($N^A + \gamma_{\text{CMB}} \rightarrow N^{(A-1)} + n$ or $N^A + e^+ + e^-$) [50, 53, 54].

Cosmic rays are also affected by both, galactic and extra-galactic magnetic fields, which bend their trajectories. These could pass from diffusive to rectilinear propagating [55]. Quantitative estimations of the deflection angles are not yet possible due to the limited knowledge of the strength of magnetic fields, the charge of UHECRs and the location of the sources.

1.4 Origin and source identification

Cosmic rays with energies up to some GeV arise predominantly from the Sun since, for instance, characteristic night-day variations are presented in the spectrum. From these energies up to a few 10^{15} eV cosmic rays could be originated by shock acceleration in galactic SNRs [56, 57]. Although there is no experimental evidence, some theories point out that SNRs could accelerate cosmic rays up to energies of 10^{18} eV as well [26, 58].

The maximum energy that cosmic ray may obtain from a given astronomical object is limited by the combination of the magnetic field strength and shock size. On this basis and considering equation 1.1, M. Hillas proposed a simple plot (Fig. 1.4) to show that there are only few astrophysical objects (AGNs and Gamma-ray bursts) capable to accelerate nuclei and protons to energies of 10^{20} eV. There are other non-traditional theories trying to explain the origin of the extreme energetic particles, the so called *top-down* models. Some of those models include production of UHECRs from the decay of exotic particles such as Topological Defects

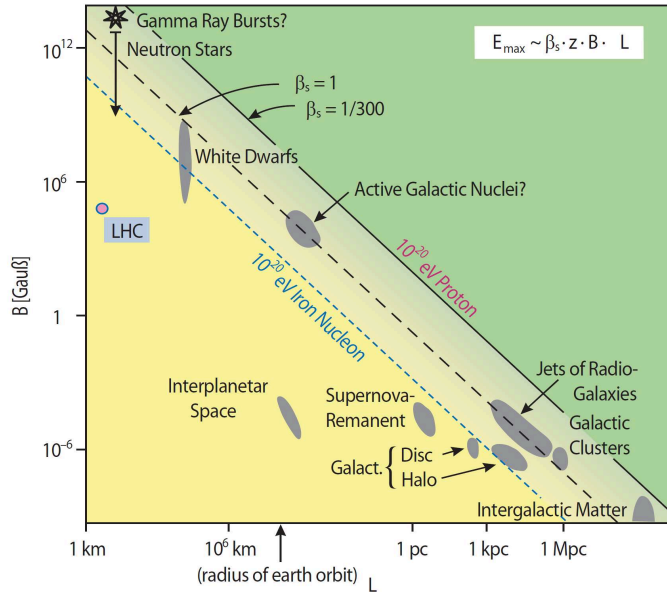


Figure 1.4: Hillas Plot showing the required size and magnetic field strength of possible UHECR sources. Objects below the corresponding lines are not able to accelerate proton or iron nuclei to an energy of 10^{20} eV [68].

(TD) [59], super heavy dark matter (SHDM) particles [60–62], or neutrino interactions with the relic neutrino background (Z-burst model) [63, 64]. All the top-down models suggest a large fraction of photons in the flux of UHECRs [65], which can be studied measuring the flux limits for photons and neutrinos. The Pierre Auger Collaboration has estimated upper limits on both of them [66, 67]. The upper limit set to the flux of photons allowed to constrain certain top-down models, which can not be considered as plausible scenarios for the production of UHECRs any more. However, neutrino flux is difficult to be measured due to the low cross section of neutrino.

The GZK effect also imposes a limit for the distance at which the sources of cosmic rays above energies of $5 \cdot 10^{19}$ eV can be located. For instance, sources of protons observed with an energy of 10^{20} eV are not expected to be located at distances larger than 50 Mpc (Fig. 1.5). Identification of sources of UHECRs by looking directly at their arrival directions is not easy because at relative low energies, the distribution of the arrival directions is isotropic. This is due to the effect of the galactic magnetic field. Nevertheless, a lot of effort has been concentrated to find significant anisotropies, which could help to correlate the flux of UHECRs with a known astrophysical object. Recently, the Pierre Auger Collaboration has reported a correlation between the arrival direction of cosmic rays with energies above 57 EeV and the position of active galactic nuclei (AGNs) lying within ~ 75 Mpc [4, 70]. This result is compatible with a scenario where UHECRs are accelerated in nearby extra-galactic sources, AGNs or other objects distributed similarly.

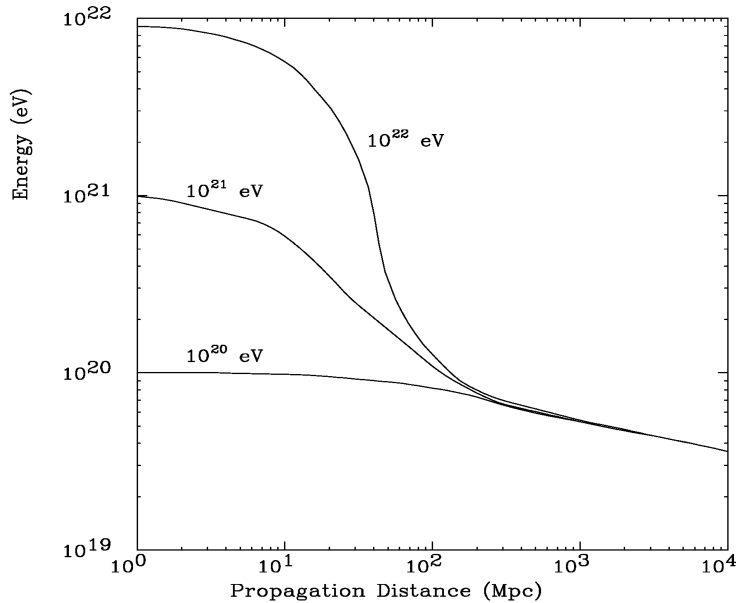
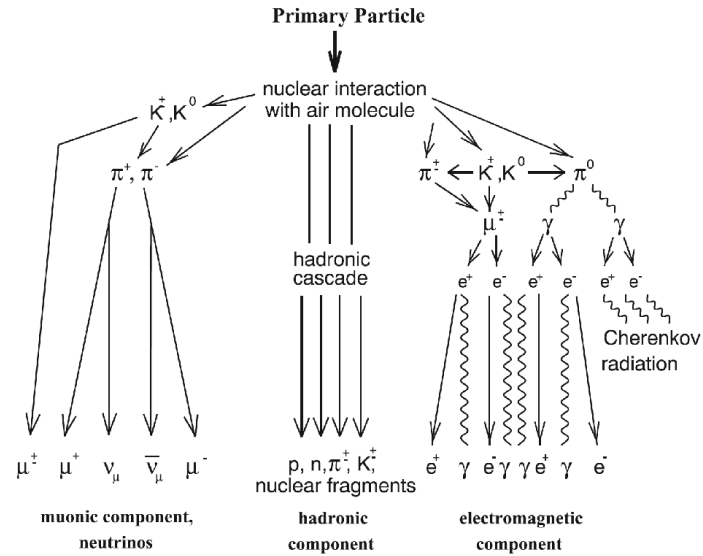


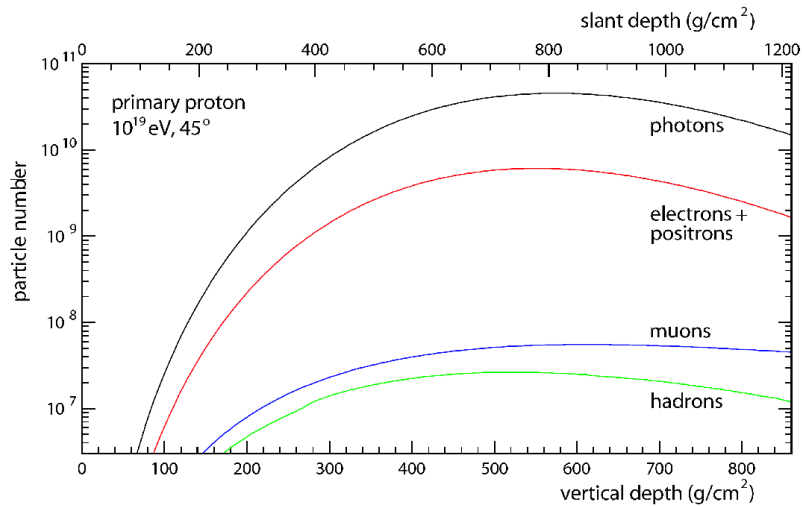
Figure 1.5: Three different initial energies of a proton as a function of the propagation distance through the CMB [69].

1.5 Extensive air showers

An extensive air shower (EAS) is a cascade of particles generated by a single high energy primary cosmic ray which interacts with the molecules of the air at about 10 km. The production of secondary particles reaches a maximum and continues after the total energy of the primary cosmic ray is distributed to them. Thus, the number of particles reaching the threshold for further particle production attenuates [71]. A cosmic ray induced EAS has three main components: *hadronic*, *muonic* and *electromagnetic* (Fig. 1.6(a)). In addition, there are particles whose contribution to the total energy balance is not big, i.e. *UV-photons* (fluorescence and Cherenkov) and *radio emission*, or which are not detectable and are therefore called *invisible component* (neutrinos and very low energy particles) [72]. **Hadronic** particles (nucleons and other high energy hadrons) stay close to the shower axis, which is the direction of motion of the primary cosmic ray particle. After a few hadronic interactions, most of the hadronic energy is transferred into the electromagnetic and muonic shower parts. Since the hadronic shower core is long lived and therefore propagates deep into the atmosphere, it acts as a permanent source of new electromagnetic particles and muons. **Muonic** component is generated by the decay of lower energy charged pions and kaons. Only about 10% of the charged particles in an extensive air shower are muons [73]. They hardly interact and lose energy slowly due mainly to ionization, being highly penetrating particles. Only lower energy muons may decay before they reach the detection level. **Electromagnetic** particles are produced primarily by photons from decay of neutral pions and eta particles. At each hadronic interaction, slightly more than a third of the energy goes into the electromagnetic component, this is the most abundant in the shower and carries the largest fraction of the total energy (Fig. 1.6(b)). The electromagnetic shower develops fast, mainly by bremsstrahlung interactions and pair production. Below a certain energy E_{crit} , ionization energy losses start



(a)



(b)

Figure 1.6: (a) Schema of the processes involved in the development of an EAS. (b) Average number of particles for a proton shower of $E_{\text{prim}} = 10^{19} \text{ eV}$, for the different components [74].

to dominate over new particle production and the shower is absorbed by the atmosphere.

The development of a cascade can be described schematically using the Heitler model. It describes the production of particles in a purely electromagnetic cascade considering a branching of particles (e^- , e^+ and γ) or packets of energy (see Fig. 1.7(a)). The branching occurs due to a splitting process after an interaction length

$$\lambda = X_0 \ln 2. \quad (1.2)$$

Chapter 1. Ultra high energy cosmic rays

The energy of the initial particle is thus distributed equally onto the two interaction products. The total number of particles doubles after every λ and the total energy E_0 is subdivided equally onto the particles of the cascade

$$N_n = 2^n \text{ and } E_n = E_0/2^n. \quad (1.3)$$

Once the energy per particle drops below the critical energy E_{crit} (85 MeV in air), the production of new particles stops and the remaining energy is lost by ionization (collisional energy loss). At this point the cascade reaches its maximum of number of particles and suddenly dies out:

$$N_{\text{max}} = E_0/E_{\text{crit}} \text{ and } X_{\text{max}} = X_0 \ln \frac{E_0}{E_{\text{crit}}} \propto \ln E_0. \quad (1.4)$$

Some detailed calculations [75] show that X_0 can be identified with the electromagnetic radiation length (X_{rad}), which depends on the medium in which the shower develops and is 36 to 37 gcm^{-2} in air.

The Heitler model can also be extended to hadronic cascades (Fig. 1.7(b)) in this case, the hadronic interaction length $\lambda_I = X_I \ln 2$, with $X_I \approx 120 \text{ gcm}^{-2}$ for pions in air, is introduced in analogy to the electromagnetic interaction length λ . In each hadronic interaction N_{mult} particles are produced, of which one third are π^0 and two thirds are π^\pm . The neutral pions decay instantly into two photons, initiating an electromagnetic cascade. The hadronic cascade stops when pions drop below their critical energy, then they decay yielding muons. The critical energy for pions E_{crit}^I in air depends on the interaction length, the atmospheric density and the pion decay length, its approximated value is 20 GeV [76]. The total number of produced muons is identical with the number of π^\pm at their critical energy:

$$N_\mu = N_{\pi^\pm} = \left(\frac{2}{3}N_{\text{mult}}\right)^{n_c} = \left(\frac{E_0}{E_{\text{crit}}^I}\right)^\beta \text{ with } n_c = \frac{1}{\ln N_{\text{mult}}} \ln \frac{E_0}{E_{\text{crit}}^I}, \quad (1.5)$$

where $\beta = \ln\left(\frac{2}{3}N_{\text{mult}}\right) / \ln(N_{\text{mult}}) \approx 0.9$. For the hadronic Heitler model, only the electromagnetic showers induced by the first generation of π^\pm are taken into account. It could result in an underestimation of the real X_{max} . This approach also neglects the significant effect of inelasticity in hadronic interactions, which leads to a not equitable energy distribution on the secondary particles, in contradiction with the original assumption. However, there is no simple analytic way to get the result from this complex superposition of cascades. Furthermore, the hadronic interactions related to the main observables of cascades are still not well known at the energies of EAS. Models of cascades have to be improved.

1.6 Mass composition of cosmic rays

As mentioned in the introduction, the origin and production mechanisms of UHECRs are still not well understood. An in-depth knowledge of the mass composition of cosmic rays can give an important clue for the processes that create the highest energy particles in nature. It might allow to constrain the sources of UHECRs as well as having a properly interpretation of the energy spectrum.

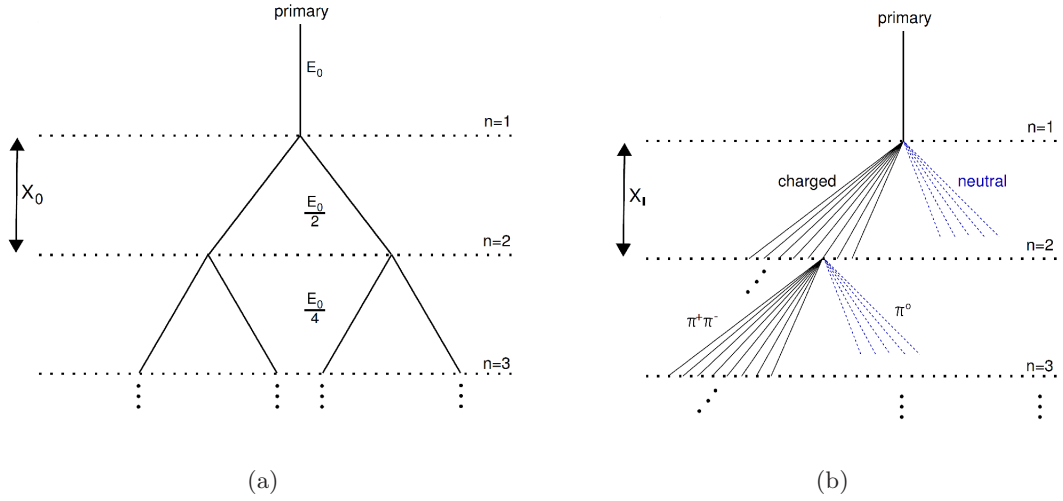


Figure 1.7: (a) Heitler model for electromagnetic cascades. (b) Extended Heitler model for hadronic cascades [72].

The abundance of individual elements has been measured with detectors above the atmosphere at energies below 10^{14} eV, at higher energies it is at the moment not possible due to the low flux and the large fluctuations in the development of the extensive air showers. An often-used quantity to characterize the composition is the **mean logarithmic mass**, defined as $\langle \ln A \rangle = \sum_i r_i \ln A_i$ where r_i is the relative fraction of nuclei of mass A_i . There are two methods to obtain experimentally $\langle \ln A \rangle$: (i) using its proportionality to the ratio of number of electrons and muons registered at ground level $\langle \ln A \rangle \propto \log_{10}(N_e/N_\mu)$ and (ii) using its proportionality to the observed depth of the shower maximum $\langle X_{\max} \rangle_A = D_p \ln(E/A) = \langle X_{\max} \rangle_p - D_p \ln A$ (see Chapter 3). Hence, the maximum of an iron induced shower (X_{\max}^{Fe}) should be about 150 gcm^{-2} higher in the atmosphere than the one induced by a proton (X_{\max}^p). Figure 1.8 shows a compilation of measurements compared with predictions of $\langle X_{\max} \rangle$ for protons and iron nuclei from different experiments and interaction models. Below $4 \cdot 10^{15}$ eV, values obtained by different experiments exhibit a common trend, they seem to increase faster as function of energy than the simulations, which implies that the average composition would become lighter. Above the knee, measured values become flat up to around $4 \cdot 10^{16}$ eV, indicating an increase of the average mass in this energy range. Finally, above $4 \cdot 10^{16}$ eV, measured data show an almost constant slope for X_{\max} as function of energy. Knowing the average depth of the shower maximum for protons and iron nuclei from simulations, the mean logarithmic mass is derived in the superposition model of air showers from the measured X_{\max}^{meas} values using the relation $\langle \ln A \rangle = \ln A_{Fe} \cdot (X_{\max}^{\text{meas}} - X_{\max}^p) / (X_{\max}^{Fe} - X_{\max}^p)$. Figure 1.9(a) and 1.9(b) show values of $\langle \ln A \rangle$ using both methods. Values corresponding to the X_{\max} method show that below $\sim 4 \cdot 10^{15}$ eV the individual experiments seem to indicate a decrease of $\langle \ln A \rangle$ with energy, while above this energy up to $\sim 4 \cdot 10^{16}$ eV it is exhibited an increase with energy. At the highest energies $E \geq 4 \cdot 10^{16}$ eV, again a decrease with energy is observed. Results from the particle ratio method, using measurements at ground level, show a clear increase of $\langle \ln A \rangle$ with energy between 10^{15} and 10^{16} eV. The decrease

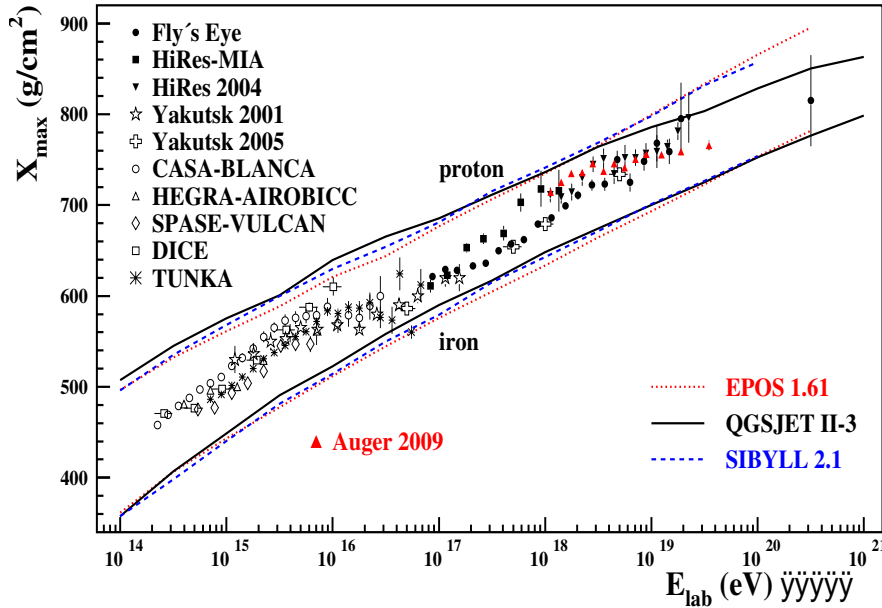


Figure 1.8: Average depth of the shower maximum X_{\max} as function of primary energy as obtained by different experiments and compared with simulations for proton and iron induced showers using the CORSIKA code with different hadronic interaction models [77].

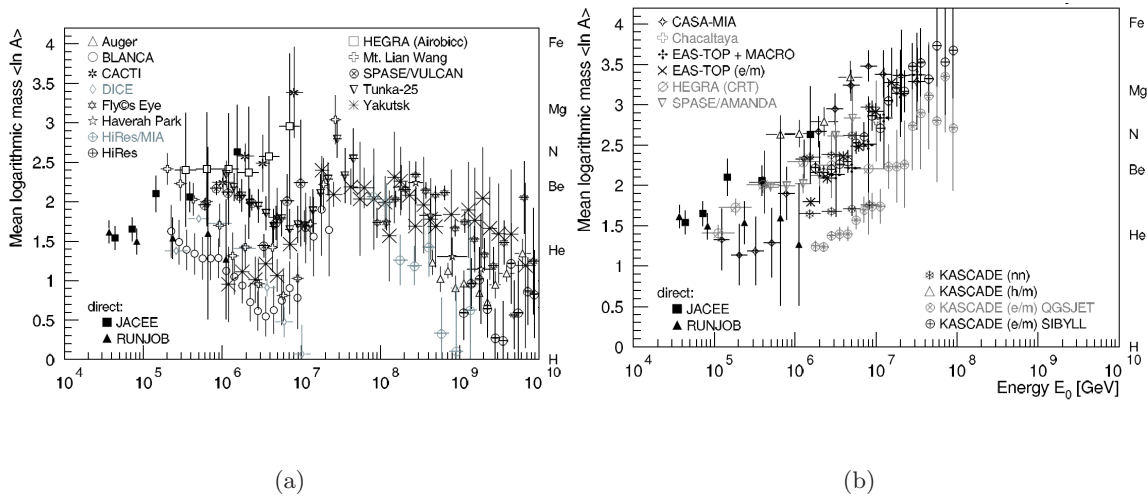


Figure 1.9: Mean logarithmic mass of cosmic rays derived from: (a) the average depth of the shower maximum, and (b) measurements of electrons, muons and hadrons at ground level (for references see [78]).

as derived from X_{\max} measurements is not visible in the particle ratio results. There seems to be some discrepancy between the results obtained from different methods [78]. It is also interesting to investigate the energy spectra for individual elements or **groups of elements**. Figures 1.10(a) and 1.10(b) show results on this issue obtained with the KASCADE hadron calorimeter. Information on the flux of primary protons can be inferred from the measurement

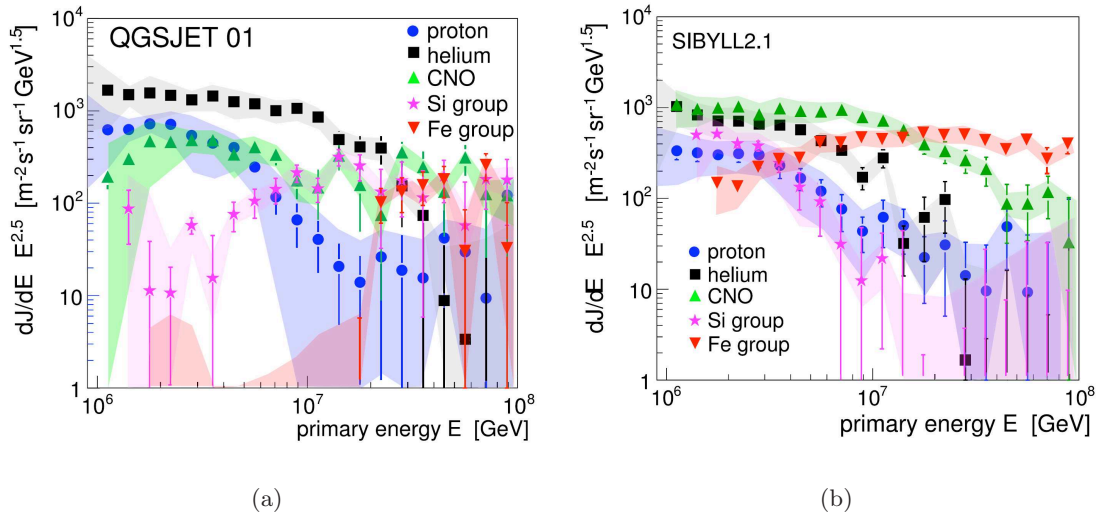


Figure 1.10: Cosmic-ray energy spectrum for five groups of elements as reconstructed by the KASCADE experiment using the hadronic interaction models: (a) QGSJET 01, and (b) SIBYLL 2.1 to interpret the measured data [28].

of the flux of unaccompanied hadrons at ground level. Unfolding algorithms were applied to the correlated frequency distribution of N_e and N_μ to derive energy spectra for elemental groups. The five mass groups chosen as representative are H, He, C, Si and Fe. The unfolding was performed using two interaction models, namely QGSJET and SIBYLL. The resulting all-particle spectra for both models show a knee at about 4 PeV and coincide within their statistical errors. The decrease of light elements across the knee is revealed independently of the used simulation code. In contrast, the spectra of silicon and iron groups differ significantly and look quite unexpected. This leads to conclude that both interaction models fail to reproduce the overall correlation between $\log_{10} N_e$ and $\log_{10} N_\mu$ as observed in the data. The spectra indicate that the knee in the all-particle spectrum is due to fall-offs in the light element spectra resulting in a heavier composition above the knee.

The EAS-TOP collaboration has measured the proton spectrum in the range 0.5-500 TeV, being described over the whole energy range by a single power law [79]. The underground MACRO experiment has studied the helium and CNO fluxes in the energy region from 80 to 200 TeV. After the subtraction of the measured proton flux, the following values were obtained: $\Phi_{He}(80 \text{ TeV}) = (12.7 \pm 4.4) \cdot 10^{-7} \text{ m}^{-2} \text{ sr}^{-1} \text{ GeV}^{-1}$ and $\Phi_{CNO}(250 \text{ TeV}) = (0.24 \pm 0.19) \cdot 10^{-7} \text{ m}^{-2} \text{ sr}^{-1} \text{ GeV}^{-1}$ [80]. In the knee region, intrinsic fluctuations and measurement accuracies allow a three component analysis: light (protons, and a mixture of 50% proton and 50% helium), intermediate (CNO) and heavy (Fe) [81]. Other experiments as the Tibet air shower array [82, 83] and the GRAPES-3 experiment [84] have obtained information on groups of elements as well.

For the highest energies there are some discrepancies depending on the methods used for indirectly deducing the mass composition. Analyzing $\langle X_{\max} \rangle$, a change from an iron dominated composition at 10^{17} eV to a proton dominated composition at $10^{19.3} \text{ eV}$ was found by the Fly's Eye experiment [34]. Using another interaction model, the conclusion holds, but at 10^{17} eV a mixed composition is expected. In contrast to the old measurements of Fly's Eye and Yakutsk [85], the HiRes data indicate a change from an iron-like to a proton

dominated composition already at 10^{18} eV. Also, the muon density measured in the HiRes-MIA setup indicates a change from heavy to light composition [86]. The observed muon densities, however, are higher or similar than the expectation for iron primaries and not compatible with medium or light nuclei [29,87]. The new Auger data are, within the systematic uncertainties, in good agreement with the published HiRes data (see Chapter 3). A re-analysis of Haverah Park data [88] threw a good description if a two-component composition with about $(66 \pm 2)\%$ iron in the energy range from $2 \cdot 10^{17}$ to 10^{18} eV is used. At higher energy (from 10^{18} to $2 \cdot 10^{18}$ eV), indications are seen for a transition to a lighter composition. On the other hand, a first study of the time structure of Haverah Park showers with zenith angles less than 45° finds a more iron-dominated composition in the same energy range [89]. Also a re-analysis of Volcano Ranch data favors a large fraction of iron [90]. The discrepancy between muon density-based composition measurements and others based on features of the longitudinal profile gives evidence of the problems still presented in the hadronic interaction models currently available.

Since showers produced by high energetic photons are almost pure electromagnetic cascades, the predictions related to them are more reliable. Analysis of Haverah Park data [91, 92] suggest that less than 48% of the observed events above 10^{19} eV can be photons (95% c.l.). At energies above $4 \cdot 10^{19}$ eV the limit is 50%. Based on the analysis of muons observed in high-energy showers at AGASA, the following upper limits were derived: 34%, 59% and 63% for primary energies above 10^{19} , $10^{19.25}$ and $10^{19.5}$ eV, respectively (95% c.l.) [93, 94]. Using a new method that accounts for the arrival direction of each individual shower, a limit of 67% (95% c.l.) could be derived for $E > 1.25 \cdot 10^{20}$ eV. This new method was also employed in a recent study of Auger shower longitudinal profile data [95]. No more than 16% photons are expected (95% c.l.). Analysis taking into account observables sensitive to the longitudinal shower development, the signal rise time and the curvature of the shower front, based on measurements with the Auger surface detectors show that the photon fraction is smaller than 2%, 5.1% and 31% above energies of 10^{19} , $2 \cdot 10^{19}$ and $4 \cdot 10^{19}$ eV respectively (95% c.l.). It should be noted that these upper limits are already relatively close to the fluxes expected for photons originating from the GZK effect [66]. Other analysis on showers above 10^{20} eV from AGASA and Yakutsk show a photon fraction of less than 36% (95% c.l.) [96].

According to *top-down* models for ultra-high-energy cosmic rays, a large flux of ultra high energy neutrinos is expected. Recent results from the Pierre Auger Observatory show that assuming an E_ν^{-2} differential energy spectrum, a limit of $E_\nu^{-2} dN_{\nu_\tau}/dE_\nu < 1.3 \cdot 10^{-7}$ GeV $\text{cm}^{-2} \text{s}^{-1} \text{sr}^{-1}$, in the energy range between $2 \cdot 10^{17}$ and $2 \cdot 10^{19}$ (90% c.l.), is derived [67].

Chapter 2

The Pierre Auger Observatory

The Pierre Auger Observatory has been conceived to collect unprecedented information about the flux, arrival direction, distribution and mass composition of cosmic rays from 10^{18} eV to the very highest energies with high statistical significance over the whole sky [20]. Its design was developed between 1992 and 1995 from a proposal by Jim Cronin (Chicago University), Alan Watson (Leeds University) and Murat Moratav (Paris VI and VII). The current amount of collaborators in the experiment is around 480 from 18 countries and 105 institutions. It was motivated by the great controversy generated from data corresponding to the region of energies around $\sim 5 \cdot 10^{19}$ eV, of the Cosmic-Ray spectrum, obtained by the AGASA **surface** array and the HiRes **fluorescence** detector, about the existence, or not, of the predicted GZK cut-off [42, 97, 98]. Therefore to obtain an accurate measurement of the spectral shape at those energies and beyond, using both kind of techniques, became crucial. The full sky coverage is also motivated by studies on anisotropy, point source determination and correlations with astrophysical objects. Due to the small rate of events above 10^{20} eV ($1 \text{ km}^{-2} \text{ sr}^{-1} \text{ century}^{-1}$), vast areas must be monitored to collect a large statistical sample, covering the full sky. Therefore two sites of the Observatory are planned, one in each of the Northern and Southern Hemispheres. The Northern site is in its planning stage, in Colorado at a latitude of 38° north. The Southern site was completed in June 2008 near Malargüe, in Mendoza Province, Argentina, at a latitude of more than 35° south. The Auger South Observatory consists of a surface detector (SD) array of 1600 water Cherenkov stations covering an area of 3000 km^2 and arranged on a triangular grid, with the sides of the triangles being 1.5 km. Four fluorescence detector stations (FD), each containing six air-fluorescence light telescopes, are located on the edges of the SD (see Fig. 2.1). The surface detector stations measure the density distribution of the EAS at ground while the telescopes measure the light produced by atmospheric nitrogen excited by the particles of the shower. Both kind of detectors are complementary and conform a *hybrid detector*. This allows to check data consistency from two independent measurements as well as inter-calibration and evaluation of systematic effects. Besides SD and FD, instrumental enhancements are currently being installed to measure showers in lower energy ranges and to focus to other kind of signals. This includes underground muon detectors and additional water Cherenkov stations with spacing of 750 m on an *infill* array (AMIGA), high-elevation fluorescence telescopes for a larger field-of-view (HEAT) and radio antenna to detect the geo-synchrotron emission of air showers (AERA) [99]. In addition to the detectors in the regular SD array, some locations were

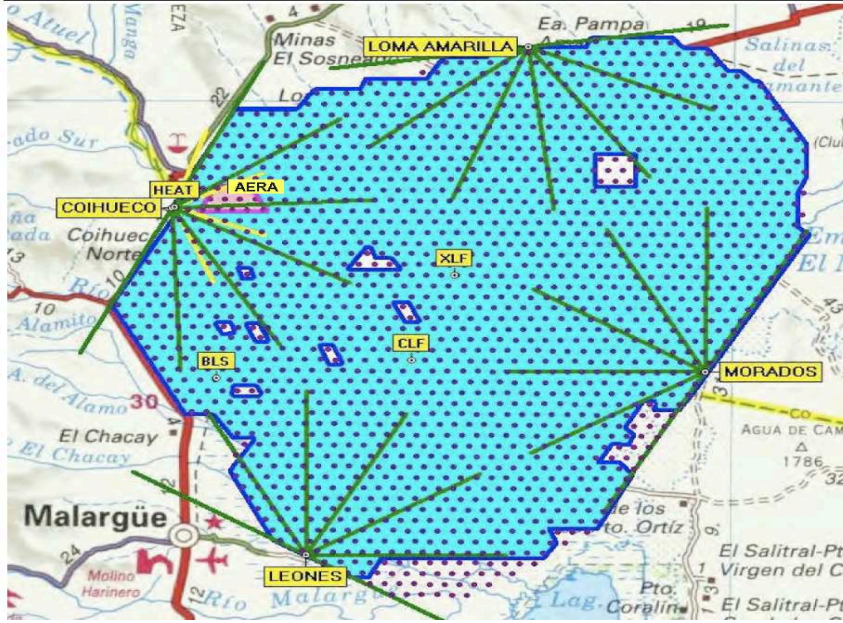


Figure 2.1: Actual status of the Pierre Auger Observatory, the shaded area are stations in operation and the “semi-asterisks” are the field of view of the fluorescence telescopes. All instrumental enhancements are close to the Coihueco FD station.

equipped with two (*twins*) and three (*triplets*) nearby detectors, placed at ~ 11 m from each other. They provide a very useful testbench for studies of signal fluctuation, timing resolution and energy and angular reconstruction precision. Specially these stations are important for estimating the uncertainty of arrival time parameters which is one of the goals of this work (see Chapter 4). In this chapter it is going to be described the operation of the detectors to be able to reconstruct EAS in a proper way and to obtain their mean characteristics.

2.1 Surface Detector

Each water Cherenkov station consists of a 3.6 m diameter water tank containing a Tyvek liner for uniform reflection of the Cherenkov light. The liner contains 12,000 l of ultra-high purity water with resistivity typically higher than $5 \text{ M}\Omega\text{cm}$. Three large 9” XP1805 Photonic photomultiplier tubes (PMTs) are symmetrically distributed at a distance of 1.20 m from the center of the tank and look downwards through windows of clear polyethylene into the water to collect the Cherenkov light produced by the passage of relativistic charged particles through the water. The water height of 1.2 m makes it also sensitive to high energy photons, which convert to electron-positron pairs in the water volume. A solar power system combined with batteries provides an average of 10 W for the PMTs and the electronics package consisting of a processor, GPS (Global Positioning System) receiver, radio transceiver and power controller. The PMTs are equipped with a resistive divider base having two outputs: anode and an amplified last dynode. This allows a large dynamic range, totaling 15 bits, extending from a few to about 10^5 photoelectrons. The high voltage (HV) is provided locally. The nominal operating gain of the PMTs is $2 \cdot 10^5$ and can be extended to 10^6 . The base, together with the

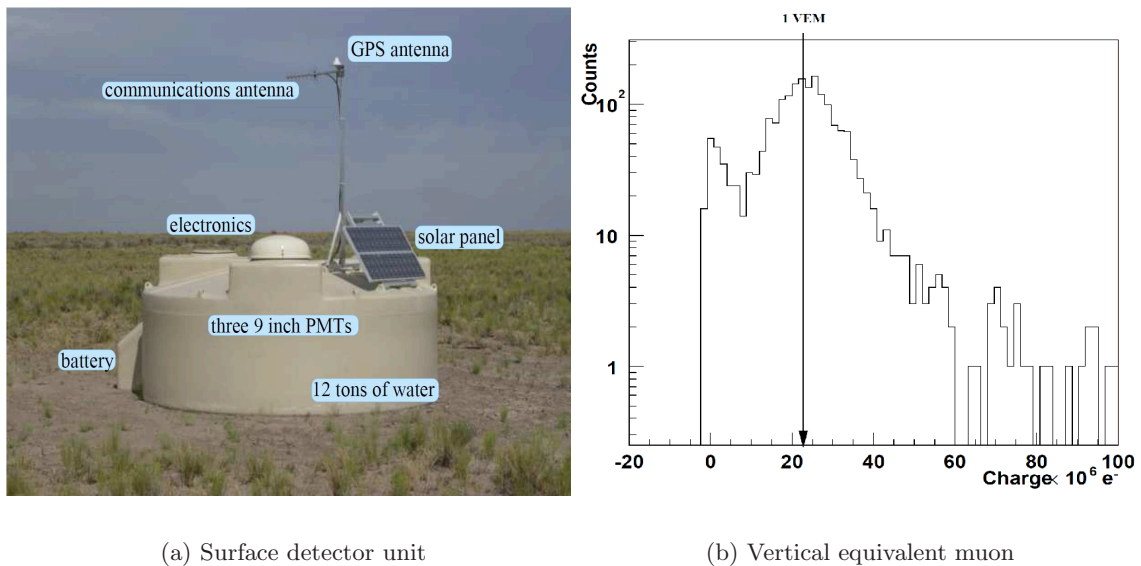


Figure 2.2: (a) A surface detector station showing its main components. (b) Vertical muon data taken on a test tank on the Southern Auger site. The small rise of the count rate for low charges (less than $10^7 e^-$) is due to a remaining part of the background. One VEM in this setup corresponds to $\approx 2.3 \times 10^7 e^-$, the production of about 25 photoelectrons in the PMT [100].

HV module, is protected against humidity by silicone potting. The signals from anode and dynode are filtered and digitized at 40 MHz using six 10 bit Flash Analog Digital Converters (FADC). A pedestal of 50 channels is added to the signal to observe possible fluctuations of the baseline. The signal recorded by the FADC is referred to in units of channels and is read by a programmable logic device (PLD) which performs trigger decisions on the signal. A common time base is established for different detector stations by using the GPS. Each tank is equipped with a commercial GPS receiver (Motorola OnCore UT) providing one pulse per second output and software corrections. This signal is used to synchronize a 100 MHz clock which serves to time-tag the trigger. Each detector station has an IBM 403 PowerPC micro-controller for local data acquisition, software trigger and detector monitoring, and memory for data storage. The station electronics is implemented in a single module called the Unified Board, and mounted in an aluminum enclosure on top of the hatch cover of one of the PMTs (see Fig. 2.2(a)). All communications are done via WLAN. A set of communication towers provides the link to the Central Data Acquisition System (CDAS). It is constructed using a combination of commercial hardware and custom-made, high level software components. Its primary role is to combine local trigger information from the SD stations and FD eyes to form the so called "central trigger", to request from all detector components the data relevant to this trigger, and finally to combine and store these data in a timely manner forming a "shower event". For the SD, the system also includes configuration and control mechanisms, means to monitor its performance and tools to access/download the monitoring, control, and configuration data. Except for the triggering information, the CDAS and the FD data acquisition systems are completely independent.

Water Cherenkov station calibration The aims of the calibration of each SD station are: to balance the individual PMTs such that they produce (on the average) the same

output signal in the high gain channel, to obtain the calibration constants needed to convert the registered FADC signal into an equivalent signal produced by vertical muons, to measure the amplification factor of the anode with respect to the last dynode and to set the trigger levels.

The reference for the absolute calibration of a detector station is the average signal produced by vertical muons from the cosmic ray background crossing the tank. The majority of the muons cross the tank and stay relativistic all the way, emitting a constant amount of Cherenkov light throughout the tank. A fraction of the muons, those with momenta below 300 MeV/c, can stop and decay inside the tank. The resulting charge distribution shows a peak, which corresponds to 1 vertical equivalent muon (VEM), the signal unit in the water tank [100](see Fig. 2.2(b)), which corresponds to an energy deposit of 240 MeV. The sum of the PMTs is a measure of the total signal deposited in the tank, whereas the individual PMTs are sensitive only to a fraction of the signal, deposited in the proximity. Thus this peak is at ≈ 1.09 VEM for the first case and 1.03 ± 0.02 VEM for individual PMTs [101]. The values were measured in a special setup consisting of a station equipped with two centered scintillators, one on top and the other underneath the station, the trigger requiring coincidences within the two scintillators [102]. By adjusting the trigger rates, the gains of the three PMTs are matched within 6%. The measurement of the muon charge spectrum from a reference tank allows us to deduce the charge value for the signal produced by a single, passing vertically through the center of the tank muon, Q_{VEM} , from which the calibration is inferred for the whole dynamic range. The average number of photoelectrons per muon collected by one PMT is 95, which means a charge of about 48 FADC channels. The FADC signal have a range of 0-1023 channels, corresponding to an input range of 0-2V. Each FADC bin corresponds to 25 ns. The cross calibration between the anode and dynode output channels is performed by using small shower signals in the overlap region [101]. The decay constant of the muon signal is related to the absorption length of the light produced. This depends on various parameters such as the Tyvek reflectivity and the purity of the water. The signal decay constant correlates with the so called area-to-peak (A/P) ratio of the signal: $A/P = Q_{VEM}/I_{VEM}$, where I_{VEM} is the maximum current of the muon signal. This A/P ratio is a routine monitoring quantity that is directly available from the local station software.

SD triggering system The surface detector triggering system includes the low level trigger received from the single station (T1,T2), the array trigger (T3) and the physical events trigger (T4 and T5). The T2 and T3 allow to detect the cosmic rays in a wide range of energies with an efficiency $> 95\%$ for cosmic rays with energies above 10^{18} eV [103].

Station triggers The local station trigger (T1) is evaluated by the PLD units and identifies the signals in a tank that could be part of a real air shower. It requires that the stations have to detect a coincidence between the 3 PMTs crossing the threshold value of 1.75 VEM above the baseline or a coincidence condition in at least 2 PMTs of more than 12 FADC bins with a signal of more than 0.2 VEM above the baseline in a window of 120 time bins. The calibration procedure already described ensures a T1 rate of about 100 Hz. The second station trigger (T2) is processed by the local software and requires either a *threshold trigger* (Thr2) or a *time over threshold trigger* (ToT). The Thr2 trigger consists of a coincidence of 3 PMTs above 3.2 VEM (fast large signals produced by the particles from either high energetic

EAS very close to the tank or by the muonic component in horizontal showers) and presents a rate of ≈ 20 Hz. The ToT trigger consist of a coincidence of 2 PMTs with traces having at least 13 bins above 0.2 VEM within a sliding window of $3\mu s$ width, which corresponds to 120 bins and presents a rate of 1 Hz (small signals given by particles far from the EAS core or low energy showers). When a tank trace satisfies both Thr2 and ToT only the latter is marked. If a tank satisfies the T2 threshold condition then it automatically satisfies the T1 condition. The Thr1 is usually observed for stations that are not part of an event, these stations are triggered by accidental muons, having a total signal of around 1-2 VEM.

CDAS trigger The lowest CDAS trigger (T3) identifies time coincidences between the signals in different tanks that could be associated with a real air shower. However, it does not guarantee that the data are physical events because a large number of chance coincidences in accidental tanks is expected due to low energetic showers and to single cosmic muons. Therefore any of the following requests must be also satisfied:

- (a) A 3-fold condition, which requires a coincidence within a time interval depending on the distance of three tanks passing the Time Over Threshold trigger (ToT) condition.
- (b) A 4-fold coincidence which requires the coincidence within a time window depending on the tank distance among 4 tanks having passed any T2 condition, with 2 tanks inside 2 hexagonal crowns around a central triggered tank and a further one within 4 crowns. A crown is formed by the stations at equal distance from the central one and are numbered depending on this separation [104] (see Fig. 2.3(a)).
- (c) A 3-fold condition which requires the coincidence of three aligned tanks passing any T2 conditions.
- (d) An external condition generated by the Fluorescence Detector (FD).

The trigger time of each station having passed a T2 condition is sent to the CDAS and stored. All stations within a sliding time window of $50\mu s$ are searched for the above patterns. If a pattern is found, the search stops and an event with the T3 trigger is formed. Information of stations from the whole array with trigger times in coincidence with the central station is also stored in the event file. Trigger times are considered to be in coincidence if they are within a time window of $(6 + 5n)\mu s$ from the central triggered station where n indicates the crown number. Some other information as the station position, identification (id), calibration histograms and an error code, are also stored in the data file. A large set of events is recorded even if they are not physical for a subsequent analysis.

Physical trigger The physical trigger (T4) was designed to distinguish air showers from random coincidences of single atmospheric muons and is the first step to select the vertical events which can be reconstructed. The requirements are:

- (a) At least 3ToT stations forming a triangle of first neighbours (Fig. 2.4(a)). This trigger is not effective for events with large zenithal angles due to the dominance of the muonic component in this case, which gives origin to fast and narrow signals, but selects 99% of the events with zenithal angle less than 60° [103,105].

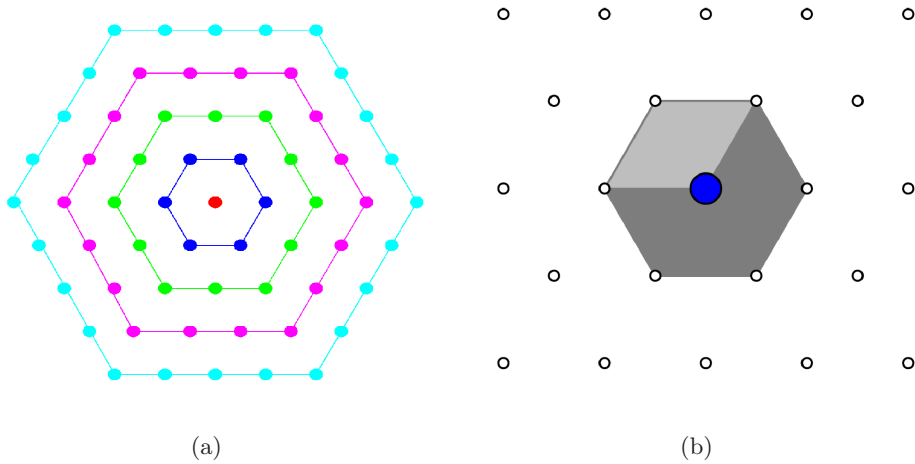


Figure 2.3: (a) The hexagon array around the central station taken into account for the T3 trigger. (b) The T5 Configuration.

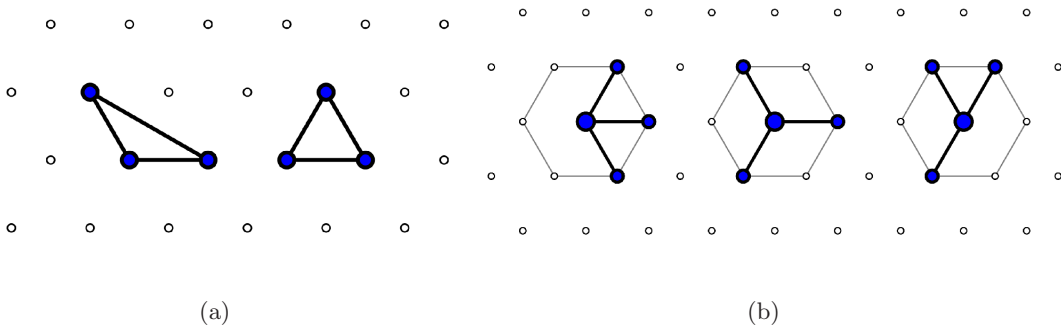


Figure 2.4: (a) Two possible 3TOT compact configurations. (b) The three minimal 4C1 configurations.

(b) 4T2 triggered stations being in a configuration of one station with 3 neighbours in the first crown as shown in Fig. 2.4(b). This is called 4C1 trigger condition.

The T4 trigger also requires compatibility in time between stations which are part of the event. The difference in their start time has to be lower than the distance between them divided by the speed of light, allowing for a marginal limit of 200 ns.

Quality trigger The quality trigger (T5), also called fiducial trigger, has been implemented to exclude events that fall too close to the edge of the SD array, for which the reconstruction of the air shower variables may not be reliable. The requirement of this trigger is the existence of six nearest and functioning (but not necessarily triggered) neighbours, for the station with the largest signal, at the time of the shower impact (see Fig. 2.3(b)) [106]. This trigger becomes fundamental for ensuring an easy way to calculate the acceptance of the detector since it would be hard to obtain taking into account events that are highly energetic but far away from the array.

The *full efficiency* of the SD trigger is reached at $3 \cdot 10^{18}$ eV for zenithal angles less than 60° . Above this energy, the calculation of the exposure is based on the determination of the

geometrical aperture and of the observation time. The aperture of the array is obtained as a multiple of the aperture of the elemental hexagon cell. The number of cells is not constant over time and is constantly monitored. The evolution of the number of trigger cells is globally similar to the evolution of the *acceptance*. The expected fractional signal loss in 10 years, due to changes in the liner reflectivity, the water quality, seasonal effects and day-night variations, is less than 10% which gives confidence in a very good long-term performance of the SD.

Reconstruction of air showers using the Surface Detector

The geometry of the air shower, the estimator of the energy $S(1000\text{m})$ and the mass sensitive parameters are obtained from the reconstruction of measured signals [107]. This is performed after the selection of the stations which belong to the event, then, the impact point on the ground and the arrival direction of the air shower are estimated. At this state, the shape parameters of the lateral distribution function (LDF), which are dependent on the zenithal angle, are initialized. Parameter $S(1000\text{m})$ is also initialized as the signal in the station closest to a distance of 1000 m to the shower center. In the next step the $S(1000\text{m})$ and core location fitting is performed with a maximum likelihood method and depending on the number of candidate stations, the LDF parameters are gradually included as variable parameters. Fixing the core position, the curvature is reconstructed and all the previous steps are repeated iteratively because the axis of the shower might change in this last step and therefore the whole configuration of the shower [108]. The energy of the event is determined calibrating the $S(1000\text{m})$ parameter with the energy measured with the FD.

Station selection The selection of stations which belong to the event is based on algorithms applied at the level of PMTs and stations. Bad calibrations and/or accidental timing information can be reasons to reject the station from the reconstruction [108, 109]. On principle, stations with an external trigger such as FD, stations with lightning like signals, second doublets of the twins (the one with the higher id), the *infill* stations and stations with bad altitude are removed. The accidental triggered stations (given by the atmospheric muons) are defined according to their distance to the first neighbours, and to their compatibility in timing information with a planar front derived from a so-called *seed*. A seed is defined as the three stations which maximize the size of the signal. Using the Bottom Up algorithm [110], the time delay of a station to the propagating planar front is computed. If it is between -1000 ns and 2000 ns, the station is kept. Between -2000 ns and 4000 ns, it is flagged as ambiguous and outside this window, it is marked as accidental. Accidental stations are considered *isolated* if they have no neighbour in 1800 m or only one in 5000 m, then they are rejected.

Geometry reconstruction The simplest model of the shower front is approximated by a plane, which is a robust estimator of the shower axis direction [107].

A shower track (see Fig. 2.5(a)) can be visualized as a point $\hat{x}(t)$ moving with the speed of light c along the straight line with (normalized) axis \vec{a} , which points towards the source, and passing the origin at time t_0 ,

$$c(t_0 - t) = (\hat{x}(t) - \hat{b})\vec{a}. \quad (2.1)$$

The *origin* \hat{b} from where all the distances are measured is set as the signal-weighted barycentre of all the stations involved in the fit. The weighted bary-time is set as the time origin, t_0 .

Chapter 2. The Pierre Auger Observatory

The initial *impact point* on the ground is equal to \hat{b} and is replaced subsequently by a more accurate estimation for the lateral distribution function fit.

The *shower plane* is a plane perpendicular to the shower axis, moving along with the same speed and containing the shower forehead. To infer on the time $t(\hat{x})$ when the shower plane is passing through some chosen point \hat{x} on the ground, the point has to be projected to the shower axis,

$$ct(\hat{x}) = ct_0 - (\hat{x} - \hat{b})\vec{a}. \quad (2.2)$$

Assuming that the positions of the stations are given with absolute precision and the only deviations can be due to the time uncertainty σ_t of the signal start, the function to minimize is the squares of the time differences between the measured signal start and the model time prediction (Eq. (2.2)). Denoting the components of the shower axis $\vec{a} = (u, v, w)$, the station coordinates $\vec{x}_i = (x_i, y_i, z_i)$, and σ_i the uncertainty of the time multiplied with the speed of light

$$\chi^2 = \sum_i \frac{[ct_i - ct_0 + x_i u + y_i v + z_i w]^2}{\sigma_i^2} \quad (2.3)$$

with a constraint of $u^2 + v^2 + w^2 = 1$ inherited. Due to this constraint, the problem is not linear, but an approximate solution can be obtained in the ansatz that all stations lay close to a plane, $z_i \ll x_i, y_i$ and therefore the z -component can be neglected.

The minimization can fail only in one case, when there is a linear dependence of the station positions (as when having three stations in a line). For higher station multiplicity the occurrence of such a situation is highly unlikely.

The more realistic shower front model is based on a curved front fit, as illustrated in Fig. 2.5(b). It is done by extending the plane fit method with a parabolic term that describes the curvature of the shower front near the impact point \hat{c} , i.e. $\rho \ll R_c$. Using $\vec{x} = \hat{x} - \hat{c}$, Eq. (2.2) can be extended to get

$$ct(\hat{x}) = ct_0 - \vec{a}\vec{x} + \frac{\rho(\vec{x})^2}{2R_c}, \quad (2.4)$$

with perpendicular distance $\rho(\vec{x})^2 = (\vec{a} \times \vec{x})^2 = x^2 - (\vec{a}\vec{x})^2$. The first approximation to the radius of curvature is obtained from a slightly different model in which the time propagation of the shower front is described as an expanding sphere. The timing information can be decoupled from any information on the impact point. The fit parameters are the radius of curvature, R_c and the shower axis. The shower axis is a derived quantity, obtained only after the position of the impact point is known. Therefore the curvature fit is done only after the lateral distribution function fit, after the core is known. The solid angle differences between the plane-fit and curvature-fit axis \vec{a} are of the order of a half degree.

An exact three-dimensional minimization of a function

$$\chi^2 = \sum_i \frac{[c(t_i - t_0) - |R_c \vec{a} - \vec{x}_i|]^2}{c^2 \sigma_{t_i}^2} \quad (2.5)$$

is also attempted with accurate $z_i \neq 0$ treatment. The differences between the approximate estimation of R_c and this one are of the order of few 10 m, while the solid angle difference between the axes is of the order of a few 0.1° .

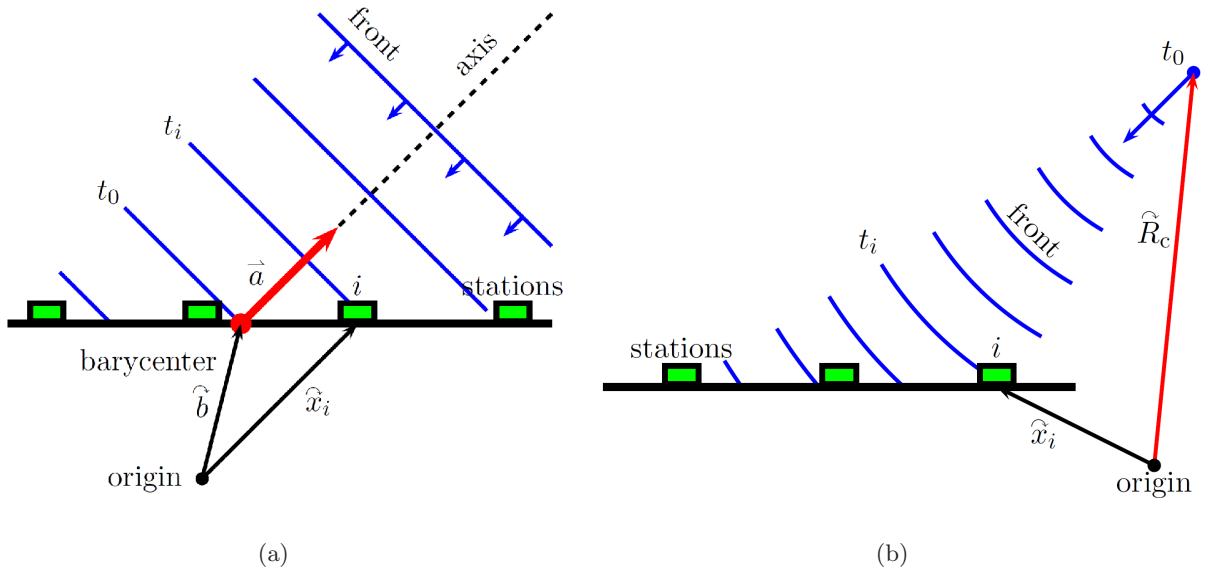


Figure 2.5: (a) Schematic of the plane front arrival. (b) Schematic of the spherical shower front development. Taken from [108].

The intrinsic time variance is modelled estimating the number of particles (muons) n in the signal, from the VEM station signal S , corrected for the zenithal angle dependence of the average track length \bar{L} ,

$$n = \frac{S}{\ell(\theta)}, \quad \ell = \frac{\bar{L}(\theta)}{\bar{L}(0)}, \quad \bar{L}(\theta) = \frac{\pi}{\pi \cos \theta + 2(h/r) \sin \theta} \quad (2.6)$$

where h and r are tank height and radius, respectively [111, 112].

Lateral distribution function The surface detector samples only a part of the particles arriving at the ground, showing a specific stage of the lateral development of the shower, therefore a fit of the lateral distribution of the particles is necessary. The lateral dependence of the signal measured in tanks is modeled as

$$S(r) = S(1000 \text{ m}) f_{\text{LDF}}(r), \quad (2.7)$$

where $f_{\text{LDF}}(r)$ is a particular shape parameterisation normalized to $S(1000 \text{ m})$, the signal at 1000 m from the shower core. As shown in Fig. 2.6(a), in the case of 1.5 km spacing of individual tanks, the fluctuations of the particle density are minimized about 1000 m from the shower core [113–115], therefore it is called the optimal distance r_{opt} and depends mainly on the spacing of the array. The uncertainty of the signal [116–118] is taken as

$$\sigma_S(\theta) = (0.32 + 0.42 \sec \theta) \sqrt{S}. \quad (2.8)$$

The shower impact point must be accurately defined since it is directly related to $S(1000 \text{ m})$ and also to the definition of the χ^2 function used for obtaining the best fit of the LDF [107]. It is defined to lie in the plane tangent to the Earth's reference ellipsoid containing the barycentre

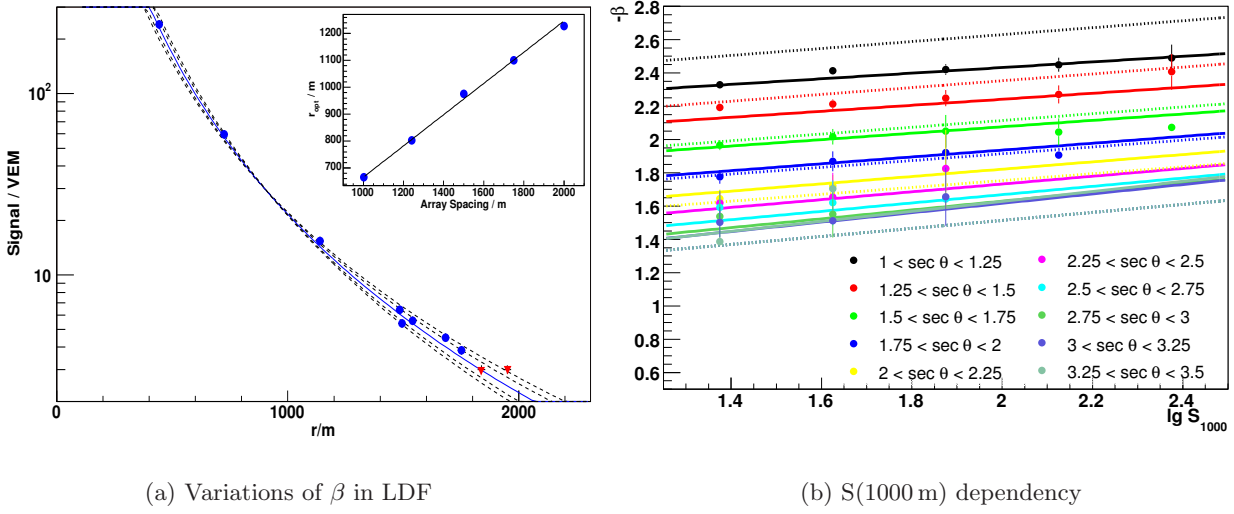


Figure 2.6: (a) Reconstructed LDFs using different values of β , variations lead to the same $S(r)$ at r_{opt} [123]. (b) Parameterisation of the LDF parameter β on $S(1000\text{ m})$ [120].

of the stations. The core location \hat{c} , obtained by the previous stages in the reconstruction chain is projected along the shower axis \vec{a} towards the plane defined by the barycentre $\hat{b} = (0, 0, 0)$ and a normal $\vec{n} = (0, 0, 1)$

$$\vec{c}' = \hat{c} + \frac{\vec{n}(\hat{b} - \hat{c})}{\vec{n} \cdot \vec{a}} \vec{a}. \quad (2.9)$$

Several functional forms of the LDF have been investigated in [119, 120]. It turned out that the best description is given by a power-law-like function and a modified Nishimura Kamata Greisen (NKG) function [121, 122]. The function used by the Pierre Auger Observatory is a slightly modified NKG function

$$f_{\text{LDF}}(r) = \left(\frac{r}{1000\text{ m}}\right)^\beta \left(\frac{r + 700\text{ m}}{1700\text{ m}}\right)^\beta, \quad (2.10)$$

with the slope β fixed according to the following parameterisation

$$\beta(\theta) = \begin{cases} a + b(\sec \theta - 1), & \sec \theta < 1.55 \quad (\theta \geq 50^\circ), \\ a + b(\sec \theta - 1) + f(\sec \theta - 1.55)^2, & \sec \theta \geq 1.55. \end{cases} \quad (2.11)$$

with

$$\begin{aligned} a &= 2.26 + 0.195 \lg e, & b &= -0.98, \\ c &= 0.37 - 0.51 \sec \theta + 0.30 \sec^2 \theta, & e &= c(S_{1000})^d \text{ (energy estimate)}, \\ d &= 1.27 - 0.27 \sec \theta + 0.08 \sec^2 \theta, & f &= -0.29. \end{aligned} \quad (2.12)$$

The parameterisation evolved meanwhile adding a quadratic term in Eq. (2.11). The increase of event statistics made a more accurate parameterisation possible [120]. A comparison to the default values is shown in Fig. 2.6(b).

If β is estimated to be larger than -1 , it is fixed to this value. The LDF is divergent at $r = 0$, because of negative value of β . The reconstruction of the LDF is done only with three free parameters: $S(1000\text{ m})$ and the core location (two components, x and y). The uncertainties on $S(1000\text{ m})$ from fixing β are obtained doing two additional reconstructions with $\beta \pm 3\%$.

A *Maximum likelihood method* applied to calculate the LDF parameters allows to include zero-signal stations, small signals (i.e. small particle densities) and large signals into the fit as well as to handle the signal of saturated stations. The first step is to define an effective particle number. The water-Cherenkov tanks provide information about Cherenkov photons, which are released by muons, electrons, or converted photons when passing the tanks. The total signal measured in a tank has two major contributions: electromagnetic part and the muonic part

$$S = S_\mu + S_{e/\gamma} \quad (2.13)$$

in the assumption that a single converted photon and a single electron, equally energetic, deposit the same mean signal in a tank. A muon is considered to deposit 1 VEM irrespective of incoming angle, distance, etc.

The signal $S_{e/\gamma}$ is much smaller on average than S_μ and the mean conversion factor for electrons and photons to signal is smaller than 1 VEM. The total number of particles that have produced the signal is then estimated as

$$n = p(r, \theta | E, A) S, \quad (2.14)$$

where $p(r, \theta | E, A)$, the so-called *Poisson factor*, is approximated to 1 for $\sigma_S(\theta) \geq 1$ and $1/\sqrt{\sigma_S(\theta)}$ otherwise. It is independent of primary energy and mass as well as core distance and zenithal angle [116]. The signals recorded in tanks close to the trigger threshold S_{thresh} , typically at larger distance from the shower core, have a large muon content, and therefore p is taken to be 1. Assuming that the transition to half-signal electron deposit content takes place when the signal exceeds the threshold S_{thresh}^G , the final simplified conversion between signal and particles is

$$n(r, \theta | E, A) = n = \begin{cases} S(r, \theta | E, A) & ; S < S_{\text{thresh}}^G \\ 2S(r, \theta | E, A) & ; S \geq S_{\text{thresh}}^G \end{cases}. \quad (2.15)$$

where $S_{\text{thresh}}^G = 15\text{ VEM}$ corresponding to an estimated number of particles of ≈ 30 .

The likelihood function, gathering the sampled information of tank i at distance r_i to be maximized is

$$L = \prod_i f_P(n_i, \mu_i) \prod_i f_G(n_i, \mu_i) \prod_i F_{\text{sat}}(n_i, \mu_i) \prod_i F_{\text{zero}}(n_i, \mu_i) \quad (2.16)$$

and thus the log likelihood function gives

$$\ell = \sum_i \ln f_P(n_i, \mu_i) + \sum_i \ln f_G(n_i, \mu_i) + \sum_i \ln F_{\text{sat}}(n_i, \mu_i) + \sum_i \ln F_{\text{zero}}(n_i, \mu_i), \quad (2.17)$$

with n_i the effective number of particles detected in the tank and μ_i the corresponding theoretical expectation. The different contributions are as following:

(a) Small signals, $n < 30$ particles, which have a Poisson distribution

$$\ln f_P(n_i, \mu_i) = n_i \ln \mu_i - \mu_i - \sum_{j=1}^{n_i} \ln j. \quad (2.18)$$

(b) Large signals, $n > 30$ particles, with Gaussian distribution

$$\ln f_G(n_i, \mu_i) = -\frac{(n_i - \mu_i)^2}{2\sigma_i^2} - \ln \sigma_i - \ln \sqrt{2\pi}. \quad (2.19)$$

(c) Stations without signal. The assumed threshold to trigger a tank is $n_{\text{thresh}} \geq 3$, i.e. at least 3 muons hitting the tank. Therefore their contribution is a sum over all Poissonian probabilities with a predicted particle number μ_i and actual particle number $n_i \leq n_{\text{thresh}}$

$$\ln F_{\text{zero}}(n_{\text{thresh}}, \mu_i) = -\mu_i + \ln \left(\sum_{n=0}^{n_{\text{thresh}}} \frac{\mu_i^n}{n!} \right). \quad (2.20)$$

There might be a slight complication due to different local trigger algorithms. In a first approximation the *threshold trigger* ($S_i \simeq 3$ VEM) fulfills the n_{thresh} condition, while a *time over threshold* (ToT) has certainly a lower threshold ($S_i \simeq 1.7$ VEM) but is unlikely to be the trigger at larger radii.

(d) Saturated signal, for which n_i represents a lower limit on the actual signal. Integrating f_G over all possible values larger than n_i , an estimate of the probability detecting a signal larger than n_i is obtained as

$$F_{\text{sat}}(n_i, \mu_i) = \int_{n_i}^{\infty} f_G(n, \mu_i) dn = \frac{1}{2} \text{Erfc} \left(\frac{n_i - \mu_i}{\sqrt{2}\sigma_i} \right), \quad (2.21)$$

where $\text{Erfc}() = 1 - \text{Erf}()$ is the complementary *error function*.

The missing signal can be recovered and included in the LDF fitting procedure as it is described in the next lines.

The signal reconstruction of one half of the showers with energies above 30 EeV is affected by the saturated readouts from the dynodes and anodes in tanks within 600 m from the core. There are two methods to recover the saturated signal, which are combined and employed for estimating the true signal [108,124]. The first method uses the undershoot of the anode signal, U_a , caused by the variation of the baseline after the signal due to the coupling capacitors attached to the anode circuits. U_a is linearly correlated with the total charge, Q_a . The second method considers a Moyal function, which precisely describes the signal distribution in time. A fitting of a Moyal function to the non-saturated parts of the signals is performed:

$$Q_a(t) = A \cdot e^{-1/2 \left(\frac{t-t_0}{\sigma} + e^{-\frac{t-t_0}{\sigma}} \right)}, \quad (2.22)$$

where t is the time after the start of the signal. The parameters t_0 and σ are the time of maximum and spread in the signal, respectively and they are parameterised in non-saturated traces in terms of reconstructed zenithal angle and core distance. Since in events with

saturated signals the reconstruction of r and θ will be less accurate, t_0 and σ are parameterised in terms of U_a . In this manner the two methods are combined and the dynamic range at which signal can be measured is extended from ~ 1000 VEM to 10^6 VEM. The uncertainties in the recovered signal, estimated using twin stations located at ~ 10 m from each other, rise from $\sim 10\%$ at 1000 VEM to $\sim 70\%$ at 10^6 VEM. The recovered signal, with its uncertainty is used in the lateral distribution fitting procedure. However, the LDF is not known in the region close to the core, in such cases the recovered signal should be used as a lower limit until better knowledge of the LDF is achieved. For this purpose an empirical cut on the second derivative of the LDF normalized to $S(1000\text{ m})$ has been implemented: if $LDF''(r_{sat})/S(1000\text{ m}) > 1$ the signal is treated as a lower limit, then the first estimation of the LDF and the saturated station distance is obtained using the standard procedure. The impact on $S(1000\text{ m})$ is on average smaller than 1% at low energies and about -3% at high values of $S(1000\text{ m})$. The *saturation recovery* method also has a positive impact improving the shower reconstruction of golden hybrid data.

Although the recovered signals are used as part of the event reconstruction, the time spreads of the recovered signals have not been studied and they are not used in risetime analysis in this thesis.

Determination of the energy The calibration of the energy scale for the SD array is determined using the correlation between the energy measured by FD and the parameter $S(1000\text{ m})$ for a subset of hybrid events [125]. It must be guaranteed (using the T5 trigger described before) for each event, that the intersection of the axis of the shower with the ground is within the array, and that the shower is sampled sufficiently to make reliable reconstruction of $S(1000\text{ m})$ and of the shower axis. From the analysis of hybrid events, using only the fall of the signal size with distance, these criteria result in a combined trigger and reconstruction efficiency greater than 99% for energies above $\sim 3 \cdot 10^{18}$ eV; at $\sim 2.5 \cdot 10^{18}$ eV it is 90%. The sensitive area has been calculated from the total area of the active hexagons. The decrease of $S(1000\text{ m})$ with zenithal angle arising from the attenuation of the shower and from geometrical effects is quantified by applying the Constant Intensity Cut (CIC) method [126]. The surface detector will measure different particle densities for the same energy of the primary particle, depending on zenithal angle. In order to correct for geometrical as well as for attenuation effects, the CIC method assumes that the flux, or the intensity (integrated flux above a certain energy) is isotropic for all energy ranges. The attenuation curve $CIC(\theta)$ is parameterised as

$$CIC(\theta) = 1 + a \cdot (\cos^2 \theta - \cos^2 38^\circ) + b \cdot (\cos^2 \theta - \cos^2 38^\circ)^2. \quad (2.23)$$

An energy estimator for each event, independent of θ , is S_{38° , the $S(1000\text{ m})$ that would be measured if the air shower comes from a zenithal angle of 38° . This angle is selected because it is the mean value for measurements, therefore the impact of the correction function is minimized. For a given shower, the corresponding S_{38° is obtained as

$$S_{38^\circ} = \frac{S(1000\text{ m})}{CIC(\theta)}. \quad (2.24)$$

Using information from the fluorescence detectors the energy corresponding to each S_{38° can be estimated almost entirely from data except for assumptions about the missing energy (the energy carried into the ground by muons and neutrinos). The geometry of each event

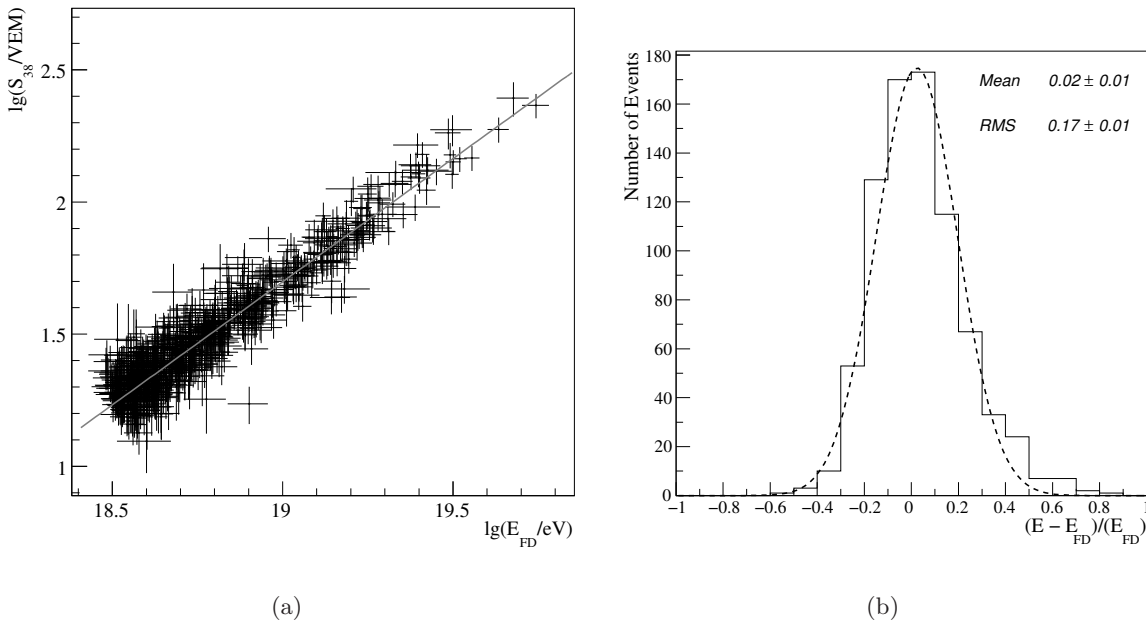


Figure 2.7: (a) Correlation between $\log E_{FD}$ and $\log S_{38^\circ}$. (b) Fractional difference between the calorimetric energy, E_{FD} , and the energy estimate of the surface detector E [127].

is determined from the times recorded by individual pixels at an FD, supplemented by the time information from triggered station with the highest signal. For the calibration it is also required for the FD measurements, that a reduced χ^2 is less than 2.5 for the fit of the longitudinal profile and that the depth of shower maximum is within the field of view of the telescopes. The fraction of the signal attributed to Cherenkov light must be less than 50%. Statistical uncertainties in S_{38° and the energy of FD (E_{FD}) are assigned to each event. The correlation of S_{38° with E_{FD} is shown in Fig. 2.7(a), together with the least-squares fit of the data to a power-law, $E_{FD} = A \cdot S_{38^\circ}^B$. The best fit yields $A = (1.51 \pm 0.06(stat) \pm 0.12(syst)) \times 10^{17}$ eV and $B = 1.07 \pm 0.01(stat) \pm 0.04(syst)$ [127]. The parameter S_{38° grows approximately linearly with energy, with $a = 0.90 \pm 0.05$ and $b = -1.26 \pm 0.21$ [127]. The energy resolution, estimated from the fractional difference between E_{FD} and the derived SD energy is shown in Fig. 2.7(b). Systematic uncertainties on the energy scale due to the calibration procedure are 7% at 10^{19} eV and 15% at 10^{20} eV, while a 22% systematic uncertainty in the absolute energy scale comes from the FD energy measurement.

2.2 Fluorescence Detector

Each of the four FD stations contain six individual air-fluorescence light telescopes (see Fig. 2.8(a) [128]) consisting of a spherical mirror of radius 3.4 m, the aperture opening (radius 1.1 m) with a ring-shaped corrector lens on its outer (25 cm) and a spherical pixel camera (radius 1.7 m). The camera is equipped with 440 hexagonal PMTs (or pixels, Photonis XP-3062), arranged in a 22×20 matrix. Programmable potentiometers equalize the gains of the PMTs to guarantee an uniform time response and amplitude. The the mirror and the camera are both placed at the center of the aperture, resulting in a fully concentric setup (see Fig. 2.8(b)). All detectors take data independently having a field-of-view (FOV) of about $30^\circ \times 30^\circ$ in azimuth and zenith. There are four layers of trigger algorithms to be passed

for an event to qualify for readout [129]. The first level trigger (FLT) works on the level of individual pixels and requires the sum over 10 consecutive time bins of the FADC trace to be above the FLT threshold. The threshold is dynamically adjusted to produce a 100 Hz FLT trigger rate per pixel. A fast hardware-implemented second level trigger (SLT) collects all FLT's from one camera and searches for geometric patterns (see Fig. 2.9). The third level trigger (TLT) is a software trigger which checks the time structure of an event on telescope level. After the TLT is measured all data from the telescopes of one eye are collected by the *eyePC*. On the *eyePC*, the combined mirror events have to pass the eye level trigger (T3), which performs a rudimentary event reconstruction to calculate the direction and time of impact on the ground. This information is sent to the CDAS in order to trigger data readout of the corresponding parts of the SD array.

Calibration Data from the telescopes are calibrated using the end-to-end calibration technique [130] in the sense that it accounts for all the components of the system from filters to mirrors to PMTs to the readout electronics. A uniform Lambertian light emitter (drum) is mounted directly in front of the aperture of a telescope and the response of each pixel is measured. The calibration constant is then calculated as the ratio of the known number of photons entering the diaphragm and the total signal recorded in the pixel. Any signal recorded during shower observation is multiplied with this calibration constant to yield the number of photons entering the diaphragm without needing to know the details of the telescope optics or electronics. There is also a relative calibration procedure [131] that is run nightly to monitor any changes in the system. The absolute calibration of the detector has currently an uncertainty of about 10 %.

Atmospheric monitoring The condition of the atmosphere plays an essential role since EAS are produced and propagated through it. Therefore its monitoring has to be done permanently. The total integrated amount of airmass, scattering and attenuation of ultraviolet photons, as well as the detailed density profile have a significant effect on the air shower measurement. The monitoring data are processed and stored in SQL databases to make them easily accessible during reconstruction and simulation tasks. Following atmosphere monitoring devices are used at the Pierre Auger Observatory.

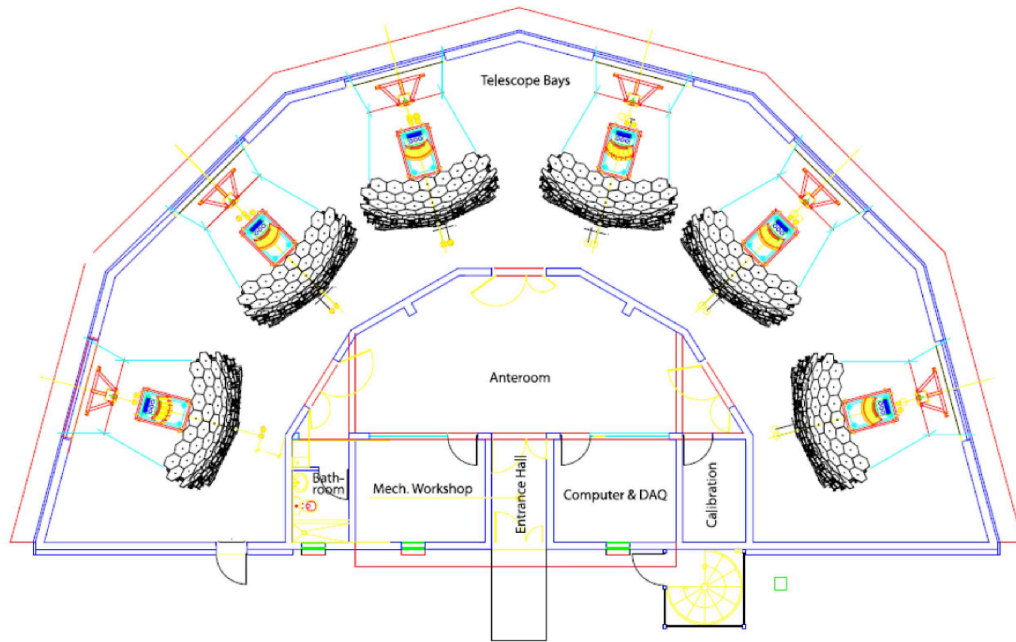
Radio sondes are used to measure vertical temperature and density profiles [132].

Cloud cameras perform a full sky infrared imaging to detect clouds and are installed on top of each telescope building.

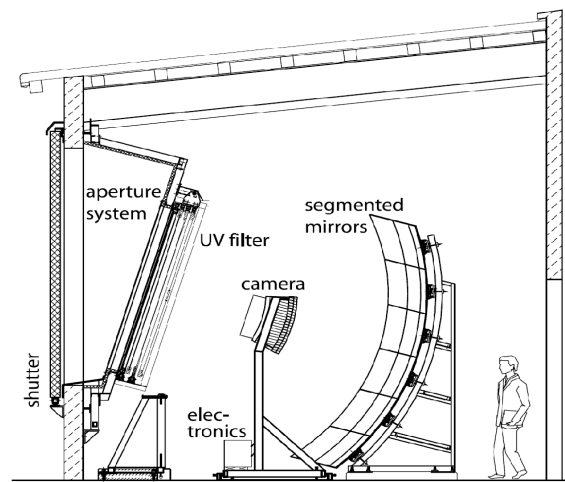
LIDAR (Light Detection And Ranging) are steerable UV lasers located at each FD eye, they scan the sky for clouds and measure aerosol backscattering [133].

CLF and XLF (Central Laser Facility and Extra Laser Facility) provide a test beam to cross-check geometric alignment, relative timing between SD and FD [134], and aerosol. The laser light is scattered by the air and detected by some telescopes.

HAMs (Horizontal Attenuation Monitors) measure the horizontal attenuation length at near ground level between the FDs. Each HAM system consists of a continuous light source, located at one FD, and a receiver located at another FD.



(a) Schematic layout of the building with six fluorescence telescopes



(b) Schematic view of a fluorescence telescope

Figure 2.8: Setup of the fluorescence detector.

APF (Aerosol Phase Function) are designed to measure the aerosol differential scattering cross-section. Lasers shoot horizontally in front of the FD detectors to observe scattered laser light over a large scattering angle range. This is used to measure the Mie scattering phase function [135] to study the contamination of the fluorescence signal by Cherenkov

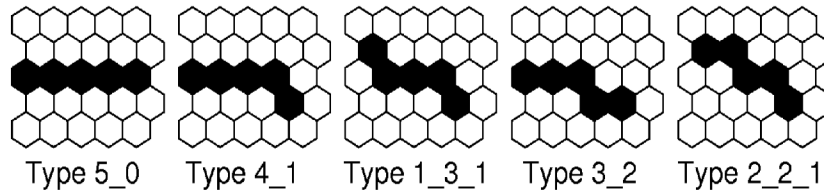


Figure 2.9: Fundamental types of pattern regarded as straight track segments.

photons.

FRAM (Fotometric Robotic Telescope for Atmospheric Monitoring) observes bright ultraviolet stars of known magnitude. Measurements of the aerosol attenuation, extinction coefficient and presence of clouds is obtained [136].

Reconstruction of air showers using the Fluorescence Detector

The reconstruction of air showers in the Pierre Auger Observatory is hybrid as mentioned before. With the FD it is possible to estimate the energy, needed for the energy calibration of the SD, and the geometry of the shower can be improved with the help of the timing from one SD station. Both procedures are part of the event reconstruction with the FD.

Pulse finder and geometry reconstruction The ADC-counts of the fluorescence detector are written by the data taking software for a period of 100 μs . The pulse related to the detection of fluorescence light from an air shower is obtained from the ADC trace by means of a signal over noise ratio (S/N). Starting from the first triggered time bin, the boundaries of the suspected pulse are shifted to find the maximal S/N-ratio

$$S/N = \frac{S(\Delta t)}{\sqrt{\Delta t} \times RMS}. \quad (2.25)$$

$S(\Delta t)$ is the total signal within the tested pulse length and RMS is the fluctuation of the trace baseline. In order to reject accidental noise from pixels triggered by background light a minimum requirement on this ratio is set and usually only pixels with pulses having a S/N greater than 5 are kept for the subsequent analysis. The variables used in the reconstruction are the pulse time, t_i^{meas} , for each pixel i , and the total integrated signal, w_i . To determine all pixels connected to the shower image and further suppress noise pixels, a pattern recognition algorithm is used. The geometrical pointing direction, \vec{p}_i together with the signals determines the plane containing both the air shower and the track on the camera called Shower Detector Plane (SDP)

$$Q^2 = \sum_i w_i [\vec{p}_i \cdot \vec{n}], \quad (2.26)$$

where \vec{n} denotes the searched vector normal to the SDP. The Q^2 should be 0 in the ideal case. An illustration of the SDP is given in Fig. 2.10.

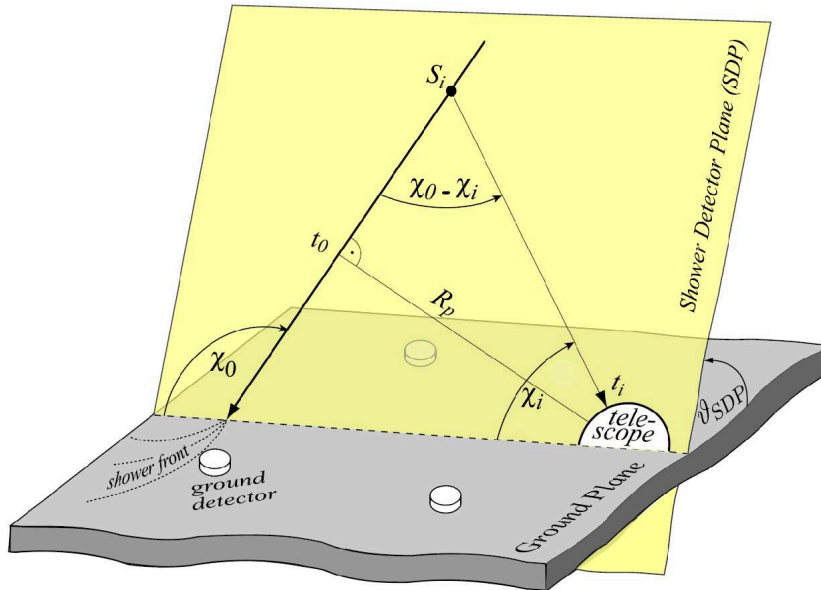


Figure 2.10: Illustration of the hybrid shower detector plane.

In order to determine the position of the shower within the SDP it is necessary to estimate the impact parameter R_p (i.e. the position of the shower core), the corresponding time T_0 and the angle between the shower axis and the ground plane χ_0 . The pointing directions of the pixels can be translated into an elevation angle $\tilde{\chi}_i$. The minimization of the following χ^2 leads to the determination of the position of the shower axis inside the SDP [137]

$$\chi^2 = \sum_i \left(\frac{t_i - t_i^{\text{meas}}}{\sigma_{t_i}} \right)^2, \quad (2.27)$$

where t_i is the theoretical expectation for the pulse time

$$t_i = T_0 + \frac{R_p}{c} \cdot \tan \left(\frac{1}{2} \cdot (\chi_0 - \tilde{\chi}_i) \right) \quad (2.28)$$

given by geometrical considerations. The correlation between the variables is large, a slight deviation in the elevation angle χ_0 induces a big change of the other two parameters. This degeneracy can be broken by adding timing information from a single SD station. Assuming a plane shower front, the expected trigger time of the station is given by:

$$t_i^{\text{meas}} = T_0 + \frac{1}{c} \vec{R} \cdot \vec{n}, \quad (2.29)$$

where \vec{R} is the position of the station with respect to the eye and \vec{n} is the shower direction. The station is chosen from those that are within 2 km from the intersection of the axis and the ground. In most cases the station with the highest signal satisfies these requirements.

The analysis of laser shots [138] suggests that the directional uncertainties of the SDP reconstruction are of an order of 0.1 degree in the case of hybrid events.

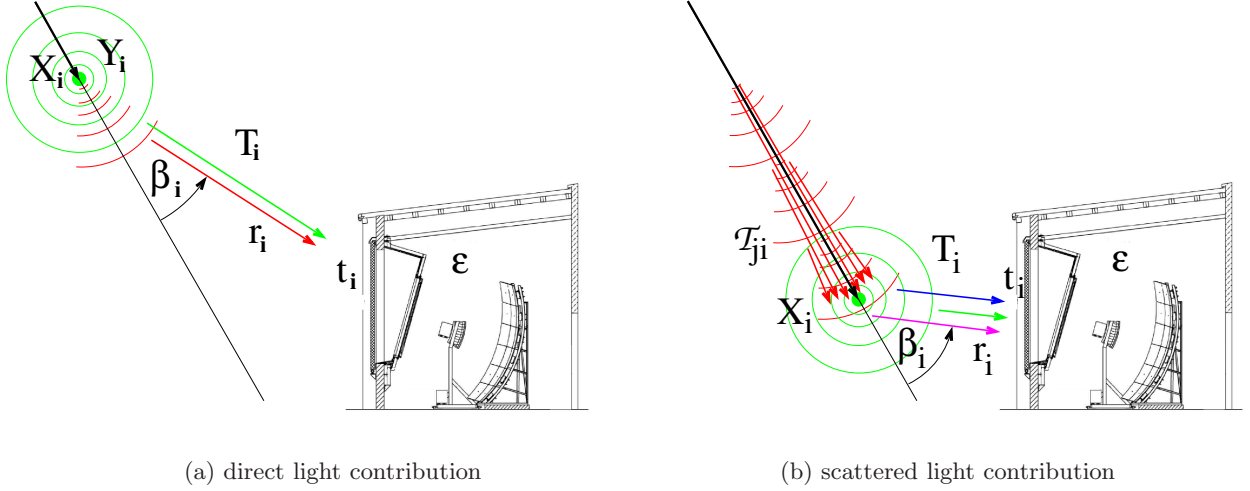


Figure 2.11: Illustration of the light flux received at the FD. Green: Isotropic fluorescence light, red: forward direct Cherenkov light, blue: Rayleigh-scattered Cherenkov light, and magenta: Mie-scattered Cherenkov light [144].

Energy reconstruction The two major contributions to the light at the FD aperture are the fluorescence light from nitrogen molecules and Cherenkov radiation photons [139–143]. Both contributions are affected by scattering and absorption in the atmosphere. The important scattering processes are Rayleigh scattering, when photons are scattered by particles much smaller than their wavelength, and Mie scattering, from particles larger than about tenfold of the light wavelength.

The amount of fluorescence light is directly proportional to the energy deposited by the air shower along its path in the atmosphere. Given the fluorescence yield Y_i^f [145–147] at a point in the atmosphere, the number of photons produced by the shower is

$$N_\gamma^f(X_i) = Y_i^f dE/dX_i, \quad (2.30)$$

where dE/dX_i denotes the energy deposited at slant depth X_i .

Due to Rayleigh and Mie attenuation only a fraction of the photons, T_i , can be detected at the aperture, as sketched in Fig. 2.11. The direct fluorescence light emitted at this slant depth is measured at the detector at time t_i . Given the light detection efficiency of ε and aperture A , the fluorescence light flux y_i^f measured at the FD is

$$y_i^f = \frac{A \varepsilon T_i}{4 \pi r_i^2} Y_i^f dE/dX_i, \quad (2.31)$$

The number of photons emitted through Cherenkov radiation is proportional to the number of charged particles above a certain energy cutoff, which is in a good approximation just the number of electrons and positrons,

$$N_\gamma^C(X_i) = Y_i^C N_e(X_i). \quad (2.32)$$

Chapter 2. The Pierre Auger Observatory

The threshold energy with the height is included in the Cherenkov yield Y_i^C [148–151]. Given the fraction $f_C(\beta_i)$ of photons emitted at an angle β_i with respect to the shower axis, the light flux at the FD aperture originated from direct Cherenkov light is

$$y_i^{\text{Cd}} = \frac{A \varepsilon T_i}{4 \pi r_i^2} f_C(\beta_i) Y_i^C N_e(X_i). \quad (2.33)$$

Although the Cherenkov photons are emitted in a narrow cone along the particle direction, they cover a considerable angular range with respect to the shower axis, because the charged particles are deviated from the primary particle direction due to multiple scattering. Due to the forward peaked nature of the Cherenkov light production, an intense Cherenkov light beam can build up along the shower as it traverses the atmosphere (cf. Fig. 2.11(b)). If a fraction $f_s(\beta_i)$ of the beam is scattered towards the detector it can contribute significantly to the total light received. In a simple one-dimensional model the number of photons in the beam at depth X_i is just the sum of Cherenkov light produced at all previous depths X_j attenuated on the way from X_j to X_i by \mathcal{T}_{ji} :

$$N_\gamma^{\text{beam}}(X_i) = \sum_{j=0}^i \mathcal{T}_{ji} Y_j^C N_e(X_j). \quad (2.34)$$

In analogy to Eq. 2.33 the scattered Cherenkov light received at the detector is

$$y_i^{\text{Cs}} = \frac{A \varepsilon T_i}{4 \pi r_i^2} f_s(\beta_i) N_\gamma^{\text{beam}}(X_i). \quad (2.35)$$

The total light received at the detector at the time t_i is obtained by adding the scattered and direct light contributions:

$$y_i = y_i^{\text{Cs}} + y_i^{\text{Cd}} + y_i^{\text{f}}. \quad (2.36)$$

To obtain the shower energy from the light at the aperture, the energy deposited in the atmosphere has to be determined. The total energy deposit is just the sum of the energy loss of electrons in the atmosphere, dE/dX_i which is related to the number of electrons $N_e(X_i)$ via

$$dE/dX_i = N_e(X_i) \int_0^\infty f_e(E, X_i) dE/dX_e(E, X_i) dE, \quad (2.37)$$

where $f_e(E, X_i)$ denotes the normalized electron energy distribution and $dE/dX_e(E, X_i)$ is the energy loss of a single electron with energy E . The electron energy spectrum $f_e(E, X_i)$ is universal in shower age [148, 150, 151], i.e. it does not depend on the primary mass or energy and since the electron energy loss depends only weakly on the local density, Eq. (2.37) is simplified to

$$dE/dX_i = N_e(X_i) \alpha_i. \quad (2.38)$$

Here α_i is the average energy deposit per electron at shower age $s_i = 3/(1+2X_{\text{max}}/X_i)$, where X_{max} denotes the shower maximum. It is parameterised from simulations as given in [151].

In general the FD will not be able to observe the full profile because of its limited field of view. Since for the calculation of the Cherenkov beam and the shower energy the full profile

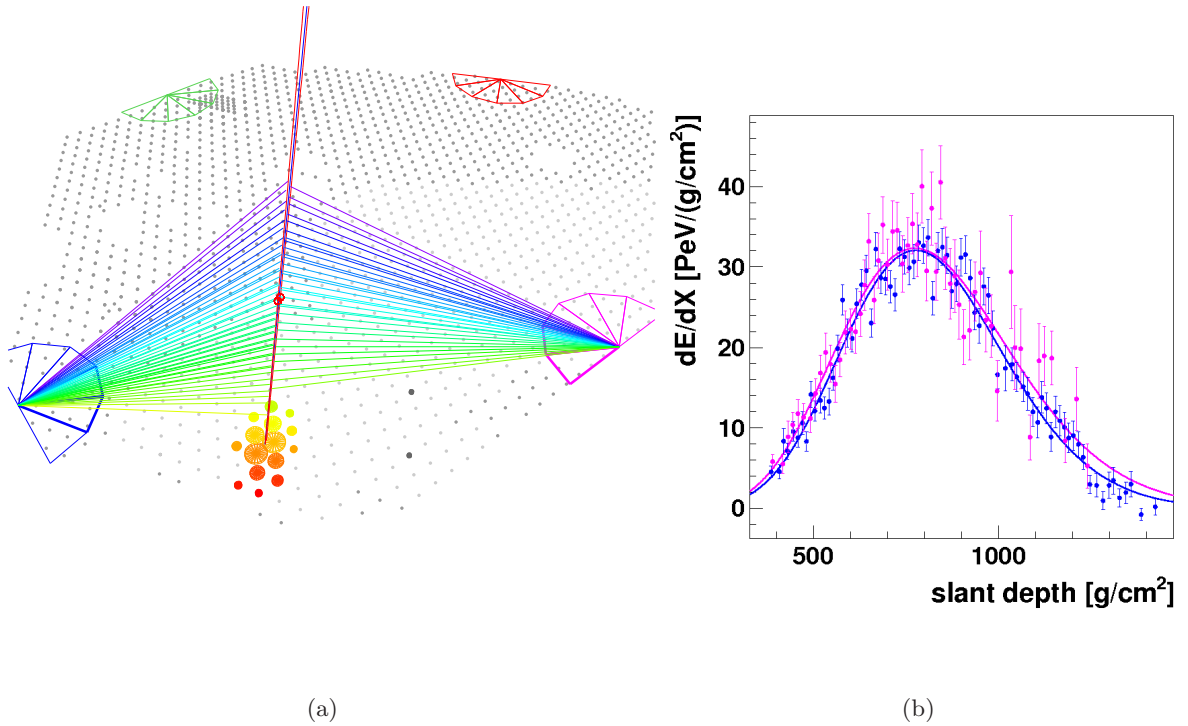


Figure 2.12: (a) Example of a golden stereo hybrid event (id 200923507306). (b) Corresponding longitudinal profiles.

is required, the extrapolation to depths outside the field of view is done with a Gaisser-Hillas function [152]. This function gives a good description of existing fluorescence data [153]

$$f_{\text{GH}}(X) = dE/dX_{\text{max}} \cdot \left(\frac{X - X_0}{X_{\text{max}} - X_0} \right)^{(X_{\text{max}} - X_0)/\lambda} e^{(X_{\text{max}} - X)/\lambda}, \quad (2.39)$$

where X_{max} is the depth where the shower reaches its maximum energy deposit dE/dX_{max} , X_0 and λ are shape parameters.

The electromagnetic energy is given by the integral over the energy deposit profile

$$E_{\text{em}} = \int_0^{\infty} f_{\text{GH}}(X) dX. \quad (2.40)$$

Not all of the energy of a primary cosmic ray particle is going into the electromagnetic part of an air shower. Neutrinos escape undetected and muons need long path lengths to release their energy. This invisible energy is usually accounted for by multiplying the electromagnetic energy Eq. (2.40) with a correction factor f_{inv} determined from shower simulations to obtain the total primary energy

$$E_{\text{tot}} = f_{\text{inv}} E_{\text{em}}. \quad (2.41)$$

Due to the energy dependence of the meson decay probabilities in the atmosphere, and thus the neutrino and muon production probabilities, the correction depends on the energy [154] and is also subject to shower-to-shower fluctuations [155].

Statistical uncertainties of the total energy The uncertainties of dE/dX_{\max} , X_{\max} , X_0 and λ obtained after the fit of the profile with Eq. (2.39), reflect only the statistical uncertainty of the light flux, $\sigma_{\text{flux}}(E_{\text{em}})$. Additional uncertainties arise from the uncertainties on the core location and shower direction (σ_{geo}) and the correction of invisible energy (σ_{inv}). The statistical variance of the total energy is

$$\sigma_{\text{stat}}(E_{\text{tot}})^2 = E_{\text{tot}}^2 \sigma(f_{\text{inv}})^2 + \left(\frac{df_{\text{inv}}}{dE_{\text{em}}} E_{\text{em}} + f_{\text{inv}} \right)^2 (\sigma_{\text{geom}}(E_{\text{em}})^2 + \sigma_{\text{flux}}(E_{\text{em}})^2). \quad (2.42)$$

Air showers detected with more than one eye (Fig. 2.12(a)) offer the opportunity to compare two independent energy estimations of the same event. The energy resolution deduced from these so-called stereo events is about 9 – 10%, independent of the availability of the Mie calibration constants. It was shown that the energy resolution from simulated data is of about 8% [144].

Systematic uncertainties of the energy scale The dominating source of systematic uncertainty for the energy estimation is the absolute fluorescence yield (14% [145, 147]). Further systematic uncertainties are related to the absolute detector calibration (9.5% [156]) and its wavelength dependence (3%). The lateral distribution Cherenkov light leads to a 5% increase of the reconstructed energy [157]. Correcting the finite spot size of the optical systems and its halo leads to an additional 3 – 5% increase. A small energy bias of about 3% has been observed in the reconstruction of MC simulations. It is related to the uncertainty in the constraints imposed to the Gaisser-Hillas parameters λ and X_0 . The correction for the invisible energy is known to 4% [158]. Atmospheric effects like the temperature and humidity dependence of the fluorescence yield leads to a combined altitude dependence of about 10%. The uncertainties of the aerosol content of the atmosphere contribute 5% [135]. The total systematic uncertainty of the energy determination can be estimated as 22% [125, 127, 159].

Offline software framework

The Offline software framework has been developed within the Pierre Auger Collaboration to perform the computing tasks [107, 160, 161]. It is designed to provide all functionality for processing data from the shower detector, including simulation and reconstruction, implemented in C++. All parts of the detector can be asked for their detailed status and configuration for all times the experiment was taking data. This includes configuration and size of the surface array, the status of each individual surface station, detailed configuration of the FD detector, uptime information for all relevant parts of the detector and all kind of atmospheric monitoring data. The data needed to retrieve the information are stored in XML files, if they are static and in SQL databases if they vary. The Offline framework provides an easy-to-use interface, making possible to modify the codes and to include new tasks, completely hiding the detailed internal mechanisms of how and where the data are taken from. In this way the users can contribute to the development of the software. There is also a general purpose ROOT-based [162] file format to store the results from SD, FD as well as hybrid event reconstruction, called *advanced data summary trees* (ADST) [163, 164]. It allows all members of the Auger Collaboration to work with up-to-date reconstructed data, without requiring to install, configure and run the heavy Offline framework. Only a valid

ROOT installation is necessary. All reconstructed and simulated data used for the analysis done in this work are in the ADST format.

Chapter 3

Studies of mass composition of ultra high energy cosmic rays with the Pierre Auger observatory

As it was mentioned in Chapter 1, it is possible to infer the composition of UHECRs from the characteristics the air-showers they produce when they interact with the atmosphere. The capabilities of the detectors of the Pierre Auger Observatory make it possible to find several observables which can give information about the nature of the primary cosmic ray. In this chapter the mass composition sensitive parameters provided by the FD and by the SD are described and some of the preliminary results are given.

3.1 The depth of the shower maximum, X_{\max}

The depth of the shower maximum, X_{\max} , is defined as the depth in the atmosphere at which the maximum number of particles in the shower is reached. It is the most mass-sensitive observable and is obtained directly from the longitudinal profiles observed by the fluorescence telescopes. Since heavy primary particles produce a greater amount of secondary particles than the light ones at a certain depth, X_{\max} is reached later for the light masses than for the heavy ones. Thus X_{\max} can be used to infer the mass of the primary particle comparing its value for different showers as shown in Fig. 3.1.

A technique to study changes in the mass composition of cosmic rays involves the rate of change of the mean value of X_{\max} with the energy. This is the so called elongation rate D_{10} , which depends on the mean logarithmic primary mass $\langle \ln A \rangle$. This definition comes from cascade theory and the simple Heitler model already mentioned in Chapter 1, which predict that the average depth of shower maximum is proportional to $\ln E$ [75, 166–168]

$$\langle X_{\max} \rangle_{\gamma} = D_{\gamma} \ln E + c_{\gamma}, \quad (3.1)$$

where D_{γ} is the electromagnetic elongation rate which corresponds to the radiation length X_{rad} in air for low energies, and c_{γ} is the corresponding absolute depth scale. It is possible

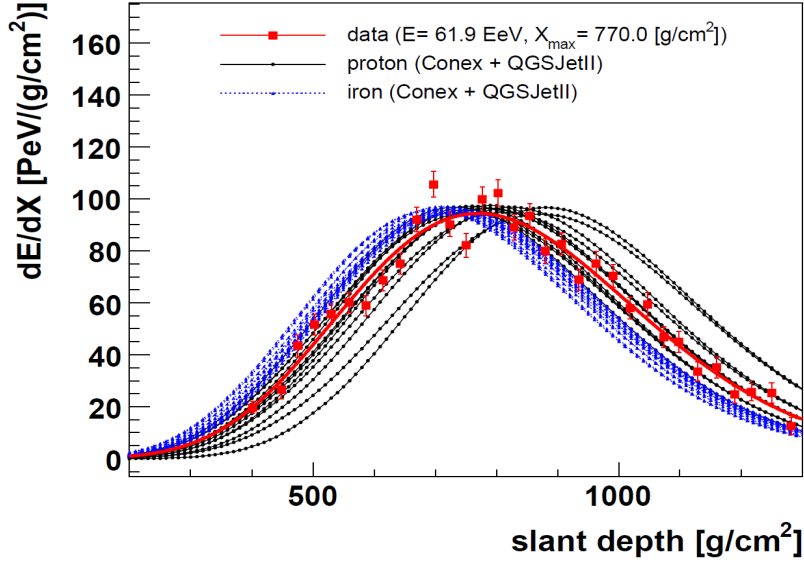


Figure 3.1: Comparison of longitudinal energy deposit profiles between a measurement (red squares) with proton (black solid lines) and iron (blue dotted lines) CONEX simulations [165].

to derive a similar form for proton initiated showers

$$\langle X_{\max} \rangle_p = D_p \ln E + c_p, \quad (3.2)$$

where $D_p = \frac{d\langle X_{\max} \rangle_p}{d \ln E}$ is the proton elongation rate and is related to D_γ by the elongation rate theorem

$$D_p \leq D_\gamma, \quad (3.3)$$

which establish the assumption that in hadronic interactions the multiplicity and the interaction length never decrease with energy [169]. Taking into account the superposition model, in which a nucleus with mass A and energy E is equivalent to A protons with energy $\frac{E}{A}$, the mean X_{\max} becomes

$$\langle X_{\max} \rangle_A = D_p \ln \left(\frac{E}{A} \right) + c_p \quad (3.4)$$

and for a mixed primary composition with average logarithmic mass $\langle \ln A \rangle$ one obtains

$$\langle X_{\max} \rangle = D_p (\ln E - \langle \ln A \rangle) + c_p. \quad (3.5)$$

The above equations are still valid if the fragmentation of nuclei is also taken into account, through the semi-superposition model [170].

That means that given the values of D_p and c_p from high energy interaction models, $\langle \ln A \rangle$ can be derived from the measurement of X_{\max} . Since it was deduced that the absolute depth scale c_p is more uncertain than its energy dependence D_p [171], it is possible to use the observed elongation rate to measure the change in composition with energy independently of c_p by

$$D_{10} = \frac{d\langle X_{\max} \rangle}{d \ln E} = D_p \left(1 - \frac{d\langle \ln A \rangle}{d \ln E} \right). \quad (3.6)$$

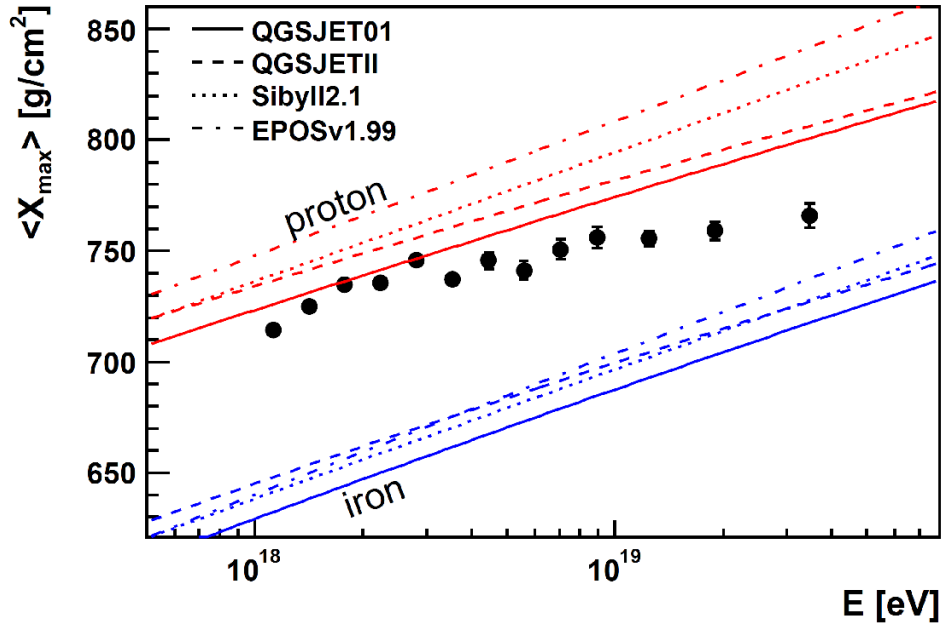


Figure 3.2: The average X_{\max} as a function of energy (black dots) plotted with predictions of protons and iron nuclei from four hadronic interaction models (lines) [173].

For instance, if an elongation rate $D_{10} > D_{\gamma}$ is observed it follows from equations 3.3 and 3.6 that a transition to lighter elements ($\frac{d(\ln A)}{d \ln E} < 0$) can be concluded independently from details of hadronic interaction models [172]. Figure 3.2 [173] shows the latest results measured by the Pierre Auger Observatory, it suggests that the composition is getting heavier at high energies but it still remains a mixed mass composition.

Fluctuations in $\langle X_{\max} \rangle$ It was deduced from the semi-superposition model, that taking into account a realistic distribution of the positions of the first interactions of nucleon showers, there are wide fluctuations. Those fluctuations can reflect correlations among nucleons in the same nucleus. Each interaction of nucleons can be considered as producing a separate sub-shower. Therefore heavy nuclei will produce more interactions, resulting in smaller fluctuations in the first part of the shower but also in the later part, than light nuclei, which will present more fluctuations. Since the shower size and X_{\max} are fully determined by the energy of the primary nucleus in this model, the fluctuations of the first interaction induce corresponding fluctuations in X_{\max} [170]. Also hadronic interaction features extrapolated from accelerator data to ultra-high energies for air shower development have shown to have a large impact on air shower observables, more than fluctuations induced by just considering the properties of the single first interaction [174]. Thus, fluctuations on X_{\max} can be also used to distinguish between different primary masses. Figure 3.3 [173] shows fluctuations of X_{\max} obtained by the Pierre Auger Observatory. It also suggests a heavy composition at highest energies, even heavier than the one inferred from the mean X_{\max} . The discrepancy is smallest for EPOS model, for which the two measurements could be consistently interpreted within their systematic uncertainties. Given the unexpected trend to heavier composition and the

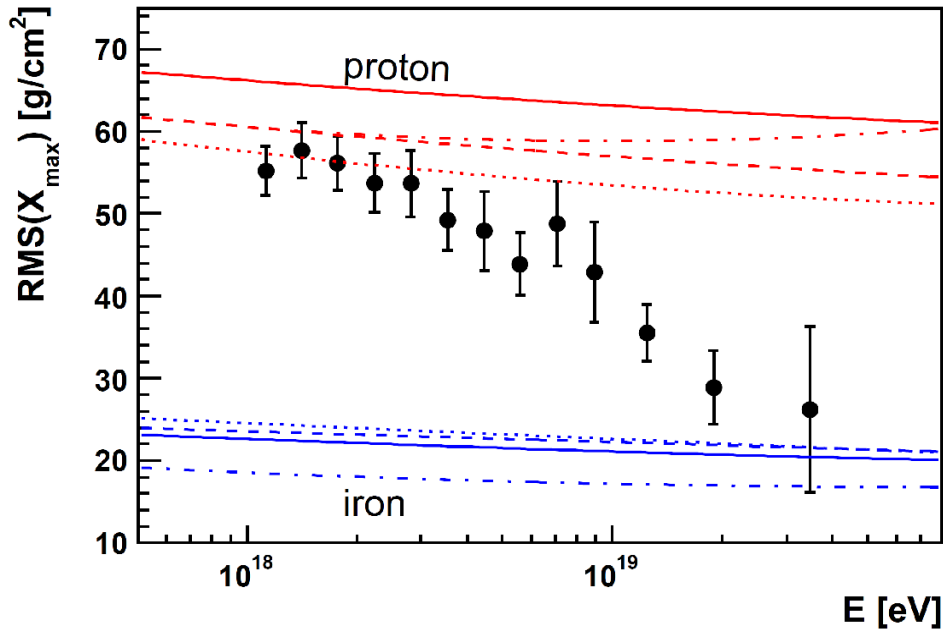


Figure 3.3: Fluctuations on X_{\max} as a function of energy plotted with predictions of protons and iron nuclei from four hadronic interaction models (as in Fig. 3.2) [173].

difficulty of reconciling models with FD measurements it is important to verify the results on X_{\max} obtained from the FD, taking the advantage of the high statistics of the SD detectors. In this thesis a method to infer X_{\max} from SD is proposed.

3.2 Ratio of muon to electromagnetic particles in the shower

Muons produced in EAS can be used to study the chemical composition of primary cosmic rays because their multiplicity depends on the atomic number of the primary particle [143]. This dependence can be explained from the development of the shower in the atmosphere. Muons are produced from the decay of charged pions. The rate of decay depends on its energy, as this determines the decay length, λ , and on the density of the atmosphere, ρ , as this determines the likelihood that the particle will interact before decaying. The probabilities to decay and interact become equal when

$$\Gamma\tau c = \frac{\lambda}{\rho}, \quad (3.7)$$

where Γ is the Lorentz factor and τ is the pion lifetime [175]. Because of this competition between interaction and decay, as the pion energy increases, higher energy pions are less likely to decay. Energy conservation requires that, if the muon number increases, the number of electromagnetic particles in the shower must be reduced and one would expect an increase in the ratio of muons to electrons in showers initiated from more massive primaries. This can be seen most simply by comparing what one expects for protons and iron primaries. In the simple superposition model of nuclear interactions, an interacting Fe nucleus of energy E_0

breaks up and produces 56 individual EAS, each of which is generated by a nucleon of energy $E_0/56$. The resulting pions in each EAS will have smaller average energies than they would for a proton induced EAS of the same energy. More of such low energy pions will decay to muons before interacting because the decay length has decreased while the interaction length is approximately the same. One may also expect that the pion multiplicity will be larger for Fe initiated showers. Furthermore, since Fe nuclei interact higher in the atmosphere than protons, Fe and p nuclei of the same energy will not produce the same number of electromagnetic particles. In general, Fe nuclei will produce less than p nuclei.

Composition studies using data of the Pierre Auger Observatory can exploit the response of the SD detectors to single muons. The time structure of the FADC traces shows peaks corresponding to muonic signals, which can be well distinguished. Using this characteristic it is possible to count the number of muons. Examples of methods to analyze the FADC traces are the use of deconvolution algorithms to remove the electromagnetic signal [176] and the identification of *jumps* in the FADC traces induced by single muons [177]. Simulations are important to compare the obtained results.

3.3 The lateral development of the shower

Showers arriving at the ground are detected at a specific stage of lateral development. This stage is observed in the lateral particle density as a function of the distance to the shower axis. This density distribution is determined by the distribution of the transverse momenta of the pions ancestors of the ground particles and the multiple scattering of the electromagnetic component of the shower [143]. The particle density decreases with the distance to the shower axis because the electromagnetic component becomes more attenuated at larger distances. In the case of late interacting showers this decrease occurs faster than in the case of early interacting showers of the same energy. In the Pierre Auger Observatory the lateral particle density is parameterised by a lateral distribution function (LDF), which is based on the one used by the Haverah Park experiment [178]. The advantage of that experiment for developing an experimentally verified LDF parameterisation was its dense array of detectors in the center of the experiment. The Haverah Park experiment used water Cherenkov detectors, as the Pierre Auger Observatory does [120]. This LDF has an NKG-type, as described in Chapter 2

$$S(r) = S_{1000} \left(\frac{r}{1000 \text{ m}} \right)^\beta \left(\frac{r + 700 \text{ m}}{1700 \text{ m}} \right)^\beta, \quad (3.8)$$

where $S(r)$ is the particle density at a given distance r to the core, and β is the steepness parameter. The β parameter and its fluctuations are sensitive to mass composition because they must change with X_{max} . The LDF has primarily been used to estimate the energy of the shower from SD data, and in such analysis it was useful to keep β fixed. Furthermore the spacing of 1500 m between the tanks on the SD makes the measurement of β on an event by event basis difficult. But at the present there are some studies to determine the LDF using the recently deployed infill array [179], which will allow using β for mass composition studies in the future.

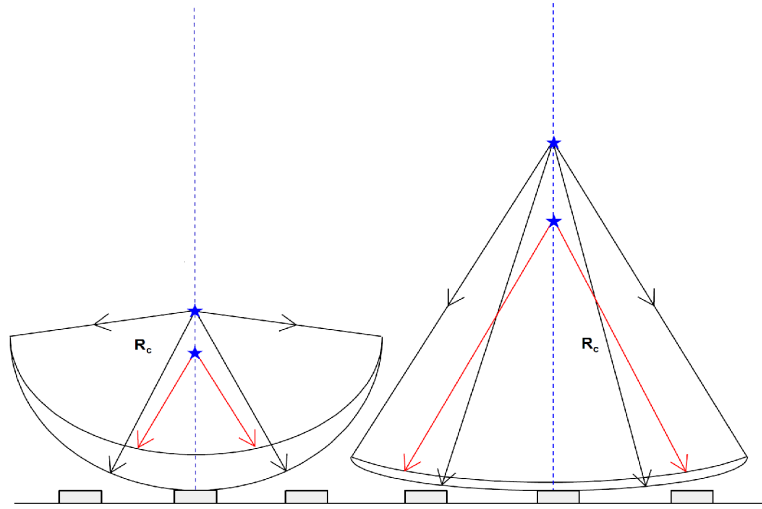


Figure 3.4: Diagram of R_c . Left: light mass primary particle shower. Right: heavy mass primary particle [175].

3.4 Radius of curvature R_c

We model the shower front as a sphere which is propagating along the shower development following the geometrical paths of the muons produced at a point source at the shower axis (see Chapter 2). That sphere has a radius of curvature R_c , which increases with the propagation of the surface of the sphere to the ground (Fig. 3.4). Even though the spherical model is an ideal approximation of the shower front, it can be used to reproduce the height of production of muons in the shower, to estimate the arrival times of particles at the stations [180] and to correct the reconstruction of the arrival direction of the showers [181]. Furthermore, since R_c is directly related to the depth of the first interaction X_0 , it can be used as a parameter to infer the mass composition. For example, an iron primary has a shorter mean free path in air than proton or photon primaries. The initial point of the shower is higher in the atmosphere, resulting in a shallower X_{\max} and a larger R_c . Photon showers develop closer to the ground and have a smaller radius of curvature [182]. A plot with the first results using R_c as mass composition parameter is shown in (Fig. 3.5).

3.5 Time structure of the signal of air shower particles

The time structure of the signal has been studied extensively. At the Volcano Ranch array it was discovered that the arrival times of particles were spread out over several hundred nanoseconds at several hundred meters from the shower axis, a spread that increased with distance. At Haverah Park it was possible to study the time structure of the shower front on an event by event basis, and to establish that the temporal fluctuations were correlated with fluctuations in the lateral distribution of the water Cherenkov signal; showers with steeper than average lateral distributions had broader time spreads than on average [50]. Since the

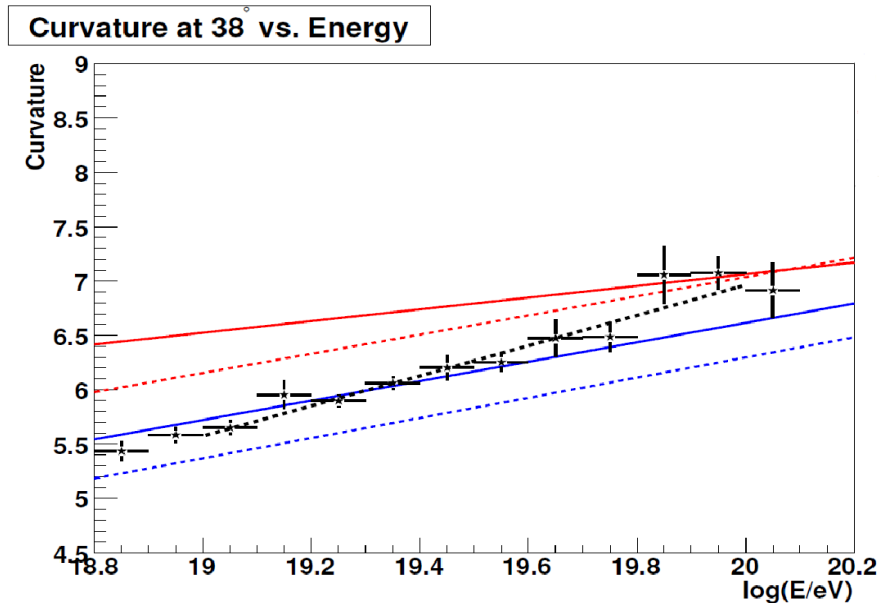


Figure 3.5: R_c from Monte Carlo predictions and data. Blue lines show proton, red lines show iron (solid = QGSJET01, dashed = Sibyll 2.1), and black dashed line shows data [183].

steepness changes with X_{\max} as mentioned in Section 3.3, the spread in arrival times of particles is larger for showers which develop later in the atmosphere than their shallower counterparts.

Besides the studies mentioned in Section 3.2 the detailed time structure of the FADC traces provide additional composition sensitive information which are defined from the FADC trace itself. Here two of these are described: the risetime $t_{\frac{1}{2}}$ and parameters derived from it as the “Time Asymmetry Parameters”, as well as $\langle \Delta_i \rangle$ and $\langle \Delta_{1000} \rangle$.

Risetime $t_{\frac{1}{2}}$ and $t_{\frac{1}{2}}(1000 \text{ m})$ The risetime is defined as the time for the integrated signal in an SD tank to rise from 10% to 50% of the final value (Fig. 3.6(a)). The study of the evolution with time of this fixed segment of the integrated signal allows the measurement of the spread in arrival times of cascade particles. It reflects the depth of the shower development and the ratio of muon to electromagnetic particles. Muons travel in approximately straight lines through the atmosphere and arrive earlier than the electromagnetic particles which scatter multiple times before they reach the ground (Fig. 3.6(b)). Therefore, the most of the particles which compose the early signal of an SD tank are muons while the later signal is composed of electromagnetic particles. If a shower has more muons, as for example an iron shower, it will have a shorter risetime than a proton induced shower. Furthermore when a primary penetrates deep in the atmosphere, as a proton does, it will have a longer risetime than a shallow primary, like iron. The possibility to distinguish between different kinds of shower primary particles from the risetime leads to use it as a mass composition parameter.

The first studies of $t_{\frac{1}{2}}$ using data of the Pierre Auger Observatory were based on the risetime

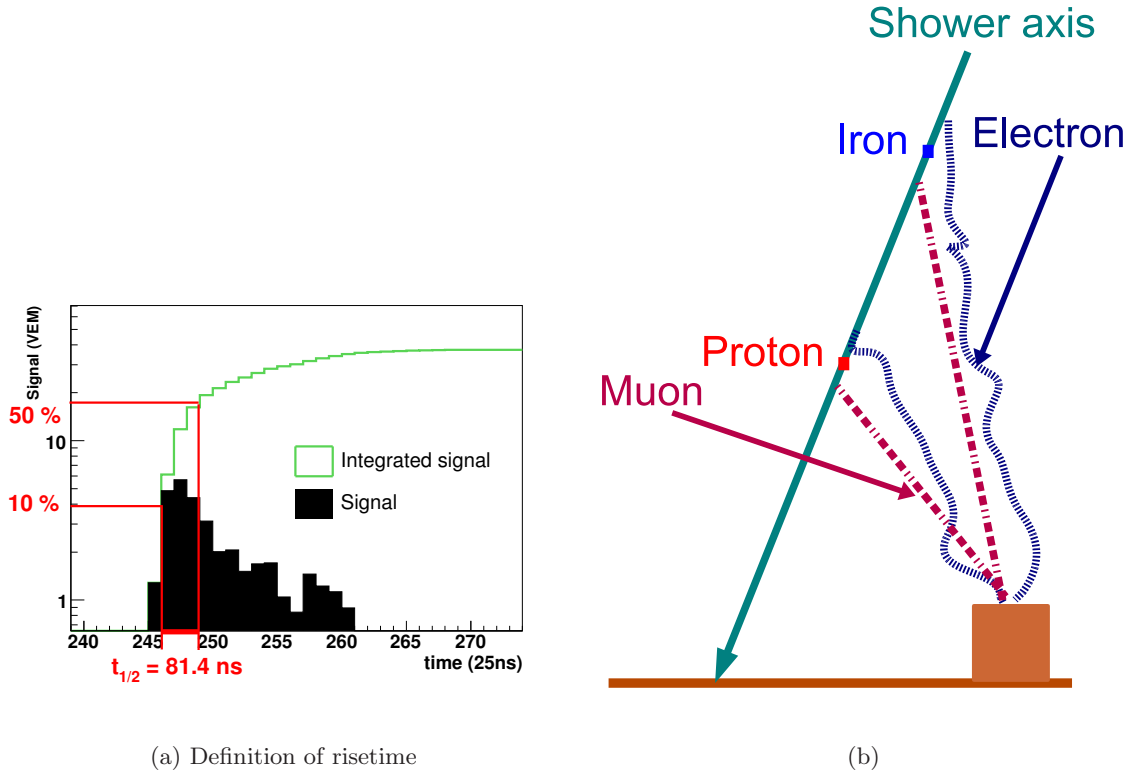


Figure 3.6: (a) Risetime of a simulated signal [185]. (b) Particles traveling different paths.

at 1000 m from the shower core, $t_{\frac{1}{2}}(1000 \text{ m})$ [184], obtained from the parameterisation

$$t_{1/2}(r, \theta) = 40 + a(\theta)r + b(\theta)r^2 \quad [ns]. \quad (3.9)$$

It was expected that $t_{\frac{1}{2}}(1000 \text{ m})$ changed with the energy but results showed that apparently there is no energy dependence (see Fig. 3.7). The results could also indicate that mass composition becomes heavier with energy [183]. Nevertheless this is not completely reliable because the flat distribution might be due to large fluctuations on the fit of the risetime as a function of the distance to the shower core on an event-by-event basis. Furthermore biases and deeper studies on the uncertainty of $t_{\frac{1}{2}}$ were not taken into account. Hence more studies on parameterisations of risetime are necessary (see Chapter 4) as well as the use of other parameters different from $t_{\frac{1}{2}}(1000 \text{ m})$ but related to the risetime. The next paragraphs are dedicated to those new parameters.

Time Asymmetry parameters The azimuthal symmetry of particle distributions in the shower plane, is broken when they are projected to the ground. As a consequence there is an azimuthal asymmetry on the signal features. This is due mainly to the different amounts of atmosphere traversed by different parts of the shower. More explanations on the origin of the asymmetry are given in Chapter 4. The azimuthal asymmetry is observed in $t_{\frac{1}{2}}$, thus, for a given primary energy E , the asymmetry depends on zenithal angle θ of the primary

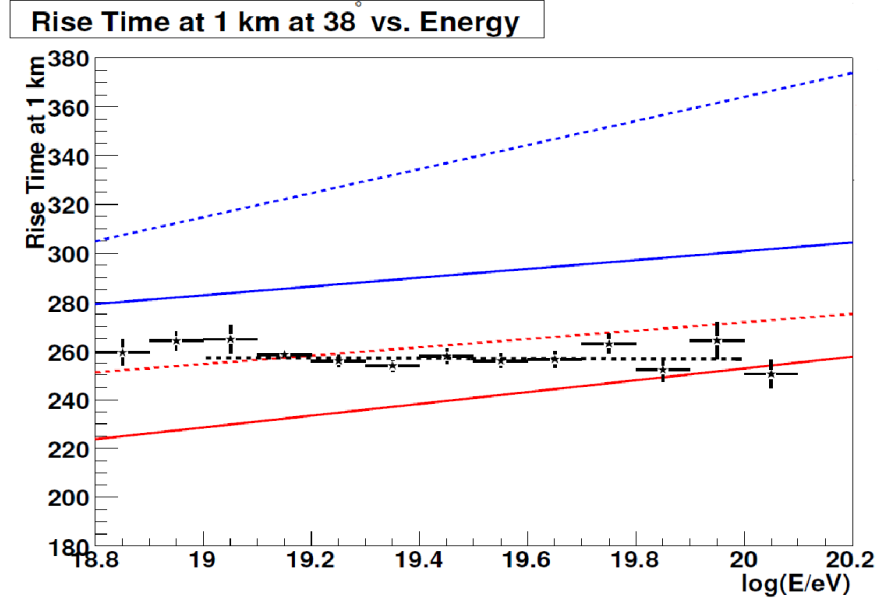


Figure 3.7: $t_{\frac{1}{2}}(1000 \text{ m})$ as a function of the energy compared with Monte Carlo predictions. Blue = proton, red = iron, solid = QGSJET01, dashed = Sibyll 2.1, and black dashed line = data.

cosmic ray in such a way that its behavior versus $\sec \theta$ is reminiscent of the longitudinal development of the shower. This “longitudinal development of the asymmetry” is strongly dependent on the nature of the primary particle. Studies based on Monte Carlo simulations exploiting parameters related to the azimuthal asymmetry of $t_{\frac{1}{2}}$ have been performed [186]. The asymmetry is parameterised using the following function

$$t_{\frac{1}{2}}(r, \theta, \zeta) = a + b \cos \theta \quad [ns]. \quad (3.10)$$

Parameters a and b define the “Time Asymmetry Parameters” as indicated in Fig. 3.8: $XAsymMax$, the position of the maximum asymmetry, i.e. the $\sec \theta$ value for which b/a is a maximum; $AsymHeight$, the height at maximum, and $XAsymWidth$, the half width at half maximum of the Gaussian function. The most sensitive of these parameters is $XAsymMax$ which can be used to discriminate between heavy and light composition (see Fig. 3.9(a)). A correlation of $XAsymMax$ with X_{\max} was found and used to infer the mass composition of showers. Plots in Fig. 3.9 show a mixed mass composition [187].

$\langle \Delta_i \rangle$ parameter The first step to defining this parameter is obtaining the so called benchmark, which is the average value of $t_{\frac{1}{2}}$ as a function of the core distance and the zenith angle for a given reference energy (10^{19} eV). Then, for each selected detector in a given event, the deviation of the measured $t_{\frac{1}{2}}$ from the benchmark function is calculated in units of measurement uncertainty, and averaged for all detectors in the event

$$\langle \Delta_i \rangle = \frac{1}{N} \sum_{i=1}^N \frac{t_{\frac{1}{2}}^i - t_{\frac{1}{2}}(r, \theta, E_{ref})}{\sigma_{1/2}^i(\theta, r, S)}, \quad (3.11)$$

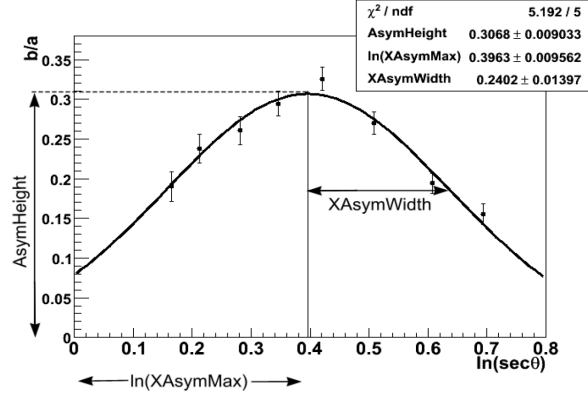
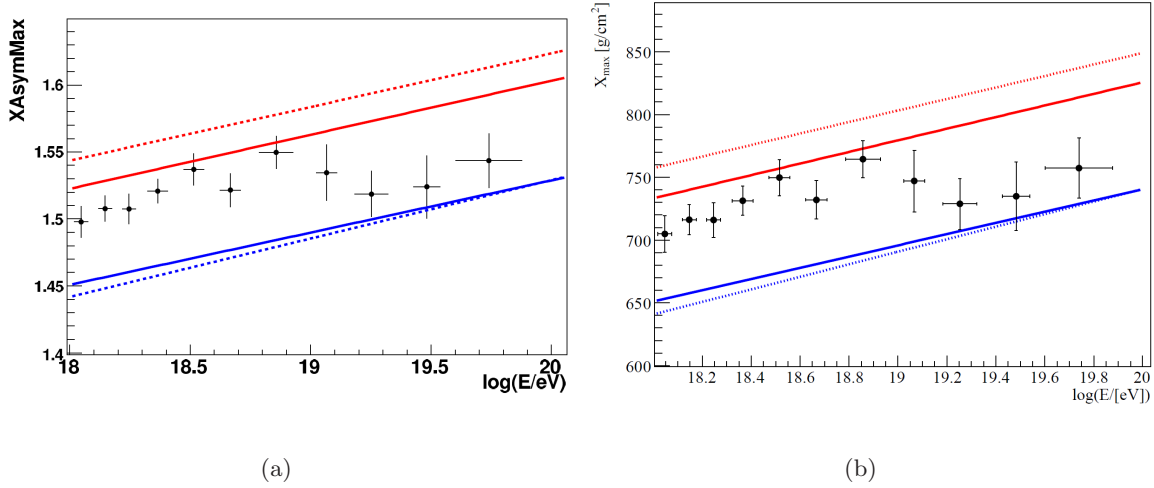


Figure 3.8: Parameters describing the asymmetry longitudinal development.



(a)

(b)

Figure 3.9: (a) $XAsymMax$ parameter vs $\log E$. (b) $\langle X_{max} \rangle$ vs $\log E$ inferred from $XAsymMax$ and Monte Carlo predictions (red lines: proton, blue lines: iron) from QGSJETII-03 (solid lines) and Sibyll 2.1 (dashed lines).

where $\sigma_{1/2}^i(\theta, r, S)$ stands for the uncertainty parameterised as function of zenithal angle, distance to the core and signal, S , of each detector. The $\langle \Delta_i \rangle$ is found to increase with energy as the showers become more penetrating in the atmosphere. Using hybrid events it can be shown that $\langle \Delta_i \rangle$ is proportional to X_{max} [188]. At present the uncertainties are quite large to be used in composition measurements on an event-by-event basis. Despite this, there is a clear correlation between the average $\langle \Delta_i \rangle$ and X_{max} for groups of showers, which means that, on an average basis, the X_{max}^{SD} , obtained from that correlation, can be used for composition analysis. Figure 3.10 shows the first results obtained from this parameter where a mixed mass composition of cosmic rays at very high energies is suggested [175].

$\langle \Delta_{1000} \rangle$ parameter This parameter is one of the main topics of this thesis. It is defined similarly to $\langle \Delta_i \rangle$ but using stead one, several benchmarks and taking into account the

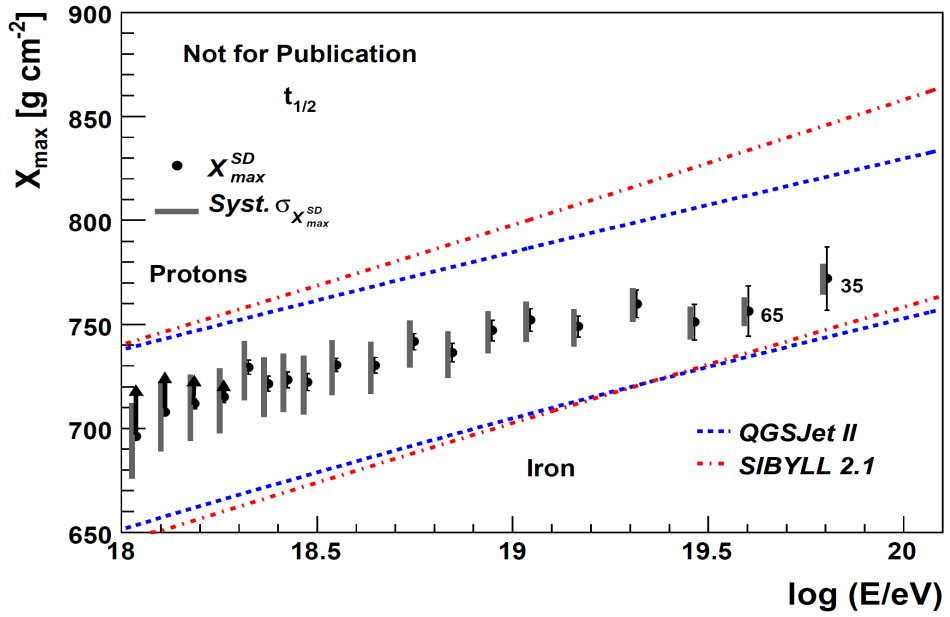


Figure 3.10: The average X_{\max}^{SD} as a function of energy plotted with predictions of protons and iron nuclei from two hadronic interaction models. The numbers denote the events in the given bins and the black arrows are the estimated corrections required due to loss of sensitivity to events at the lower energies.

corresponding risetime at 1000 m from the shower core. It is going to be explained with more detail in Chapter 5.

Chapter 4

The Risetime $t_{1/2}$, its uncertainty and asymmetry

The Risetime $t_{1/2}$ is one of the most studied mass-sensitive observables concerning the SD as mentioned in Chapter 3. In this chapter, the most important treatments, necessary for the correct use of this observable, are explained. These are basically the calculation of a proper uncertainty, $\sigma_{t_{1/2}}$, and the correction of the azimuthal asymmetry. A brief statement of $t_{1/2}(1000\text{ m})$ as mass-sensitive observable is presented.

4.1 Uncertainty of risetime $\sigma_{t_{1/2}}$

The use of a properly defined and understood uncertainty of $t_{1/2}$ is crucial for obtaining reliable results. It must be taken into consideration to quantify shower-to-shower fluctuations, or to test the agreement between the observed and predicted $t_{1/2}$ made by using Monte Carlo simulations. The uncertainty, $\sigma_{t_{1/2}}$, is an empirical approach proposed in Ref. [189]. The sources of $\sigma_{t_{1/2}}$ are detector effects and data treatment. As detector effects, the digitising of the signal by the FADCs [190] and the data sampling, can be mentioned. The reconstruction procedures performed by the software, as well as the asymmetry correction (explained in the next section), are additional sources of uncertainty.

Definition Stations belonging to different showers and located at different distances from the shower core, r , register different signals, S . The muon to electromagnetic ratio of the shower front changes with the zenith angle, θ , of the event, when it is registered at ground. The corresponding risetime presents fluctuations which may not be directly compared to calculate a measurement uncertainty. Therefore, only risetimes from stations within an event, and located at the same r can be directly compared. This is equivalent to compare risetime measurements with similar S , r and θ . Stations which present a similar r , and thus, a similar S , are the twins and triplets sets available in the SD array. These provide doublets stations separated by 11 m and located, 12 twins and 7 triplets, on a hexagonal grid, plus 3 more twins located on the standard grid [191]. Nevertheless, statistics from twins and triplets are not large enough, being necessary to devise the concept of *pairs* [192]. A pair consists of two

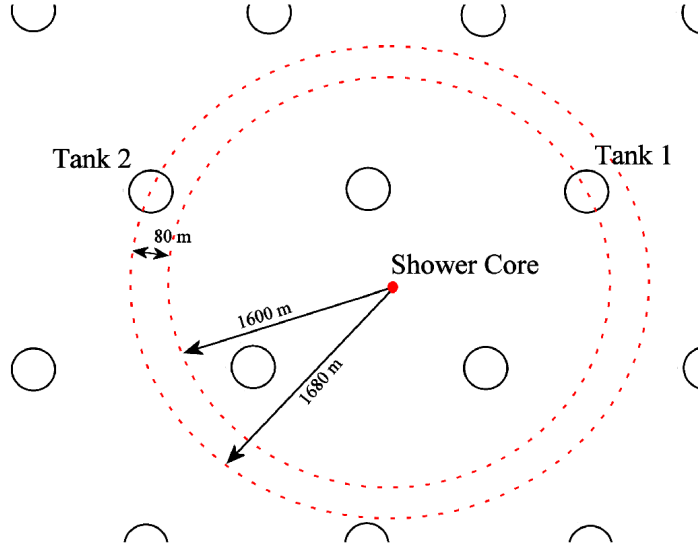


Figure 4.1: Diagram of the pairs of stations considered for the uncertainty of risetime $\sigma_{t_{1/2}}$, taken from [189].

stations belonging to the same event, having a difference in r of less than 100 m (see Fig. 4.1). The difference of risetime concerning the azimuthal angle of pair stations is removed by doing a preliminary asymmetry correction. Having two measurements of the same parameter from multiple observations, as in the case of $t_{1/2}$ from doublets, the measurement uncertainty can be calculated using

$$\sigma_{pair} = \frac{\sqrt{\pi}}{2} \cdot \langle |\Delta t_{1/2}| \rangle, \quad (4.1)$$

where $\langle |\Delta t_{1/2}| \rangle$ is the average absolute difference in the risetimes recorded by the doublet stations [193]. The uncertainty introduced due to the differences in r of pairs can be taken into account using

$$\sigma_{pair}^2 = 2 \cdot \sigma_{t_{1/2}}^2 + \sigma_{\Delta r}^2, \quad (4.2)$$

where $\sigma_{\Delta r}$ is given by

$$\sigma_{\Delta r} = \frac{\partial t_{1/2}}{\partial r} \cdot \langle |\Delta r| \rangle, \quad (4.3)$$

being $\langle |\Delta r| \rangle$ the average absolute difference in distance. The risetime is parameterised as a function of r , as explained in Section 4.3, using

$$t_{1/2}(r, \theta) = 40 + a \cdot r + b \cdot r^2, \quad (4.4)$$

resulting $\sigma_{\Delta r}$ in

$$\sigma_{\Delta r} = (a + 2 \cdot b \cdot r) \cdot \langle |\Delta r| \rangle, \quad (4.5)$$

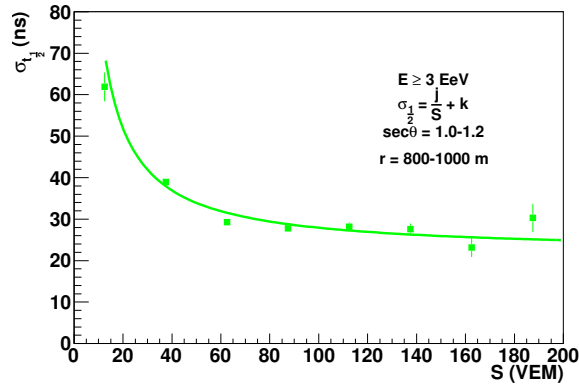


Figure 4.2: Dependence of the measurement uncertainty on the signal, as obtained from calculation of $\sigma_{t_{1/2}}$. The green line shows a fit using a function of the form $\sigma_{t_{1/2}} = \frac{j}{S} + k$.

the measurement uncertainty of risetime can therefore be found from equation 4.2 obtaining

$$\sigma_{t_{1/2}} = \sqrt{\frac{\sigma_{pair}^2 - \sigma_{\Delta r}^2}{2}}, \quad (4.6)$$

which is the expected value to be compared with observations.

Calculation The uncertainty is calculated for a set of pairs (from now on, this name refers to doublets and *pairs*), using the equation 4.6. The stations must have a signal above 10 VEM, not being saturated and have to be located within 2000 m of the shower core. The events containing the pairs must have an energy above 3 EeV, with zenith angles below 60° , the number of candidate stations (stations used for the shower reconstruction) must be above 5. The T4 trigger, defined in Chapter 2 is also required to ensure enough statistics. These conditions ensure that events of good quality are used for the analysis. The data are split into 5 bins of $\sec \theta$ and 8 bins of r . The measurement uncertainty of the risetime is observed to be strongly dependent on signal size. This is expected since fluctuations in risetime will be larger when fewer particles contribute towards the signal. Therefore, this dependence is used to explore the behavior of $\sigma_{t_{1/2}}$. The dependence of $\sigma_{t_{1/2}}$ on S for a given zenith angle and distance range is shown in Fig. 4.2.

The function used to describe the dependence is

$$\sigma_{t_{1/2}}(S) = \frac{j(r, \sec \theta)}{S} + k(r, \sec \theta). \quad (4.7)$$

The measurement uncertainty is also dependent on r , as shown in Figs. 4.3(a), 4.3(b) and 4.3(c). It is observed that for large distances, $\sigma_{t_{1/2}}$ increases, not only due to a drop in signal size, but due to the different composition of the shower front for different distances at a given signal size. A dependence on zenith angle is also observed since $\sigma_{t_{1/2}}$ decreases as $\sec \theta$ increases. It can be explained considering that showers produce shorter signals after

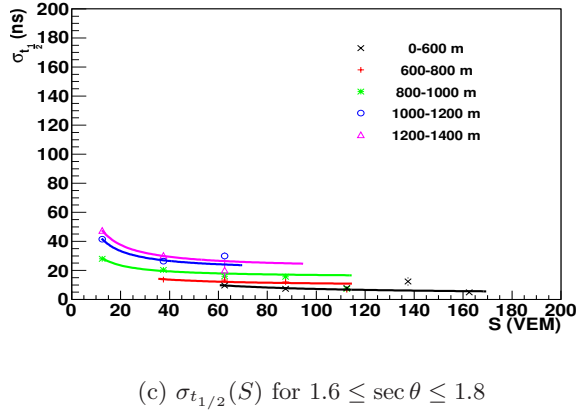
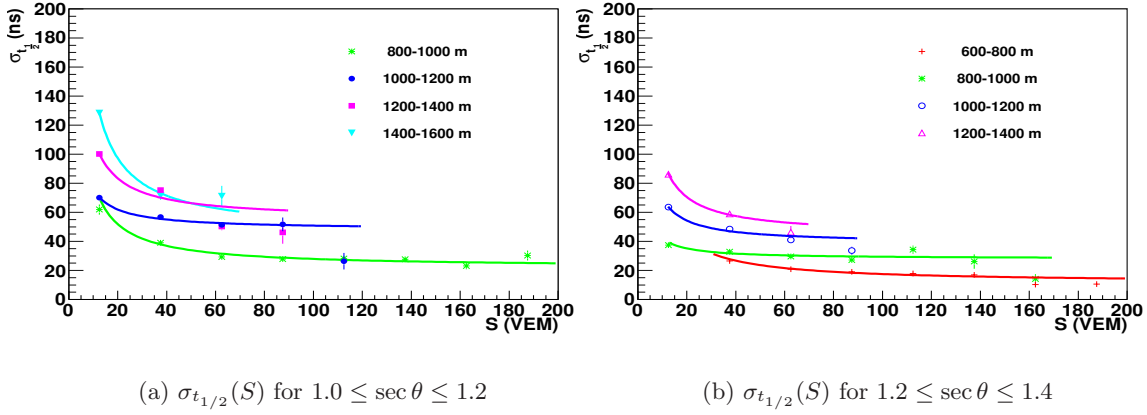


Figure 4.3: $\sigma_{t_{1/2}}(S)$ for three ranges of $\sec \theta$. The ranges of r shown correspond to the best fits obtained. For getting representative points in each bin of $\sigma_{t_{1/2}}$, the condition: $\sigma_{t_{1/2}}(S) \in [\langle \sigma_{t_{1/2}} \rangle - 2\sigma, \langle \sigma_{t_{1/2}} \rangle + 2\sigma]$, is imposed. $\langle \sigma_{t_{1/2}} \rangle$ is the mean value of the uncertainty in the bin and σ its spread. A minimum number of five entries per bin is required.

crossing greater atmospheric depths. This leads to a smaller uncertainty for more inclined showers.

All dependencies of $\sigma_{t_{1/2}}$ have to be taken into account for finding an adequate fit. Using a very first fit (the one shown in Fig. 4.3), the type of function which describes each dependence of the parameters, is found. The dependence on r of parameter j is described by a cubic polynomial as shown in Fig. 4.4(a). For parameter k , this dependence is described by a linear function as shown in Fig. 4.5(a). For both parameters, the dependence on zenith angle is described by a linear function, as shown in Figs. 4.4(b) - 4.4(d) and 4.5(b) - 4.5(c).

Thus, the final fit is obtained using the function 4.7, with

$$j(r, \sec \theta) = j_{a1} + j_{a2} \cdot \sec \theta + (j_{b1} + j_{b2} \cdot \sec \theta) \cdot r^2 + (j_{c1} + j_{c2} \cdot \sec \theta) \cdot r^3 \quad (4.8)$$

and

$$k(r, \sec \theta) = k_{a1} + k_{a2} \cdot \sec \theta + (k_{b1} + k_{b2} \cdot \sec \theta) \cdot r. \quad (4.9)$$

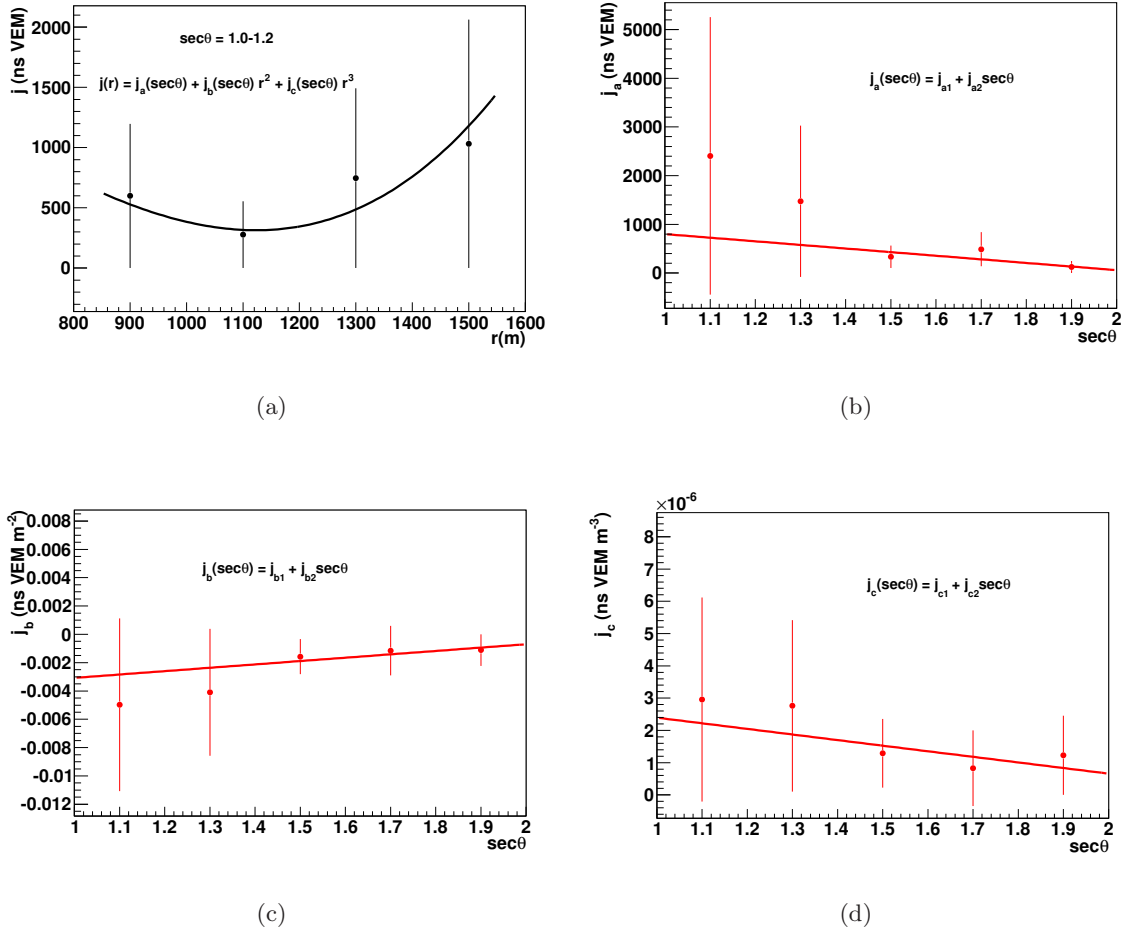


Figure 4.4: j parameter as a function of: (a) distance to the core, with a cubic polynomial fit and (b)-(d) zenith angle, with a linear function, respectively.

All available points contained in plots of $\sigma_{t_{1/2}}(S)$ for 8 ranges of r and 5 ranges of zenith angle, are considered at the same time. The plots must fulfill the condition $\sigma_{t_{1/2}}(S) \in [\langle\sigma_{t_{1/2}}\rangle - 3\sigma, \langle\sigma_{t_{1/2}}\rangle + 3\sigma]$ for each bin, where $\langle\sigma_{t_{1/2}}\rangle$ is the mean value of the uncertainty in the bin and σ is the spread. This condition eliminates points which are far from the mean value and reduces the spread caused by those points. A minimum number of five entries per bin and 40 points per plot are also required. The best fit is the one which minimizes the χ^2 . The obtained values are shown in table 4.1. Figure 4.6 shows the new parameterisation for four ranges of zenith angle. Using all available points at the same time to perform the fit, allows to obtain an estimation of the proper curve corresponding to each range of r , even if the statistics in that range is low.

An overall average fractional difference between each individual estimate of $\sigma_{t_{1/2}}$ and the parameterised value, $\sigma_{t_{1/2}}^p$, for all zenith angles and distance bins is shown in Fig. 4.7(a). The distribution is centered on 0. Figure 4.7(b) shows a comparison of $\sigma_{t_{1/2}}$ and the expected value $\sigma_{t_{1/2}}^p$. The points are in good agreement within the spread.

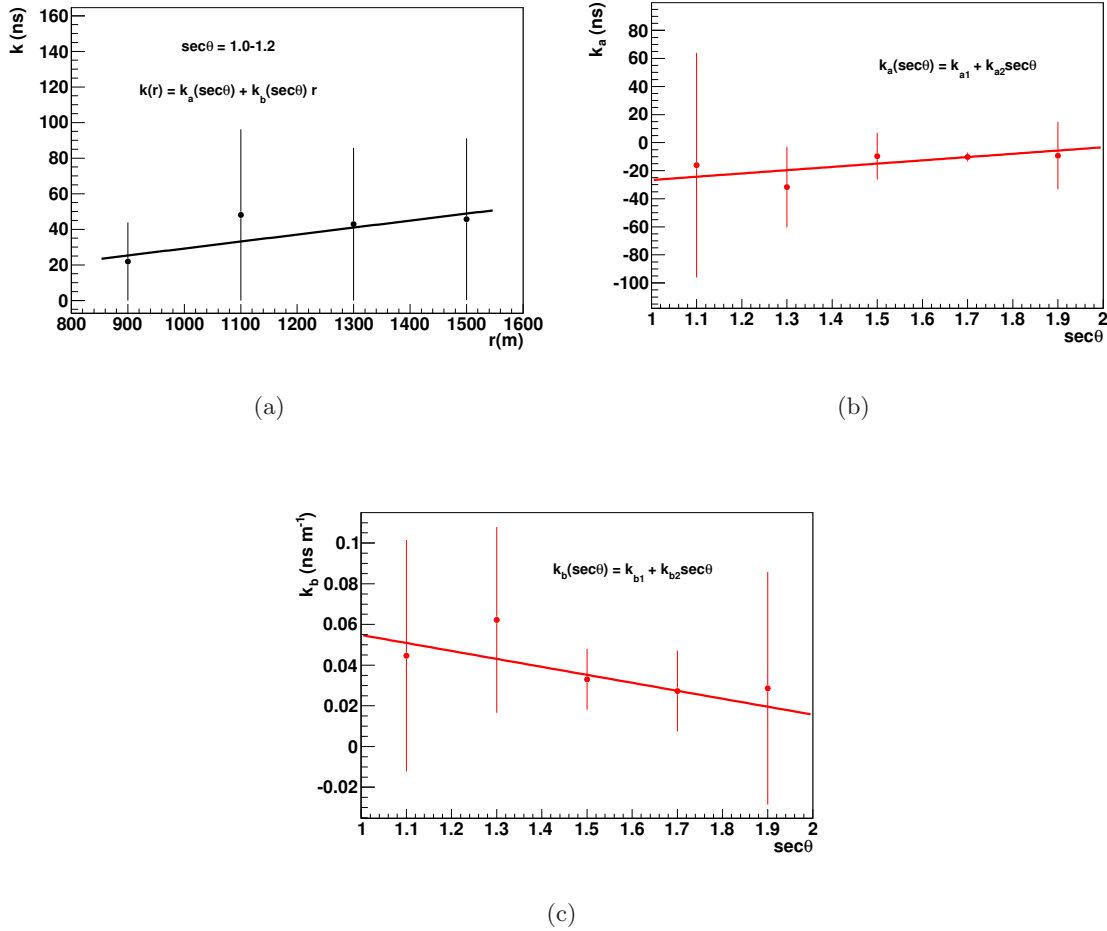


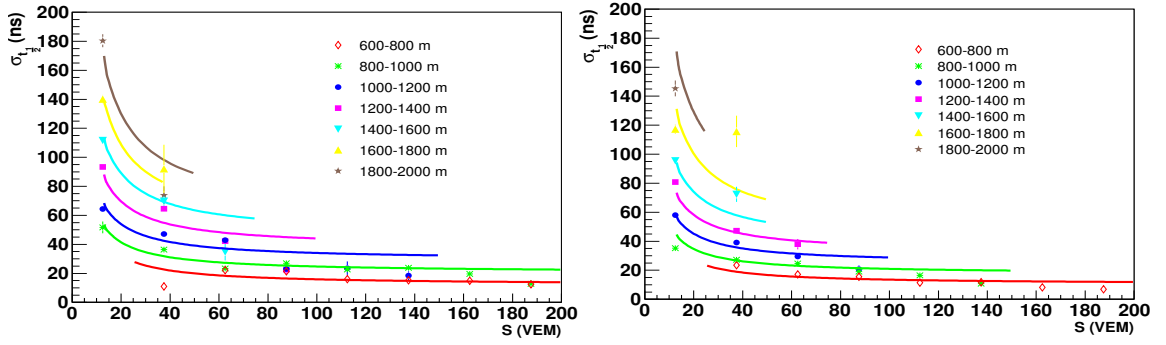
Figure 4.5: k parameter as a function of: (a) distance to the core, and (b)-(c) zenith angle, with linear fits.

The average fractional differences (see Fig. 4.8) are found to be 7% as a function of S , 7% as a function of r , 2% as a function of E and 20% as a function of $\sec\theta$. No systematic bias with S , r and E is observed. Nevertheless, a systematic bias with $\sec\theta$ is observed. This is most likely due to uncertainties introduced by the asymmetry correction and to the lack of statistics. For vertical showers this is due to the removal of saturated stations while for the inclined ones the number of stations fulfilling the cuts is small. An improvement of the statistics reduces the bias as it can be observed in Appendix A, Fig. A.3(d).

4.1 Uncertainty of risetime $\sigma_{t_{1/2}}$

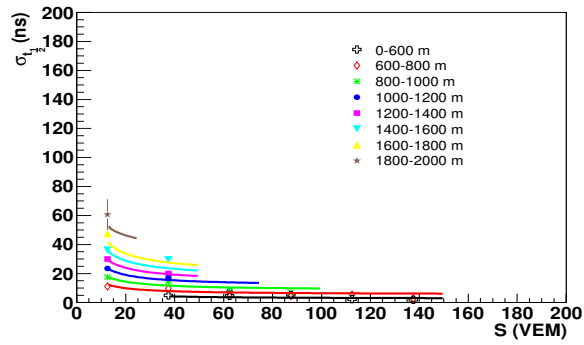
Parameter	Value	Error
j_{a1}	969.1	8.9
j_{a2}	-492	4.8
j_{b1}	-8.7×10^{-4}	8.5×10^{-6}
j_{b2}	5.3×10^{-4}	5.12×10^{-6}
j_{c1}	8.2×10^{-7}	5.9×10^{-9}
j_{c2}	-4.4×10^{-7}	3.6×10^{-9}
k_{a1}	-36.1	0.35
k_{a2}	16.5	0.19
k_{b1}	0.08	4.1×10^{-4}
k_{b2}	-0.03	2.6×10^{-4}

Table 4.1: Parameters for $\sigma_{t_{1/2}}$ with $\chi^2/ndf = 8.08$.



(a) $\sec \theta = 1.0 - 1.2$

(b) $\sec \theta = 1.2 - 1.4$



(c) $\sec \theta = 1.8 - 2.0$

Figure 4.6: Estimation of $\sigma_{t_{1/2}}(S)$ for three ranges of $\sec \theta$, taking into account the existing dependencies on r and $\sec \theta$ in the fit.

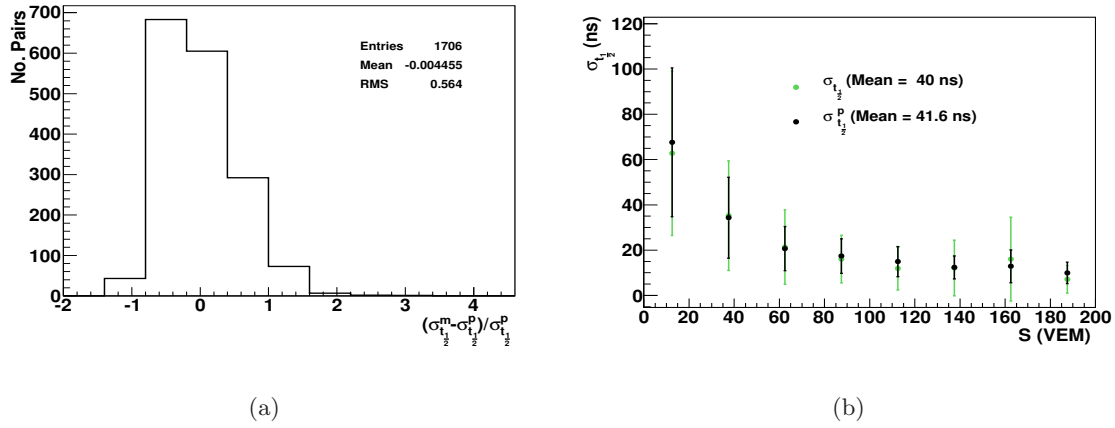


Figure 4.7: (a) The average fractional difference in $\sigma_{t_{1/2}}$ for all signals, distances, energies and $\sec\theta$. (b) Comparison between measured and expected value of $\sigma_{t_{1/2}}$, the error bars correspond to the spread.

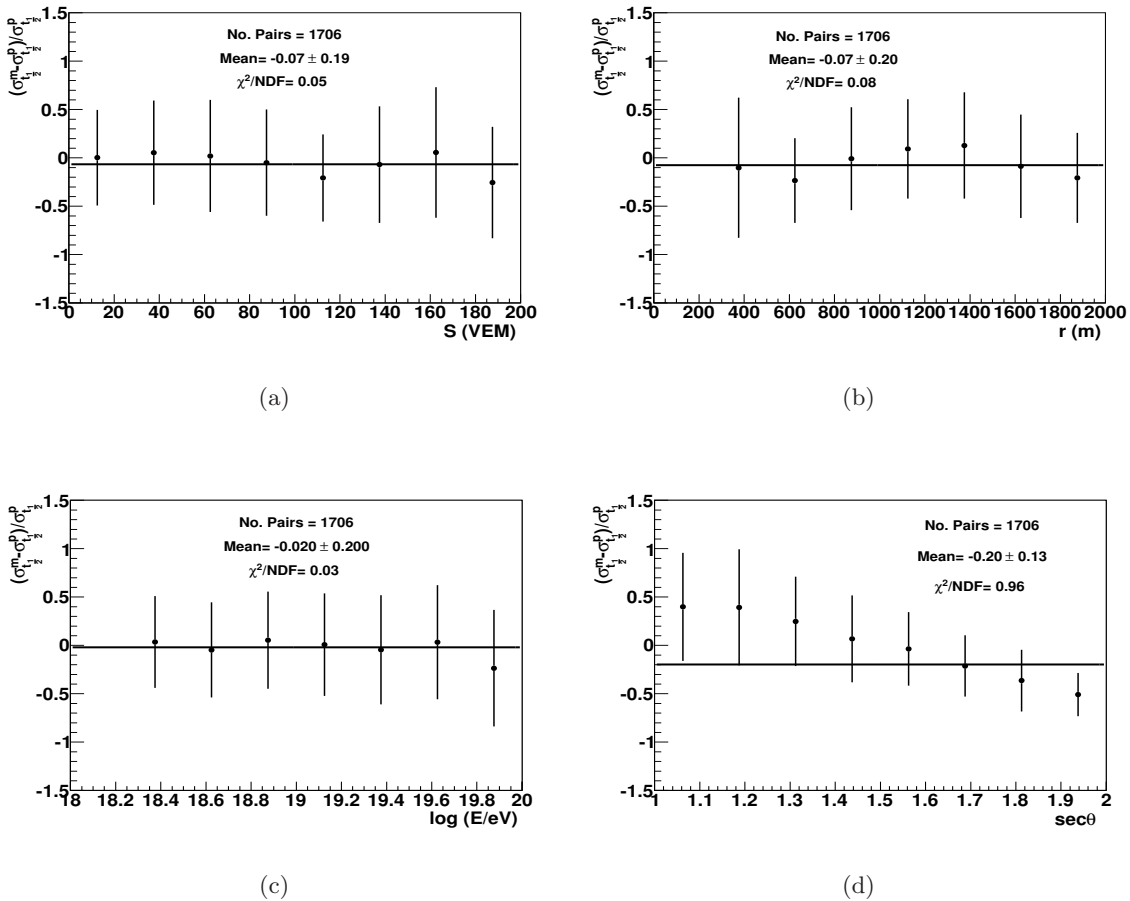


Figure 4.8: The average fractional difference in $\sigma_{t_{1/2}}$ as a function of : (a) signal, (b) distance to the core, (c) energy of the shower and (d) $\sec\theta$. The horizontal lines correspond to the fit of a constant function over the points, showing the mean values of the average fractional difference.

Comparison with Monte Carlo simulations The results of the method are confirmed using Monte Carlo simulations containing a ring of stations located at 1000 m from the shower core. The pairs correspond to the stations located at $\zeta = \pm 90^\circ$, angle where no azimuthal asymmetry correction is necessary (see next section). Stations have to fulfill also the conditions imposed for measurements. The simulations are performed with CORSIKA [194, 195] (QGSJET II model) and Offline (Geant4Fast [196, 197]), having as primary particles proton (801 showers) and iron (1223 showers), generated with isotropic arrival directions within a zenith angle range from 0 to 65° and an energy distribution following a power law with a spectral index of -3 below 3 EeV and -2.5 above this energy. Figure 4.9 shows the comparison of the expected $\sigma_{t_{1/2}}$ for three ranges of zenith angle, with the value obtained from measurements (about 7000 showers). The agreement between simulations and measurements is good, validating the method within the very limited statistics. This also validates the use of the $\sigma_{t_{1/2}}$ obtained from measurements, by Monte Carlo simulations, as is going to be used later in this thesis. It is interesting to see that the agreement for the first bin of signal improves with the zenith angle. This suggests that the minimum requested signal may be greater than 10 VEM for vertical showers, to be able to compare with simulations.

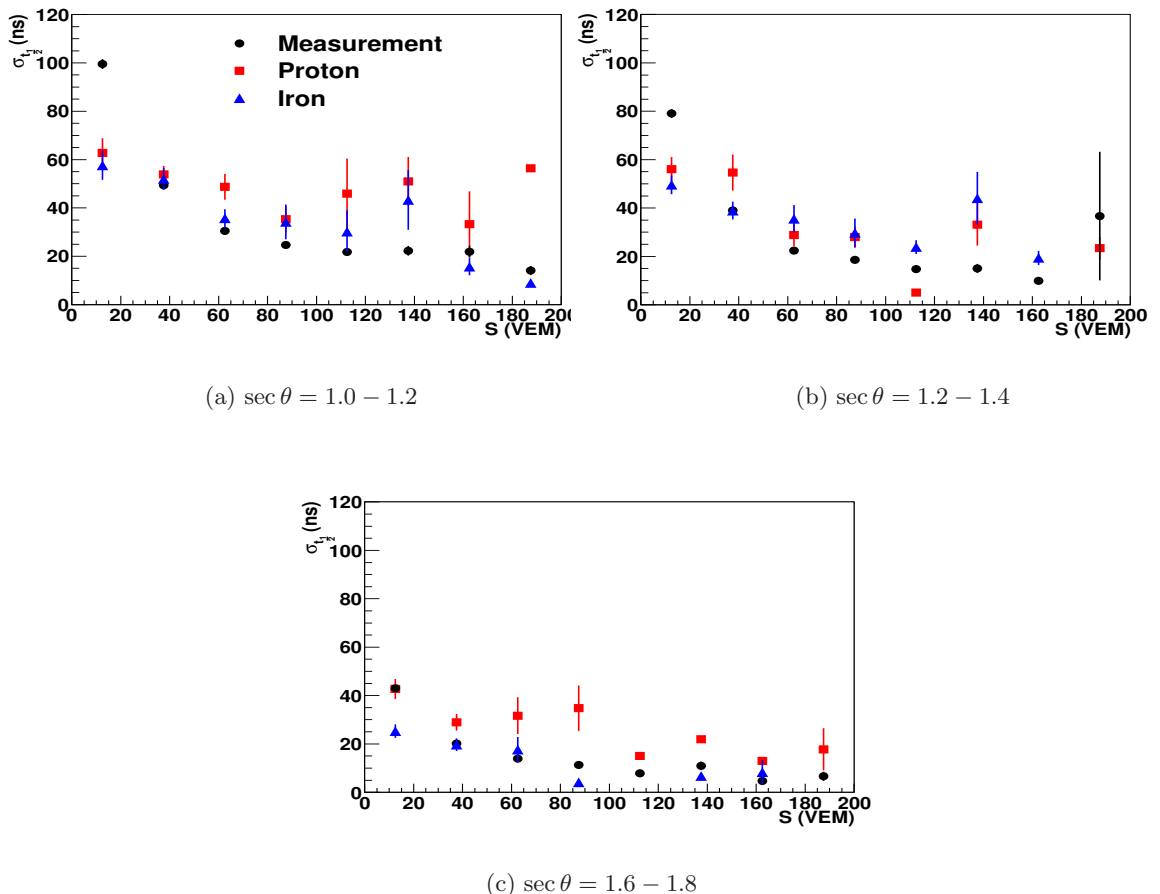


Figure 4.9: Comparison of $\sigma_{t_{1/2}}$ with Monte Carlo simulations. Values are of the same order and are in good agreement for almost all signals.

4.2 Asymmetry correction

As mentioned in Chapter 3, the distribution of shower particles arriving at ground presents an azimuthal asymmetry which is observed in the risetime. Figures 4.10(a) and 4.10(b) show the asymmetry of the risetime according to the azimuthal angle, ζ , as registered by the SD. The azimuthal asymmetry is due to the following factors: the difference in the muon to electromagnetic ratio during the longitudinal evolution of the shower produces an asymmetry in particle densities and arrival times. Therefore, the risetime measured in the early part of the shower (upstream) is larger than in the late part (downstream). Electrons which travel long distances through the air before arriving at the ground, which is the case of the late part of the shower, can be attenuated producing an almost pure muonic signal on the detectors. Whereas particles arriving from the early part of the shower were not attenuated (see Fig. 4.11). Geometrical effects related to the incidence angles of the particles on the walls of the tanks are other factors which contribute to the asymmetry [198].

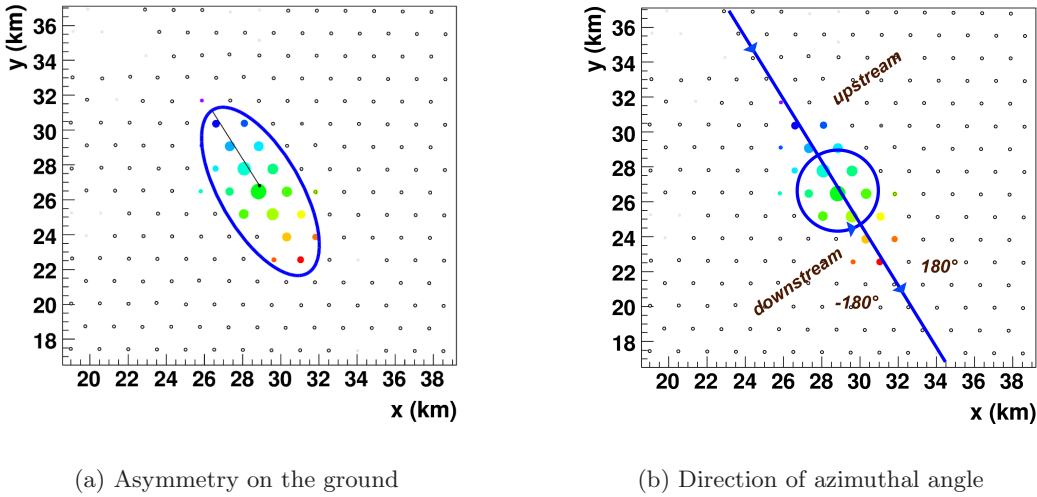


Figure 4.10: Footprint of a shower. (a) Showing its asymmetry according to the arrival direction, colors show different $t_{1/2}$ for early particles (cold color) and late particles (hot color). (b) The arrow on the circle shows the direction of the azimuthal angle.

The asymmetry has to be corrected to allow the proper use of $t_{1/2}$ for further analysis, avoiding the effects introduced by the characteristics of the detector. It is equivalent to translate the plane of the detector to be parallel to that of the shower front. The same set of data used for studies on the measurement uncertainty of risetime is used in this analysis. The parameterisation of $\sigma_{t_{1/2}}(S)$ obtained in the last section is taken into account. In order to observe and characterize the asymmetry for later correction, it is necessary to split the data in ranges of r (8 bins) and θ (5 bins). Figure 4.12 shows the asymmetry for some of the ranges of distance from the shower core and zenith angle. The asymmetry is large for $\zeta = 0^\circ$, where $t_{1/2}$ corresponds to the early part of the shower, as it is expected. It is observed that the asymmetry decreases with the zenith angle, showing the effect of the attenuation of particles in the signal. As discussed in the last section, the risetime and in consequence the asymmetry, is larger for stations located far from the shower core, which can be also observed.

The parametrization of the asymmetry is made with the following function:

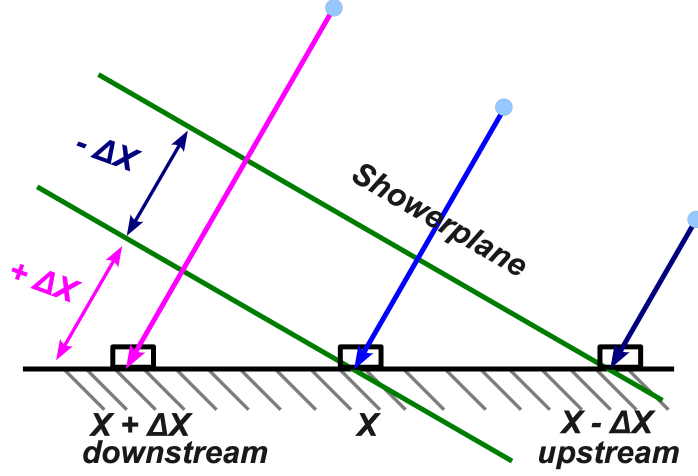


Figure 4.11: Diagram of the arrival of particles. Particles in the downstream part travel longer distances (pink line) than those in the upstream part (dark blue line).

$$t_{1/2}(r, \theta, \zeta) = f + g \cdot \cos(\zeta), \quad (4.10)$$

this expression has to be subtracted from the measured value of risetime, $m(r, \theta, \zeta)$

$$m(r, \theta, \zeta) - (f + g \cdot \cos(\zeta)) = 0, \quad (4.11)$$

resulting in the following expression for the corrected risetime, f

$$f = m(r, \theta, \zeta) - g \cdot \cos(\zeta), \quad (4.12)$$

where the parameter g is the correction factor. The correction factor has to be parameterised taking into account the dependence on r and θ . Figure 4.12(d) shows the dependence on r , which is parameterised with a quadratic polynomial

$$g(r, \sec \theta) = \epsilon(\sec \theta) + \delta(\sec \theta) \cdot r^2. \quad (4.13)$$

The dependence on θ of the parameters is then described with a Landau function, it is shown in Figs. 4.13. The obtained parameters are shown in table 4.2.

After applying the correction to the data set, a suppression of the asymmetry is observed in Figs. 4.14. The effectiveness of the parameterisation can be observed taking the extreme value of $t_{1/2}$ at 0° of azimuthal angle, and comparing it with the expected value of $t_{1/2}$ at 90° , where the correction does not apply (see equation 4.12). It is found that the correction works properly, the bias is between 1% and $< 5\%$ for distances in the range of [600 m, 1800 m], and $\sim 12\%$ for extreme distances, as shown in Fig. 4.14(d).

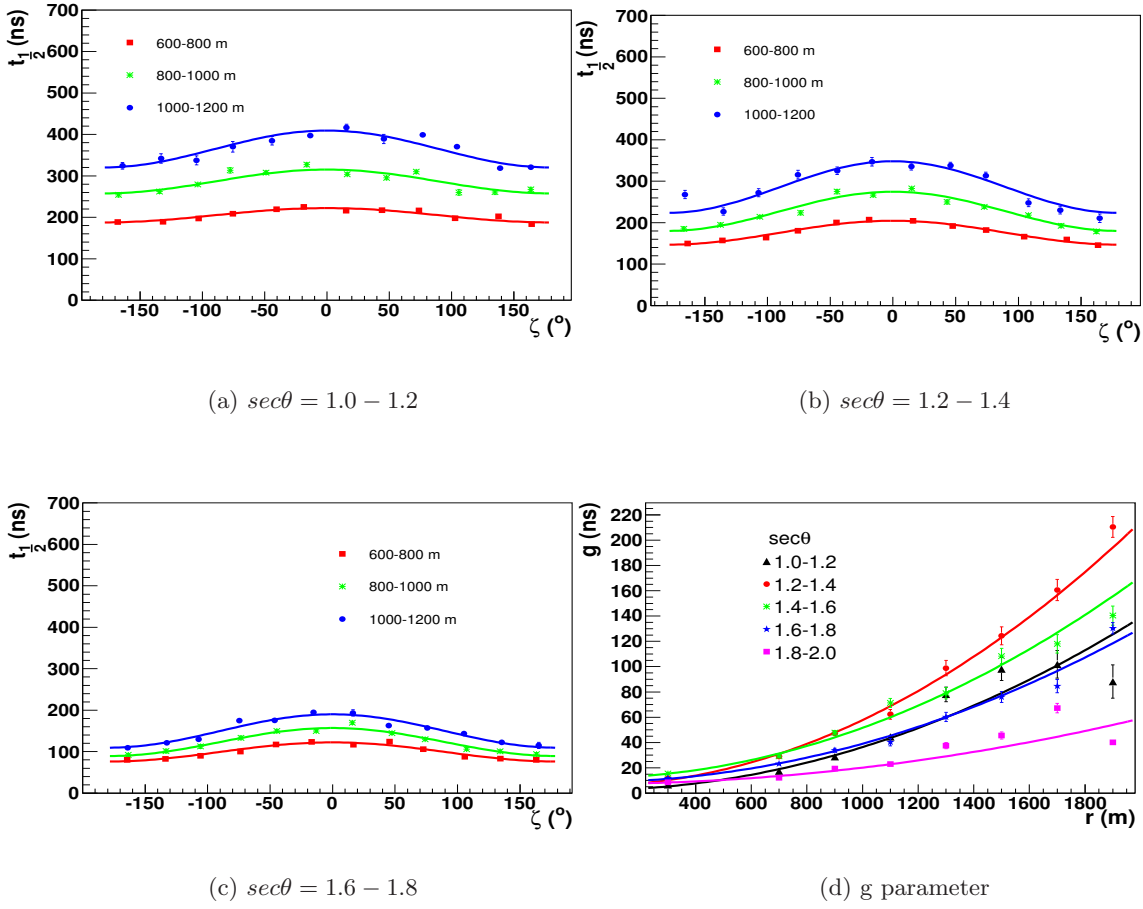


Figure 4.12: (a)-(c) Asymmetry observed in the risetime for different ranges of r and θ . (d) Correction factor g as a function of the distance from the shower core.

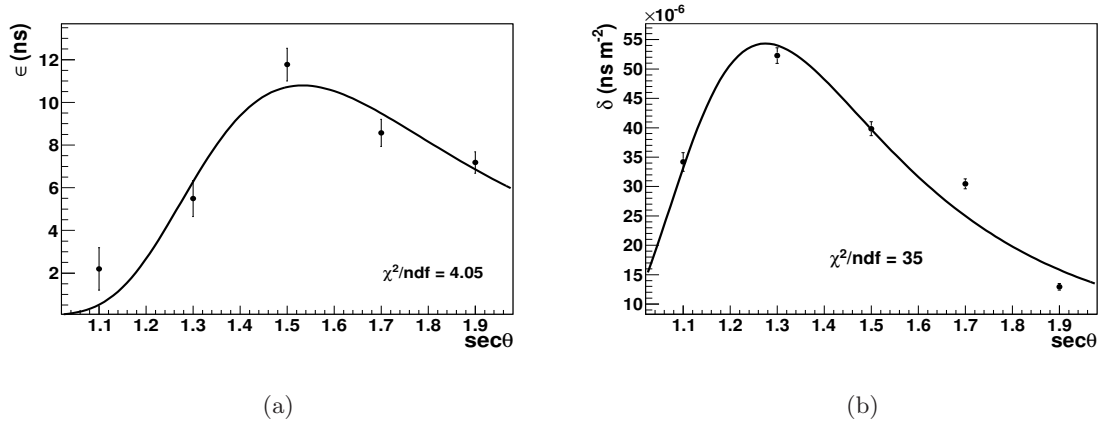


Figure 4.13: Parameters ϵ (a) and δ (b), of the correction factor, as a function of $\sec\theta$.

Parameter	Value	Error
ϵ_{mpv}	1.6	0.024
ϵ_{σ}	0.19	0.027
ϵ_C	59.75	4.2
δ_{mpv}	1.3	5.7×10^{-3}
δ_{σ}	0.15	3.7×10^{-3}
δ_C	3.0×10^{-4}	6.7×10^{-6}

Table 4.2: Values for ϵ and δ parameters as a function of $\sec\theta$. For the Landau function, *mpv* means the most probable value, σ is a scale parameter and C is a constant.

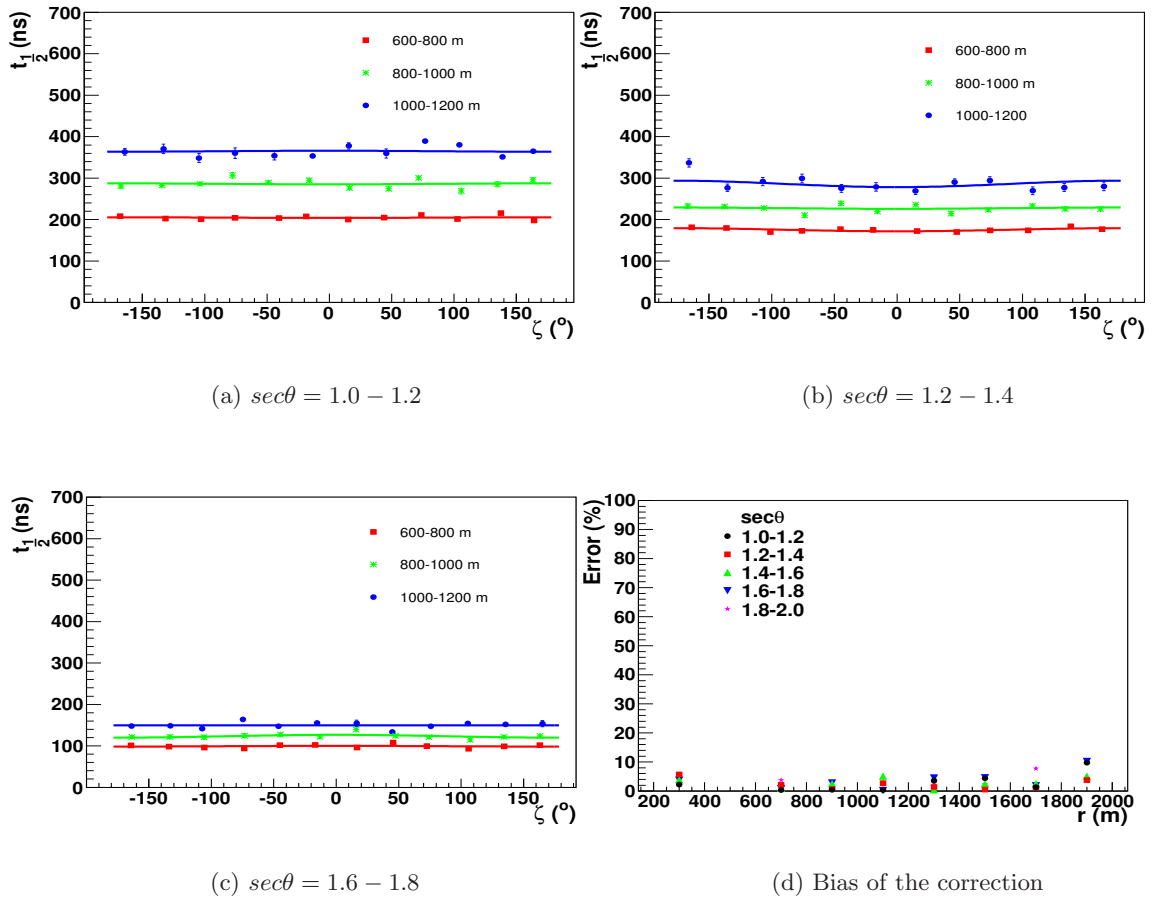


Figure 4.14: (a)-(c) Risetime corrected for the azimuthal asymmetry for different ranges of r and θ . (d) Bias of the parameterised azimuthal asymmetry correction with respect to the expected value as a function of the distance from the shower core.

4.3 Parameterisation of risetime

Until now, the parameterisation of $t_{1/2}$ was made based on its dependence on the distance from the shower core with a function of the form

$$t_{1/2}(r) = 40 + a \cdot r + b \cdot r^2 \quad [ns], \quad (4.14)$$

where 40 ns was fixed based on studies with inclined showers [182, 199]. It is an artificial lower limit for the risetime introduced to the time trace by the limitation of the bin width of recorded FADC traces, which is 25 ns, and by the effect of the detector response, which is convoluted with the arrival times of particles. This effect is called the Single Particle Response (SPR) [189] and results in a lengthened time trace for each particle being detected.

Nevertheless, there are dependencies of risetime on zenith angle and energy, which must be taken into account for the main studies presented in this thesis, being based on the parameterisation of $t_{1/2}$. The same sample of events used for the last two sections is analyzed.

The dependence of risetime on θ is shown in Fig. 4.15 and is described with the function

$$t_{1/2}(r, \theta) = 40 + \alpha(\theta) \cdot r + \beta(\theta) \cdot r^2 \quad [ns]. \quad (4.15)$$

The parameters are described by a Gaussian function (parameter α)

$$\alpha = a_1 \cdot e^{-\lambda}, \quad (4.16)$$

where λ is

$$\lambda = \frac{1}{2} \left(\frac{\sec \theta - a_2}{a_3} \right)^2, \quad (4.17)$$

and a quadratic polynomial (parameter β)

$$\beta = b_1 + b_2 \cdot \sec \theta + b_3 \cdot \sec^2 \theta. \quad (4.18)$$

These dependencies are shown in Fig. 4.16.

The dependence of risetime on the energy E is shown in Fig. 4.17 and is described with the function

$$t_{1/2}(r, E) = 40 + A(E) \cdot r + B(E) \cdot r^2 \quad [ns]. \quad (4.19)$$

The parameteres are described with linear functions (see Fig. 4.18)

$$A(E) = \varepsilon_{a1} + \varepsilon_{a2} \cdot \log E \quad (4.20)$$

and

$$B(E) = \varepsilon_{b1} + \varepsilon_{b2} \cdot \log E, \quad (4.21)$$

where log refers to the decadic logarithm, \log_{10} .

The final function to fit, which is dependent of zenith angle, energy and distance from the shower core, has the following form

$$t_{1/2}(r, \theta, E) = 40 + A(E) \cdot \alpha(\theta) \cdot r + B(E) \cdot \beta(\theta) \cdot r^2 \quad [ns]. \quad (4.22)$$

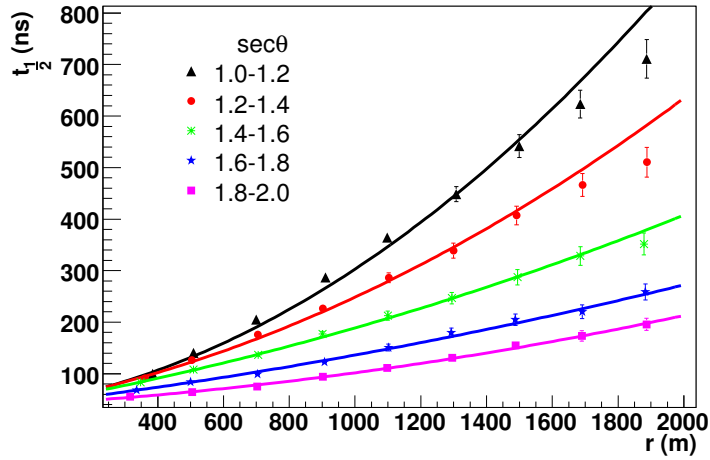


Figure 4.15: Risettime as a function of distance from the shower core for five intervals in zenith angle.

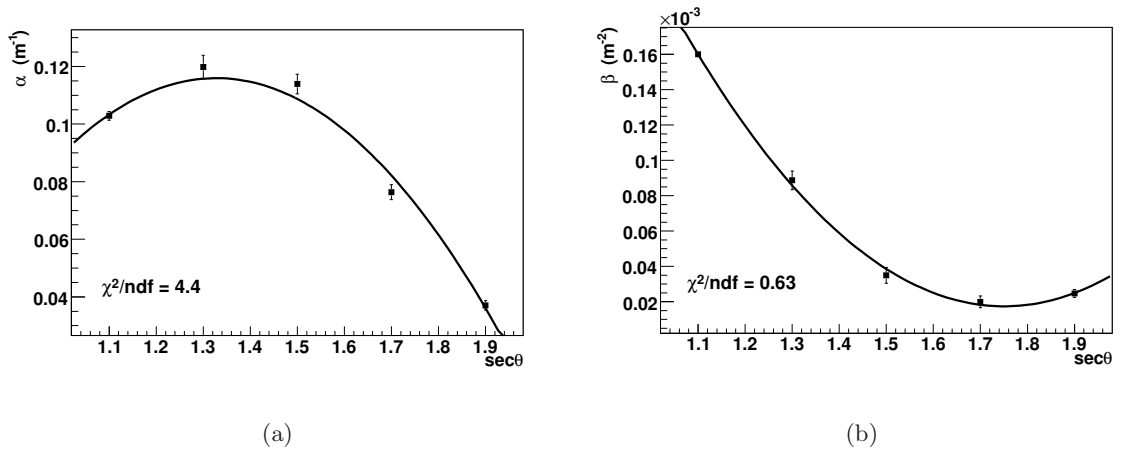


Figure 4.16: (a) Parameter α as a function of zenith angle, (b) Parameter β as a function of zenith angle.

With the purpose of obtaining parameters which describe the behavior of a fit according to a typical event, a simultaneous fit is performed. This fit takes into account all valid points of all events, such that the parameters are reasonable initial values when performing individual fits, even if a standard event-by-event fit can not be performed. However, to fix all parameters would not allow us to perform a fit of each specific event. For this reason, the parameter ε_{a1} (which is the most significant parameter in the function) is considered as a free parameter which is going to describe each individual event. In order to find the optimum distance from the shower core for which the fit works within the uncertainty, the stations belonging to the events considered are investigated. It turns out that most of the stations are located within the range $\sim [600 \text{ m}, 1500 \text{ m}]$ as shown in Fig. 4.19.

Events containing at least one station in this range are analyzed. The residuals of the fit, indicate that the fit is well within a $\pm 1\sigma$ band in the range of $[600 \text{ m}, 1200 \text{ m}]$. Figure 4.20

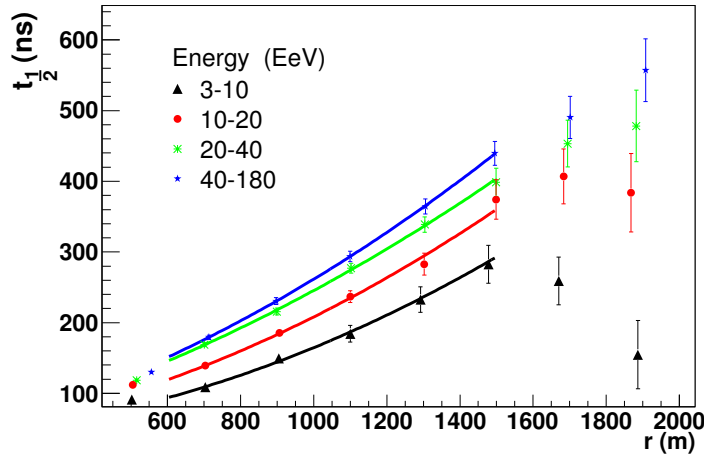


Figure 4.17: Risetime as a function of distance from the shower core for five intervals in energy.

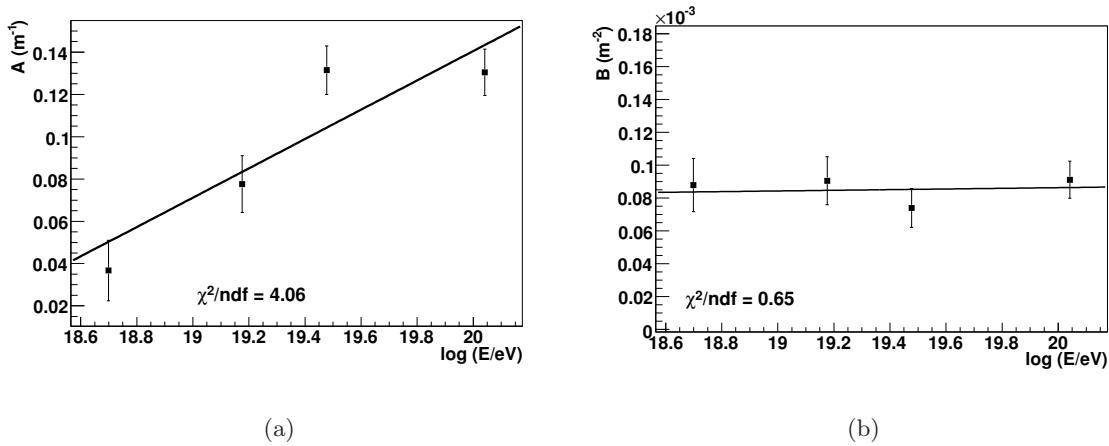
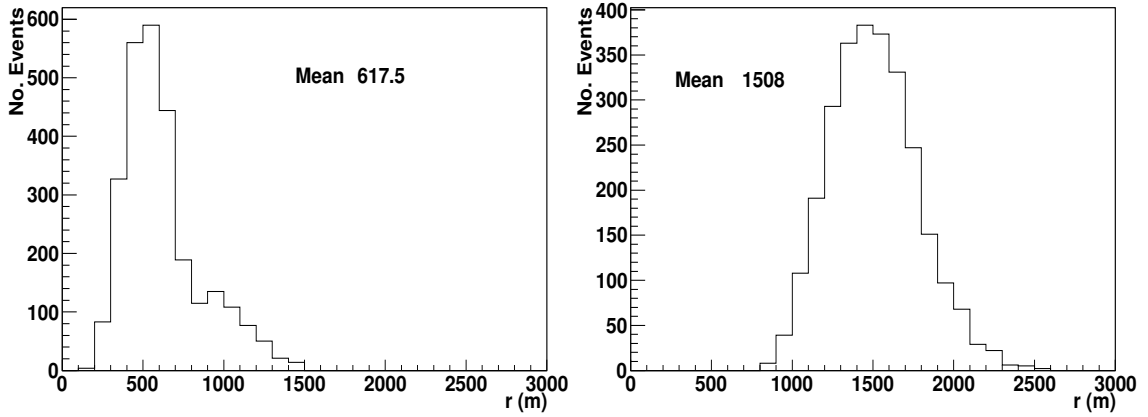


Figure 4.18: (a) Parameter A as a function of energy, (b) Parameter B as a function of energy. Notation \log refers to the decadic logarithm, \log_{10} .

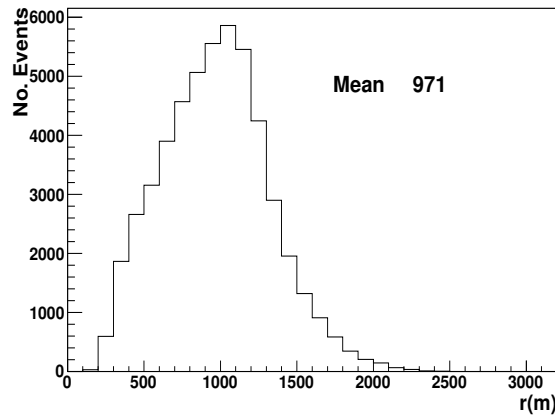
shows two of the five ranges of zenith angles, for the rest, the residuals are also within $\pm 1\sigma$ in the same range of r .

A comparison of different kinds of fits for a single extreme event is shown in Fig. 4.21. The event has only two candidate stations in the considered range of distances, which results in zero degrees of freedom left for the standard fit (Eq. 4.14). The situation is different for the fit proposed in this section (*One free parameter* in the figure) since there is still one degree of freedom left. In this case, the event seems to be described in a more realistic way being possible that the fit almost matches the remaining candidate station, which is located below 400 m.



(a) Core distance of the closest station within an event

(b) Core distance of the farthest station within an event



(c) Core distance distribution of all stations

Figure 4.19: Distance from the shower core of stations belonging to the sample of events used for the analysis. The second bump in (a) is due to the removal of saturated stations, which are typically at the early part of the shower, leaving as the first available stations those located farther.

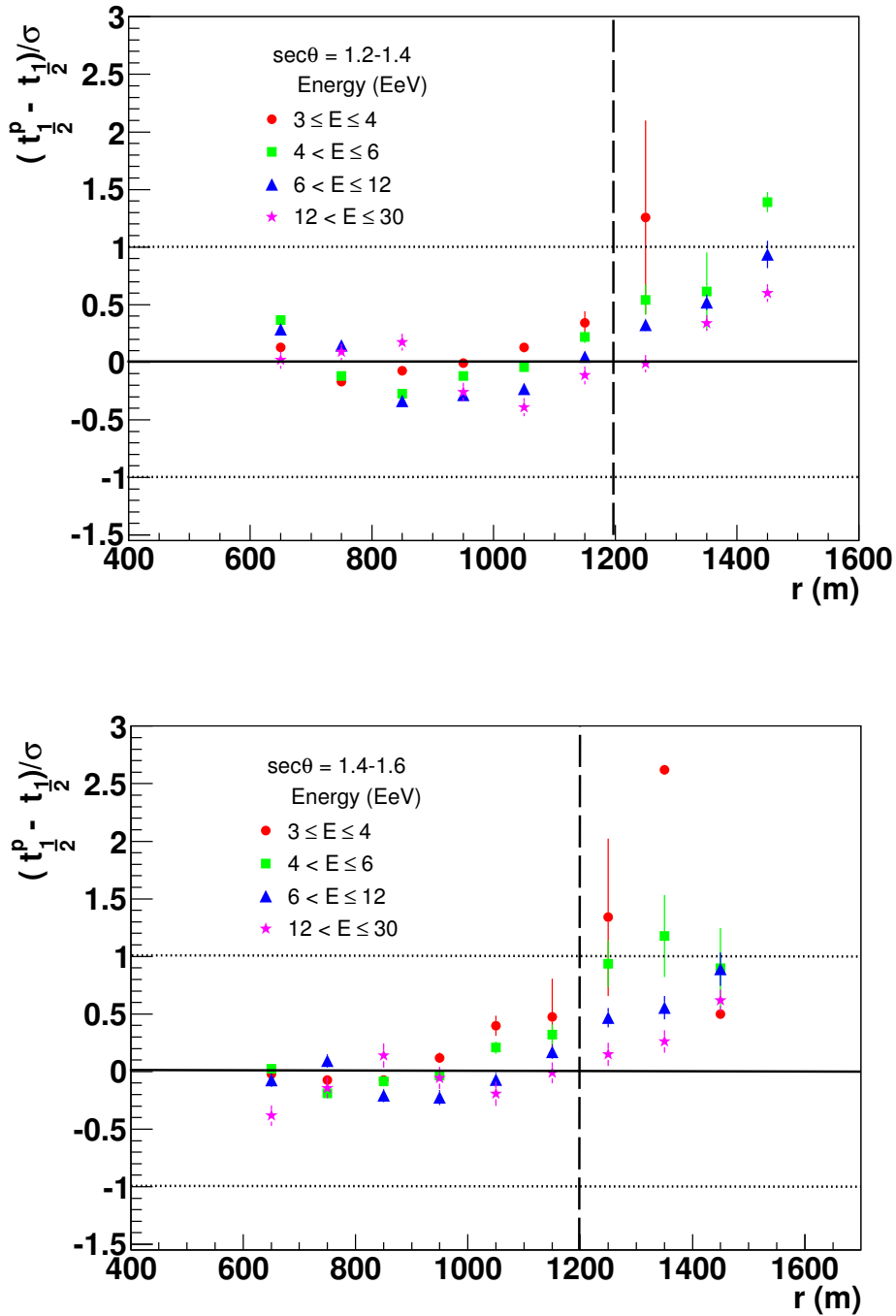


Figure 4.20: Residuals of the proposed fit ($t_{1/2}^p$) for two out of five intervals of zenith angle. The vertical line shows the distance where residuals are no more within $\pm 1\sigma$, this limit is delimited by the horizontal lines.

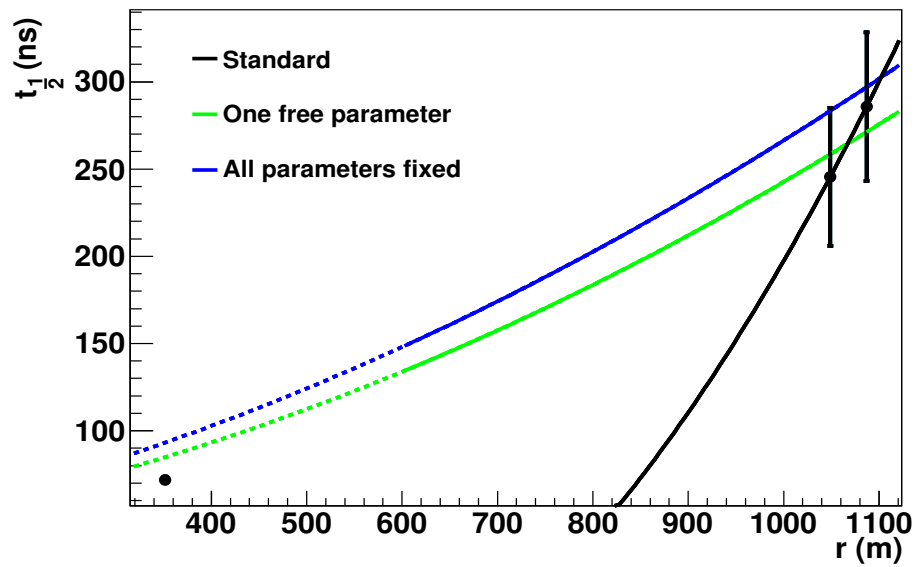


Figure 4.21: Example of an event which can be described in a proper way using the proposed fit (“One free parameter”). “All parameters fixed” corresponds to the fit obtained directly from the simultaneous fit and “Standard” corresponds to Eq. 4.14. The dotted lines show the values of the functions out of the fitting range, close to match the remaining station.

4.4 $t_{1/2}(1000\text{ m})$ as a mass composition parameter

As mentioned in Chapter 3, $t_{1/2}(1000\text{ m})$ has been used as a mass-sensitive observable using the function 4.14. In this section, a cross-check of the results obtained in Ref. [183], using the function proposed in the last section (Eq. 4.22 with ε_{a1} free) and taking into account the measurement uncertainty, $\sigma_{t_{1/2}}$, is done. The events considered for this study are having an energy above 3 EeV, zenith angles below 60° , T4 trigger condition fulfilled, they may not be lightning, and having at least one station in the range [600 m, 1200 m] of distance from the shower core is necessary. The stations must have a signal above 15 VEM, and not be saturated. The selection of 1000 m obeys the need to use a unique representative value of the shower, instead of several values corresponding to each station. This simplifies the analysis and reduces the introduced fluctuations. Furthermore, most showers present signal around that distance from the shower core as shown in Fig. 4.19(c). This corresponds also to the distance at which the fluctuations of the particle density are the smallest (see Chapter 2). The value of $t_{1/2}(1000\text{ m})$ is obtained by interpolation. The same procedure is made for Monte Carlo simulations, which are used to compare with measurements. Comparisons may allow to obtain an estimation of the mass composition.

Comparison with Monte Carlo simulations The same set of simulations already used for $\sigma_{t_{1/2}}$ studies is taken into account. In principle, the risetime at 1000 m from the shower core seems to be useful for discriminating between different primary particles as shown in Fig. 4.22. The comparison of measurements with the values obtained from Monte Carlo simulations shows that risetimes of iron primaries are smaller than the ones corresponding to proton as expected, even though the estimation for composition of measurements is not clear. However, in figure 4.23(a), the values of $t_{1/2}(1000\text{ m})$ as a function of zenith angle reveal more details about the validity of the comparison. Monte Carlo data are not in the range given by measurements, suggesting a heavy mass composition for all ranges of $\sec\theta$. This may not be the case according to predictions and results using other mass-composition sensitive observables as X_{\max} (see Chapter 3). This contradiction is explained since it was recently found that QGSJET II model predicts less muons than recorded in SD tanks [200, 201]. Using the factors reported in Ref. [200] the muonic component of the time trace is corrected and a new FADC trace is built, from which the risetime is recalculated. A farther comparison is obtained in Fig. 4.23(b). Measurements are now within the limits given by predictions. Nevertheless, this correction can not be used because it does not only depend on the predictions of the hadronic interaction model, but also on the reliability of the model used for calculating the electromagnetic interactions. There is also an effect observed at $\sec\theta > 1.5$ for Monte Carlo and at $\sec\theta > 1.7$ for measurements, which indicates that for inclined showers the value of the risetime is limited by the minimum value of 40 ns imposed in the fit and the corresponding faster traces are not described properly. This introduces a strong bias with respect to the zenith angle. A comparison of $t_{1/2}(1000\text{ m})$ as a function of the energy may give information about the evolution of the mass composition according to the observed dependence on the energy. Figure 4.24 shows the corresponding plot using the set of Monte Carlo data described in Section 6.2, for three ranges of zenith angle. Unfortunately, no clear dependence on the energy is observed. This result might indicate that fluctuations on the fit are still significant, as observed in the corresponding $\text{RMS}(t_{1/2}(1000\text{ m}))$ plots. Simulations and measurements have the same order, however, a dependence of $t_{1/2}(1000\text{ m})$

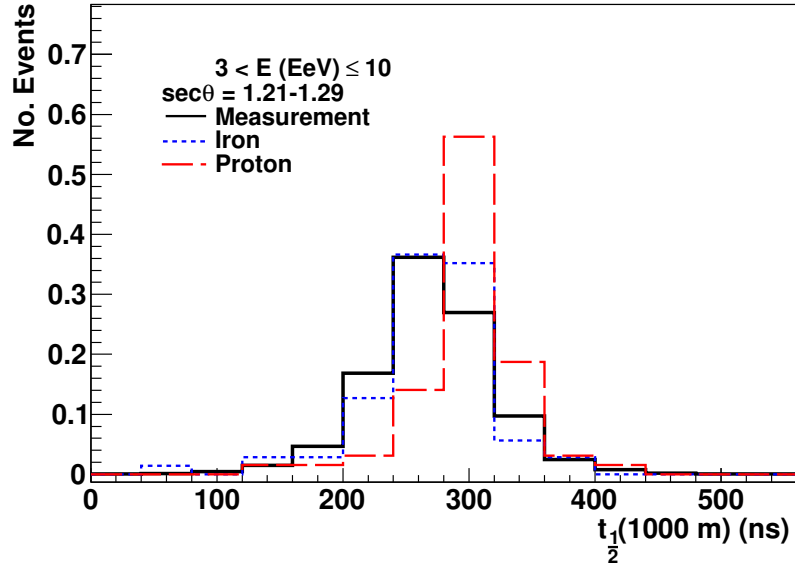


Figure 4.22: Comparison of $t_{1/2}(1000 \text{ m})$ of measurements with Monte Carlo simulations. The histograms are normalized to unity.

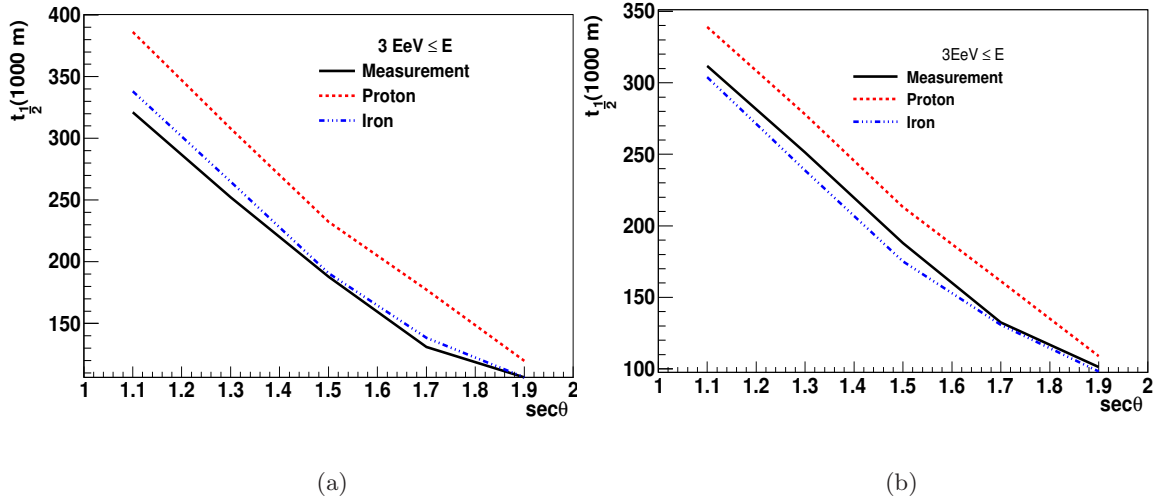


Figure 4.23: Comparison of $t_{1/2}(1000 \text{ m})$ as a function of the zenith angle using a parameterisation as the one proposed in this chapter. (a) Showing the result using Monte Carlo simulations. (b) Showing the result using corrected Monte Carlo simulations.

with zenith angle is observed. Nevertheless, qualitatively a mass composition getting heavier with energy is observed. Results shown in Fig. 3.7 are confirmed as shown in Fig. 4.25, and it can be concluded that $t_{1/2}(1000 \text{ m})$ is not a suitable mass composition observable, when Monte Carlo data are used as a reference.

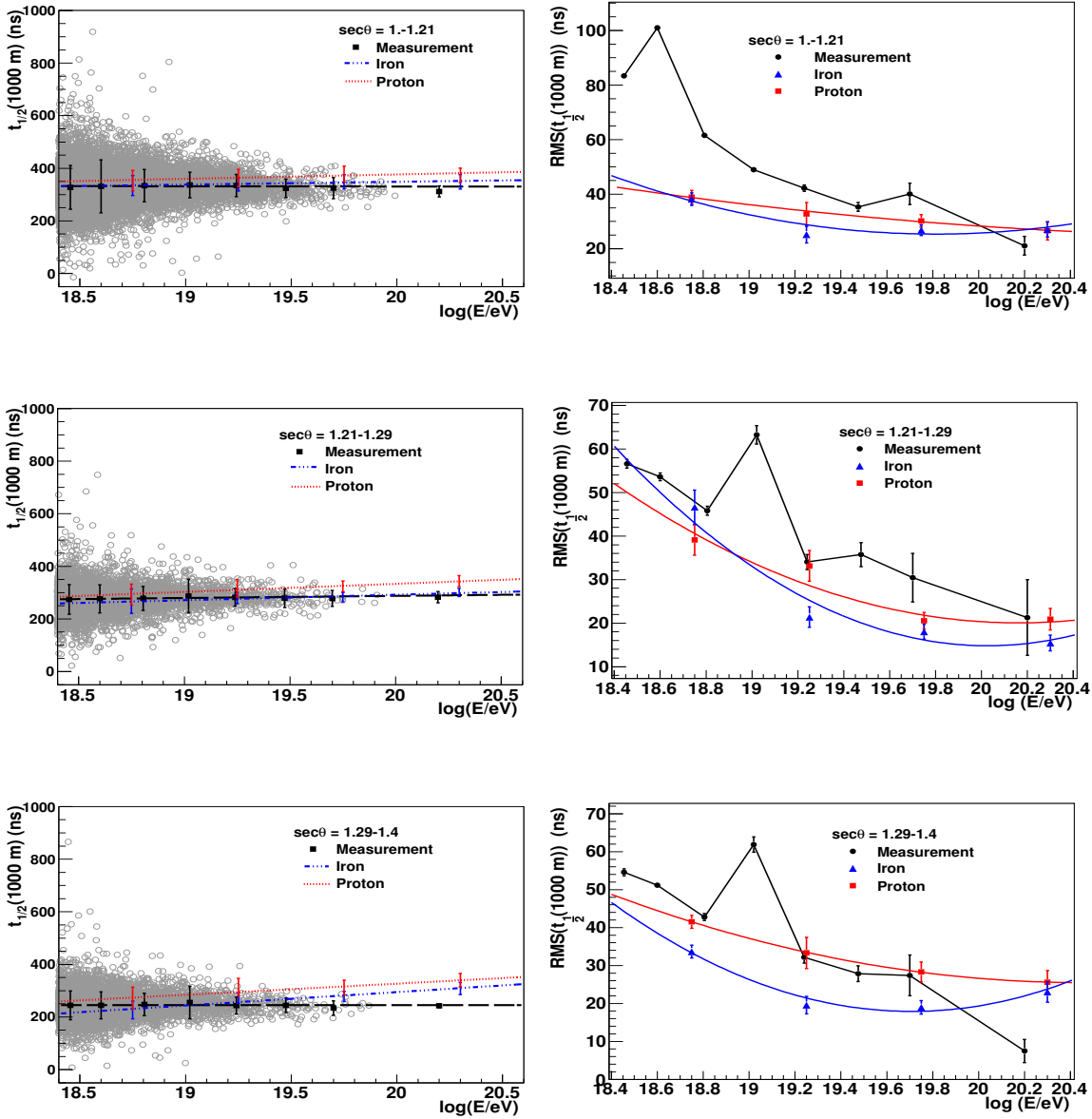


Figure 4.24: Left: comparison of $t_{1/2}(1000 \text{ m})$ as a function of the energy of measurements with Monte Carlo simulations (QGSJET II model) for three ranges of zenith angles. The dashed line is a linear fit to the measured data, shown also as gray circles, the error bars correspond to the spread of the data. Right: the corresponding fluctuations of $t_{1/2}(1000 \text{ m})$. Values are zenith angle dependent.

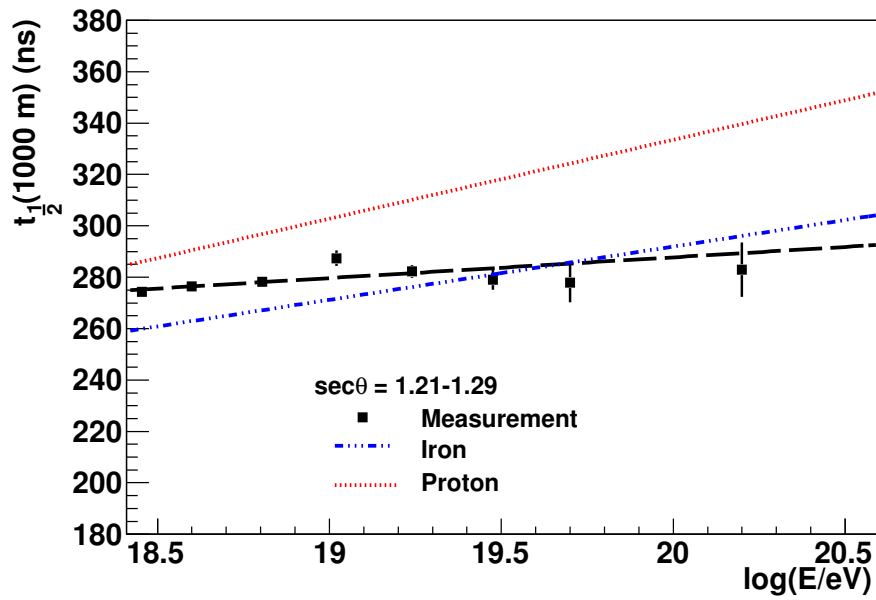


Figure 4.25: Comparison of $t_{1/2}(1000 \text{ m})$ as a function of the energy of measurements with Monte Carlo simulations (QGSJET II model). The dashed line is a linear fit to the measured data, showing almost no change with the energy. The error bars correspond to the error of the mean value.

Chapter 5

Δ_{1000} as a mass composition sensitive parameter

The Pierre Auger Observatory offers the possibility to study the risetime in several manners due to the huge amount of data available. To take advantage of this situation, the use of observables based on risetime becomes crucial. One of the first parameters used for studying mass composition with the SD is $t_{\frac{1}{2}}(1000\text{ m})$. Nevertheless, as confirmed in Chapter 4, this is not a suitable observable, leading to the necessity of finding more parameters based on risetime. In this chapter a new parameter, Δ_{1000} , is proposed. The correlation of this new observable with X_{max} is explored to obtain an estimation of a depth of the shower maximum based on SD measurements, namely $X_{\text{max}}^{\text{SD}}$. Results on evolution of this parameter with energy as well as systematics errors are also shown.

5.1 Definition

The Δ_{1000} parameter is defined as the difference of the $t_{\frac{1}{2}}(1000\text{ m})$ value in an event, to the average risetime at 1000 m from the shower core as obtained from fits to the risetime as a function of core distance for all events belonging to each one of five energy ranges. This difference is normalized to the measurement uncertainty, $\sigma_{t_{\frac{1}{2}}}(S, r, \theta)$ calculated in Chapter 4, with $S = S(1000\text{ m})$. Each fit in a specific energy range represents a so called *benchmark* and the corresponding value at 1000 m is called $t_{\frac{1}{2}}^{\text{BM}}(1000\text{ m})$. The proposed Δ_{1000} parameter is represented as

$$\Delta_{1000}(r, \theta, S, E) = \frac{t_{\frac{1}{2}}(1000\text{ m}) - t_{\frac{1}{2}}^{\text{BM}}(1000\text{ m})}{\sigma_{t_{\frac{1}{2}}}}. \quad (5.1)$$

A schematic representation of Δ_{1000} is shown in Fig. 5.1. The Δ_{1000} parameter as well as $t_{\frac{1}{2}}(1000)$, allows to obtain a single value per event. It is defined with the goal to avoid the fluctuations introduced by fitting $t_{\frac{1}{2}}(r)$ on an event-by-event basis regardless of the arrival direction and signal position. The use of benchmarks for several energy ranges to calculate the differences allows to avoid a bias with energy. Each benchmark provides $t_{\frac{1}{2}}(1000)$ for showers having similar depth of the shower maximum, because it is calculated for a specific

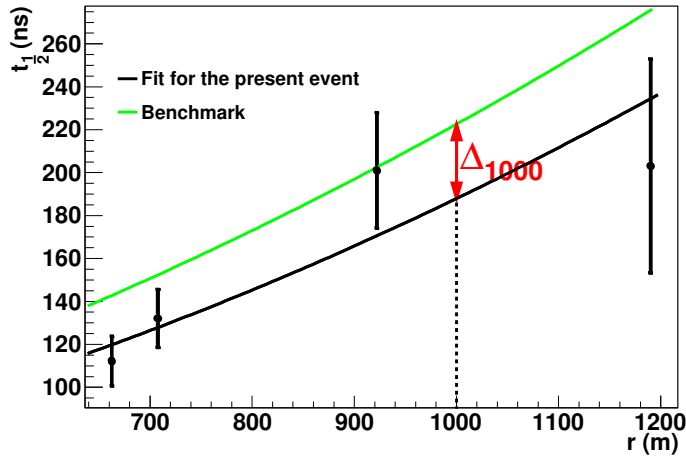


Figure 5.1: Schematic representation of Δ_{1000} parameter, the deviation is going to be expressed in units of measurement uncertainty.

energy range. Since the risetime increases with X_{\max} , as shown with Monte Carlo simulations in Ref. [202], the variation in risetimes is also related to changes in the atmospheric depths of observation (this assumption was proved by studying changing weather conditions [175]). Thus, the difference about the benchmark function, Δ_{1000} , is expected to present also a correlation with X_{\max} .

The Benchmark Function For obtaining Δ_{1000} it is necessary to perform a fit of the risetime as a function of distance from the shower core for every single event, and also an average fit for all events contained in each energy range, i.e. the benchmark function.

To get the benchmark, a function as the one proposed in equation 4.22 is used. This allows to obtain a value for Δ_{1000} from events having only one station located into the range of distances taken into account for the fit, which is [600 m, 1200 m]. The events considered for this analysis fulfill the same conditions as for the calculation of $t_{1/2}(1000)$, mentioned in Section 4.4, but changing the condition of T4 trigger to T5 trigger, to ensure a high qualitative reconstruction of the shower. Events from $\log(E/\text{eV}) = 18.4$ on, are taken into account since the SD detector is sensitive to all showers at these energies for $\theta < 60^\circ$ as shown in Fig. 5.2(a) [203]. Figure 5.2(b) shows the efficiency of the SD detector to T5 events passing the requested cuts for $\theta < 60^\circ$. The detection efficiency is $\sim 70\%$ at $10^{18.4}$ eV and reaches $\geq 95\%$ at 10^{19} eV. The benchmarks are obtained considering five ranges of energy, from $\log(E/\text{eV}) = 18.4$ up to energies above $\log(E/\text{eV}) = 20$. The notation log refers to the decadic logarithm, \log_{10} , for all the analysis. After the selection cuts, a sample of 45951 events out of the available data between January 2004 and November 2009 is obtained. All stations fulfilling the cuts, of events in the same range are taken into account. Figure 5.3 shows the obtained benchmarks for $\theta = 38^\circ$.

For every event, the risetime function defined in equation 4.20 is fitted to the station data. All parameters are fixed to the values of the benchmark except ε_{a1} , which is the free parameter of the fit.

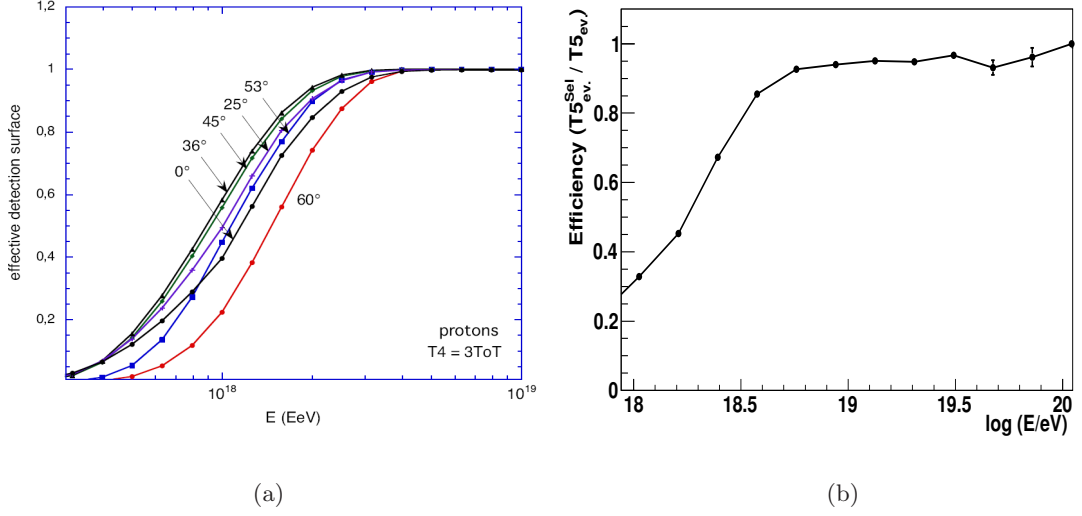


Figure 5.2: (a) Detection efficiency of proton showers for T5 trigger condition [203]. (b) Efficiency of the SD detector of T5 showers fulfilling the conditions imposed for the analysis, $\theta < 60^\circ$.

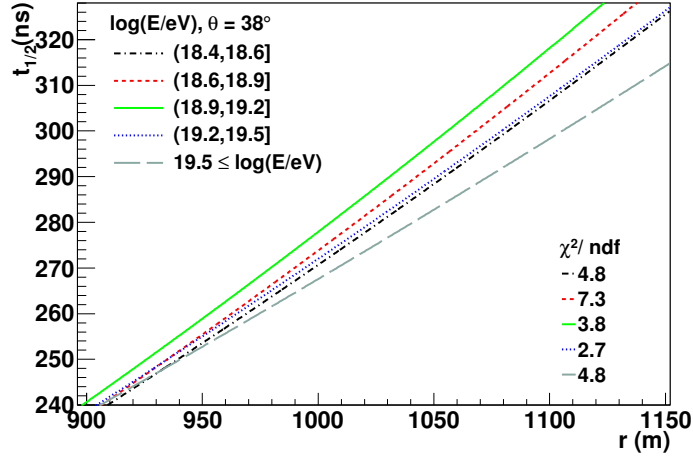


Figure 5.3: The five benchmarks obtained for the calculation of Δ_{1000} parameter at $\sec \theta = 1.3$.

Δ_{1000} as a function of Zenith Angle The risetime is affected by the limitation of the bin size of recorded data and by the SPR effect, leading to a minimum value of 40 ns, as explained in Section 4.3. The parameter $t_{\frac{1}{2}}(1000)$ is also affected by this limitation as can be observed in Fig. 4.23. Signals become faster with increasing θ , which can not be properly reflected. The line corresponding to measured data has a different slope from $\sim \sec \theta = 1.7$ on, which is an artefact of the experiment limitations. For simulations, the increase appears already at $\sim \sec \theta = 1.5$. The parameter Δ_{1000} is still affected, which is shown in Fig. 5.4. Four ranges of energy are explored, each one has an offset of 0.5 units to make its behavior more visible. The dotted line represents a constant fit to the points and the solid line shows

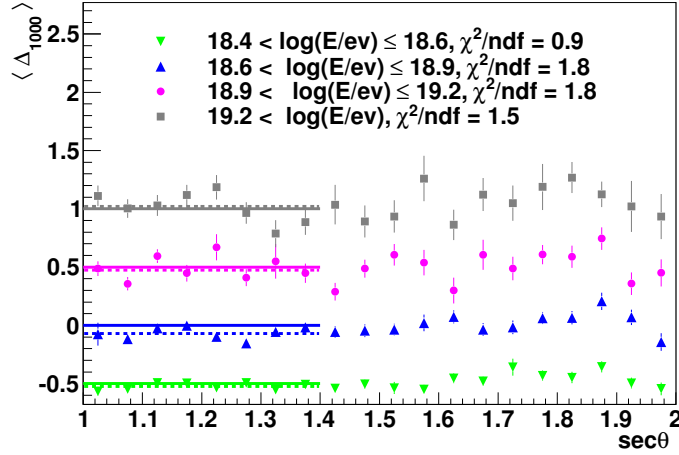


Figure 5.4: Δ_{1000} parameter as a function of zenith angle for four ranges of energy. Solid lines are the expected value and the dotted lines are fits of a constant to the points. The behavior is constant up to $\sim \sec \theta = 1.4$.

the expected value of zero, according to the definition of Δ_{1000} . The parameter is found to be constant with θ until $\sim \sec \theta = 1.4$ above which a small bias and larger fluctuations for energies between $\log(E/eV) = 18.9$ and $\log(E/eV) = 19.2$ can be observed. Therefore, only showers with zenith angles up to $\sim \sec \theta = 1.4$ are taken into account to define an appropriate parameter which behaves constant with zenith angle as expected for calibrating with X_{\max} .

Δ_{1000} as a function of Energy After applying all cuts including $1.0 \leq \sec \theta \leq 1.4$, the efficiency of the SD detector to T5 events fulfilling the conditions is shown in Fig. 5.5(a). The T5 detection efficiency is $\sim 65\%$ at $10^{18.4}$ eV and reaches $\geq 78\%$ at $10^{18.5}$ eV.

According to the definition of Δ_{1000} (Eq. 5.1), its fluctuations should be minimized. This will allow to measure the relation between X_{\max} and Δ_{1000} with small statistical uncertainties during the calibration procedure. Figure 5.5(b) shows Δ_{1000} parameter as a function of energy. As can be seen, the measured Δ_{1000} is constant over all energies as it should be by construction. With respect to three ranges of zenith angle, the values agree with uncertainties and no systematic trend with θ is observed as shown in Fig. 5.6(a). The shape of the different samples can be better observed in Fig. 5.6(b), where values are having an offset of 0.5 units for every range of zenith angle. The evolution of Δ_{1000} with the energy is stable for every range of zenith angle up to $\log(E/eV) = 19.6$.

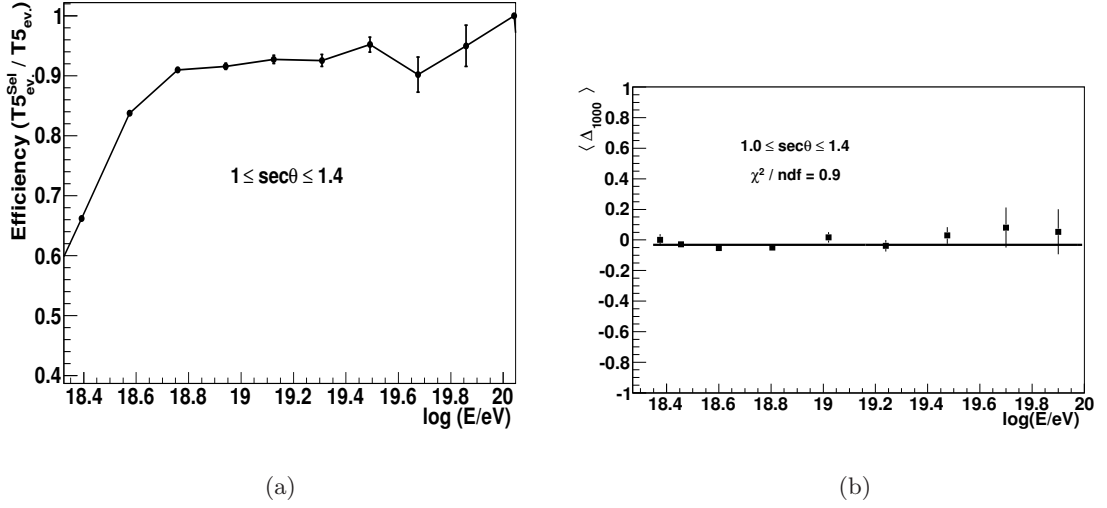


Figure 5.5: (a) Efficiency of the SD detector to T5 showers fulfilling the conditions imposed for the analysis, $\theta < 44^\circ$ ($\sim \sec\theta = 1.4$). (b) Δ_{1000} parameter as a function of energy. The notation log refers to the decadic logarithm, \log_{10} .

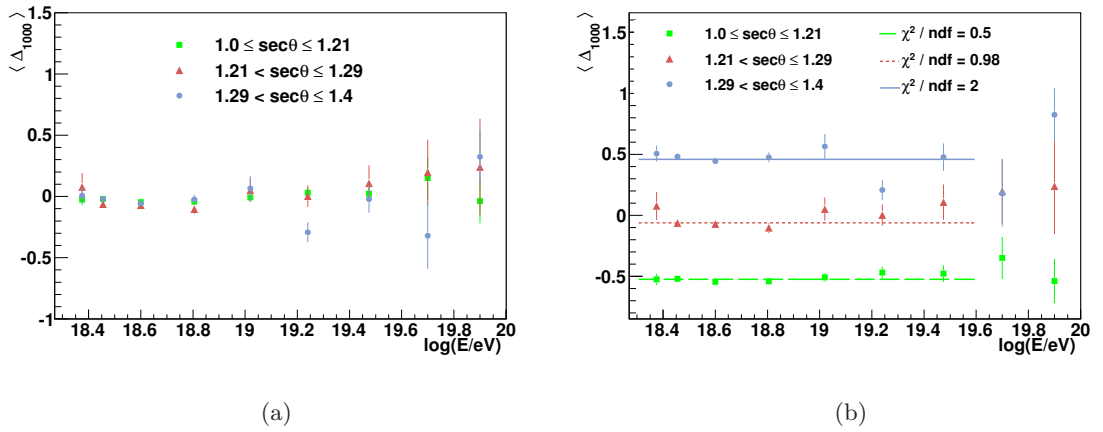


Figure 5.6: (a) Δ_{1000} parameter as a function of energy for three ranges of zenith angle. (b) Showing an offset of 0.5 units to allow the observation of the shape of the distributions. The line shows the fit of a constant to the data.

5.2 Calibration of Δ_{1000} with X_{\max}

The SD detector take data with a duty cycle of 100% while in the case of the FD detector the data taking is restricted to clear, moonless nights and moreover the atmospheric conditions have to be monitored very precisely. This reduces the FD duty cycle to 13% [165]. The result is a lower FD statistics in comparison with the one available from SD. Studies on X_{\max} parameter may become more robust at energy bins for which FD statistics is low if SD observables calibrated with X_{\max} are used. The observable to be considered for this purpose is Δ_{1000} . The sample of 3754 hybrid data explored in Ref. [3] for studies on depth of maximum of extensive air showers above $\log(E/\text{eV}) = 18$, is taken into account. After applying the SD cuts to the sample, 1022 events are left, from which 506 events above $\log(E/\text{eV}) = 18.4$ are selected for the present analysis. The $\langle X_{\max} \rangle$ as a function of energy is shown in Fig. 5.7 for all FD events and for only the events selected for this analysis. As can be seen the two samples are in good agreement above the energy threshold of $10^{18.4}$ eV considered here and it can be concluded, that the additional SD requirements do not introduce a bias in the $\langle X_{\max} \rangle$ (and hence in the mass composition).

A correlation of Δ_{1000} with the depth of the shower maximum is expected, as it was explained in Section 5.1. This correlation is shown in Fig. 5.8(a). The correlation coefficient is $r = 0.3$ for all available events. The lines corresponding to the uncertainties of X_{\max} are given by the measurement made with the FD detector. To minimize the correlation of the fit parameters, a translation with respect to the mean value, $\langle X_{\max} \rangle$ of all data is plotted, allowing to consider only the correlation with Δ_{1000} out of statistical fluctuations. The correlation is still observed in Fig. 5.8(b), only the origin ordinate changes as it was expected.

The calibration is made with a linear function $\Delta_{1000} = a + b \cdot (X_{\max} - \langle X_{\max} \rangle)$ which is found to be sensitive to the energy as shown in Fig. 5.9, where the corresponding slope differs from $0.0078 \text{ cm}^2 \text{ g}^{-1}$ at $\log(E/\text{eV}) = 18.5$ to $0.012 \text{ cm}^2 \text{ g}^{-1}$ at $\log(E/\text{eV}) = 18.6$. Therefore, the calibration is done for eight energy ranges and the corresponding parameters are expressed as a function of the energy as shown in Figs. 5.10(a) and 5.10(b). The energies for which the linear fits are performed are $18.5 < \log(E/\text{eV}) < 19.6$. The lower limit is chosen since the detection of showers fulfilling the conditions imposed for the analysis is $\sim 78\%$ at $\log(E/\text{eV}) = 18.5$ for $\sec \theta < 1.4$ as shown in Fig. 5.5(a), ensuring reliable results. The upper limit of the energy is based on the distribution of Δ_{1000} parameter shown in Fig. 5.6(b) where values are stable up to $\log(E/\text{eV}) = 19.6$. Moreover, the statistics for higher energies is low according to Fig. 5.10. Δ_{1000} parameter as a function of X_{\max} is thus expressed as following:

$$\Delta_{1000}(E, X_{\max}) = a(E) + b(E) \cdot (X_{\max} - \langle X_{\max} \rangle), \quad (5.2)$$

where $\langle X_{\max} \rangle$ is chosen to be the mean value of the depth of the shower maximum corresponding to the 388 hybrid data having $18.5 < \log(E/\text{eV}) < 19.6$, which were taken into account for the calibration procedure, the value is $\sim 745 \text{ g cm}^{-2}$. The parameters are found to be: $a(E) = (4.74 \pm 2.13) + (-0.25 \pm 0.11) \cdot \log(E)$ and $b(E) = (0.047 \pm 0.051) + (-0.002 \pm 0.0027) \cdot \log(E)$ ¹.

¹The point at $\sim 10^{19.1}$ eV could be an outlier. It has been verified that excluding this point from the calibration does change the results by only less than 10 g cm^{-2} .

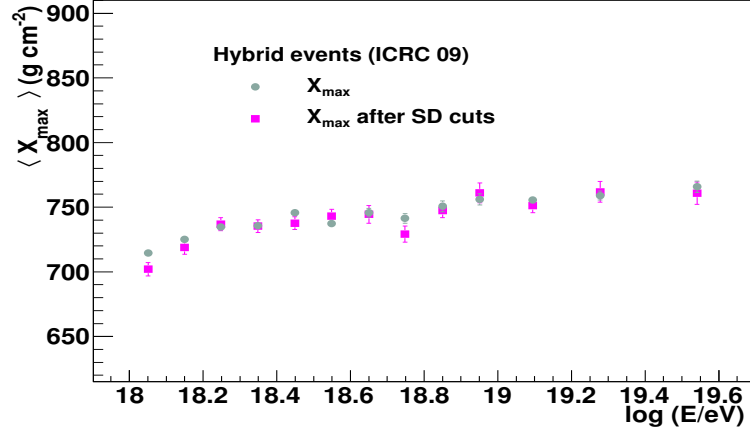


Figure 5.7: Comparison of the hybrid data used for the calibration of Δ_{1000} with X_{\max} , before and after applying SD cuts. The values of X_{\max} were presented by the Pierre Auger Collaboration in the 31st International Cosmic Ray Conference in 2009 [204].

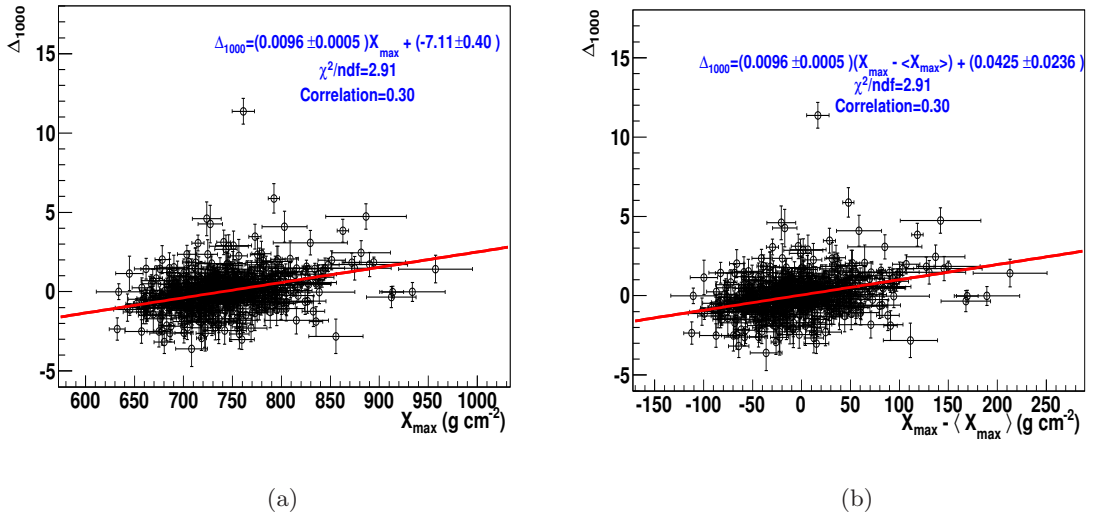


Figure 5.8: (a) Δ_{1000} as a function of X_{\max} , showing a correlation between both observables. (b) Δ_{1000} as a function of $X_{\max} - \langle X_{\max} \rangle$ minimizing the correlation of the fit parameters. The events are having $18.4 \leq \log (E/eV)$ and $1.0 \leq \sec \theta \leq 1.4$. Uncertainties of X_{\max} are estimated from the measurement made with the FD.

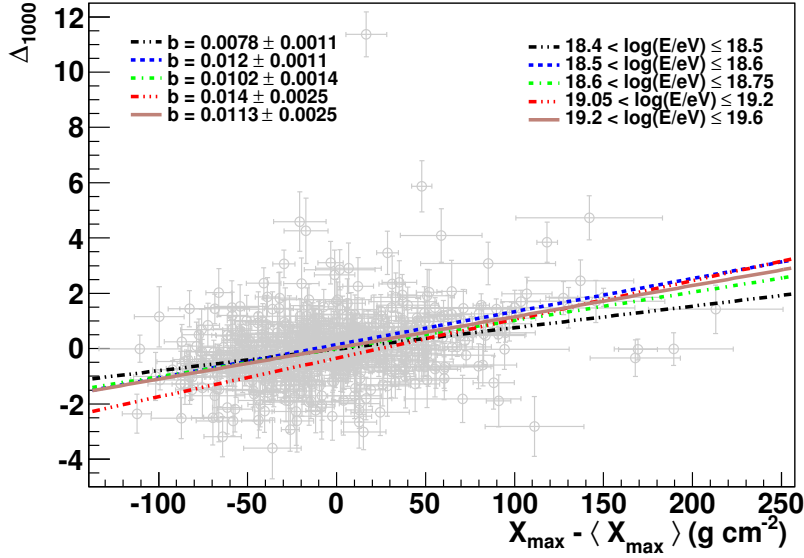


Figure 5.9: Calibration of Δ_{1000} parameter with X_{\max} for five ranges of energy.

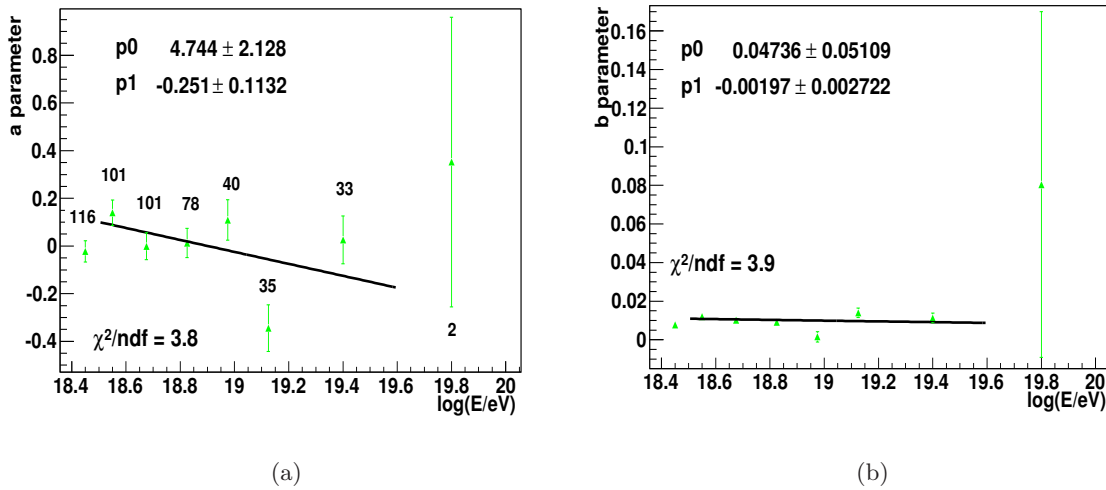


Figure 5.10: (a) Parameter “a” as a function of the energy. (b) Parameter “b” as a function of the energy. Parameters p_0 and p_1 are the corresponding origin ordinate and slope, respectively. The numbers attached to the points represent the number of events in each range of energy.

Identification of possible biases in the calibration It is necessary to prove that the calibration is able to reflect the trend of X_{\max} with the energy, through the Δ_{1000} parameter. The evaluation of residuals between Δ_{1000} and $\Delta_{1000}^{\text{Cal}}$, the value obtained from the calibration, gives information about the reliability of the result. Residuals are shown in Fig. 5.11(a) as a function of the energy, for $18.5 < \log(E/\text{eV}) < 19.6$. No bias with increasing energy is observed within statistical uncertainties. Residuals do not show any bias with respect to the zenith angle either, as it can be seen in Fig. 5.11(b). Only an overestimation in the first bin, corresponding to few vertical showers is observed. Hence, it can be concluded that the method is reliable for studies on X_{\max} .

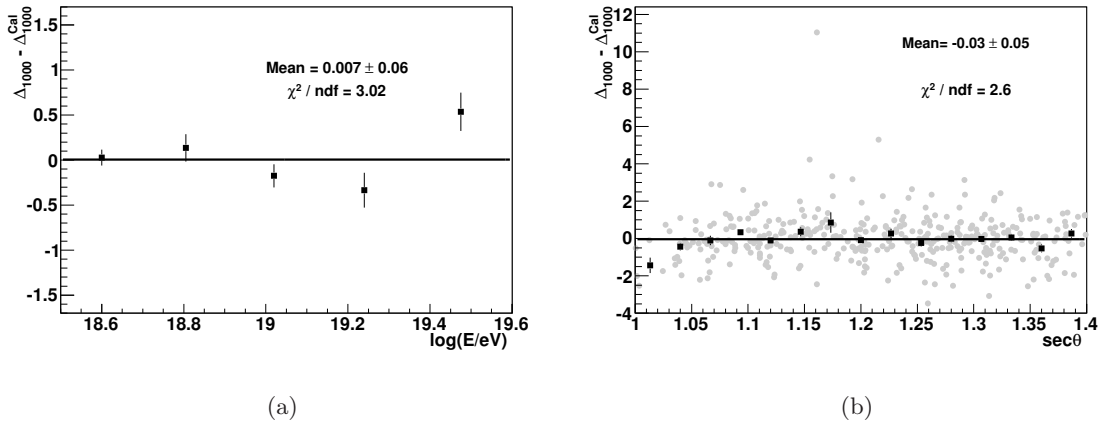


Figure 5.11: Comparison of Δ_{1000} value with the one obtained from the calibration procedure, $\Delta_{1000}^{\text{Cal}}$, (a) as a function of the energy and (b) as a function of the zenith angle.

5.3 The SD depth of the shower maximum, X_{\max}^{SD}

The depth of the shower maximum obtained from SD measurements is calculated using the inverse of equation 5.2, applied to all SD available data fulfilling the required cuts, between January 2004 and November 2009 (45951 events). The value for events with energy above $\log(E/\text{eV}) = 19.6$ are obtained from extrapolation. A comparison of X_{\max}^{SD} with X_{\max}^{FD} as a function of the energy shows a good agreement between both kind of depth of the shower maximum on average basis, as can be seen in Fig. 5.12. It is clear that the statistics for energies above $10^{19.4}$ eV increases about 15 times for SD measurements with respect to FD data. This allows to get more information concerning this observable at such high energies, at least in a conservative sense regarding the statistical uncertainties, which correspond to the error of the mean value in each bin. Moreover, the energy range of measurements for X_{\max} of the Pierre Auger Observatory has been extended to energies of $10^{19.9}$ eV, i.e., by a factor of 2.3 with respect to the range of energies reached for the FD analysis, which is of about $10^{19.5}$ eV only.

As shown in Fig. 5.13, X_{\max}^{SD} is stable with the zenith angle. This means that no bias with zenith angle is introduced by obtaining X_{\max}^{SD} from using the inverse of the calibration. This is expected since Δ_{1000} and $\Delta_{1000}^{\text{Cal}}$ do not exhibit any bias with zenith angle, as discussed in Sections 5.1 and 5.2.

The agreement between SD and FD data can be illustrated better by comparing the fractional residuals between the average X_{\max} at given energies, $\langle X_{\max} \rangle(E)$, and the average over all energies, $\langle X_{\max} \rangle$ for both kind of measurements. Fig. 5.14 shows that the residuals in X_{\max}^{SD} and X_{\max}^{FD} , for the data used in the calibration procedure, do also agree, having a maximum difference up to 3% within the errors bars, which confirms that X_{\max}^{FD} and Δ_{1000} evolve similarly with the energy. This conclusion is important for the use of X_{\max}^{SD} in mass composition studies, as will be discussed in Chapter 6. Nevertheless, the fluctuations of X_{\max} , $\text{RMS}(X_{\max})$, are not comparable as shown in Fig. 5.15. The SD sample is enriched for stations triggered by heavy nuclei at low energies, leading to small fluctuations in that region, while for energies above $\log(E/\text{eV}) = 18.5$, fluctuations are larger than the corresponding to FD data. The difference can be understood if the detector resolution, effects due to the event selection and measurement uncertainties are taken into account. In Section 5.4 some results on this topic are discussed.

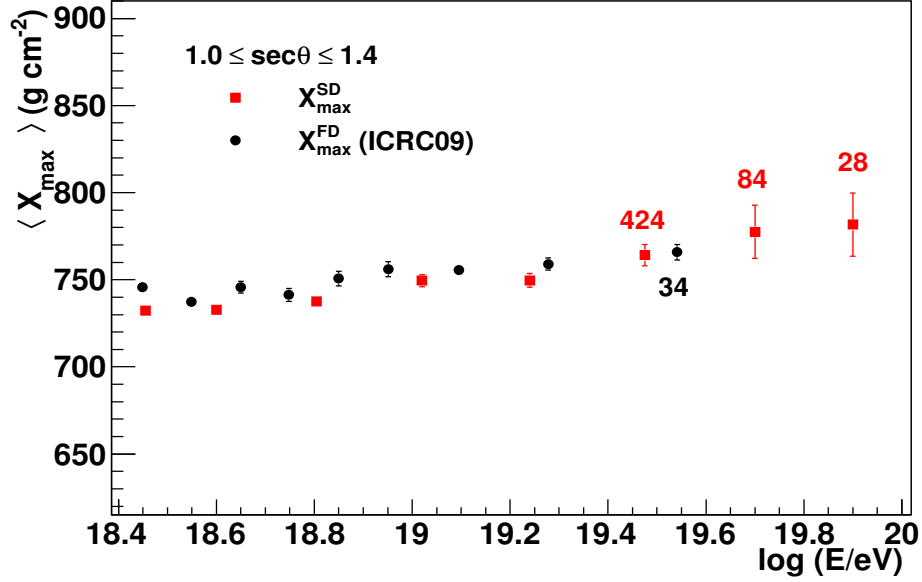


Figure 5.12: Comparison of the depth of the shower maximum obtained from FD and SD measurements. The agreement between both kind of values is clear. The numbers indicate the number of events in the corresponding energy bin.

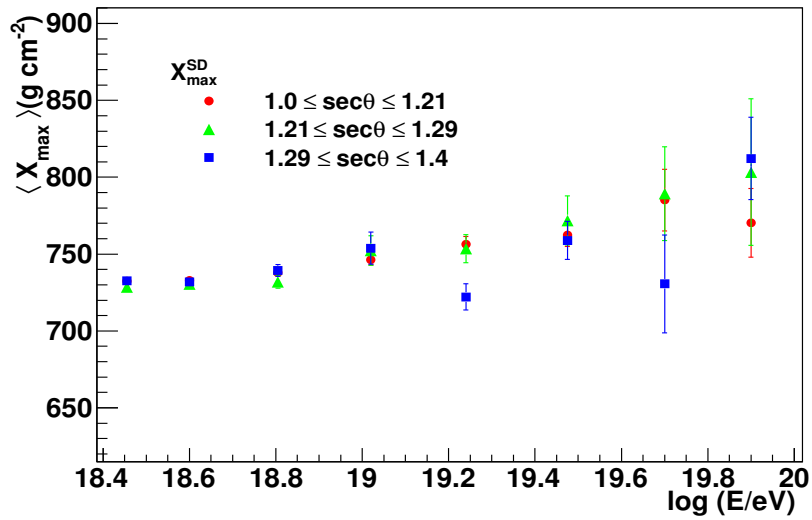


Figure 5.13: X_{\max}^{SD} as a function of energy. There is no systematic deviation with respect to the zenith angle.

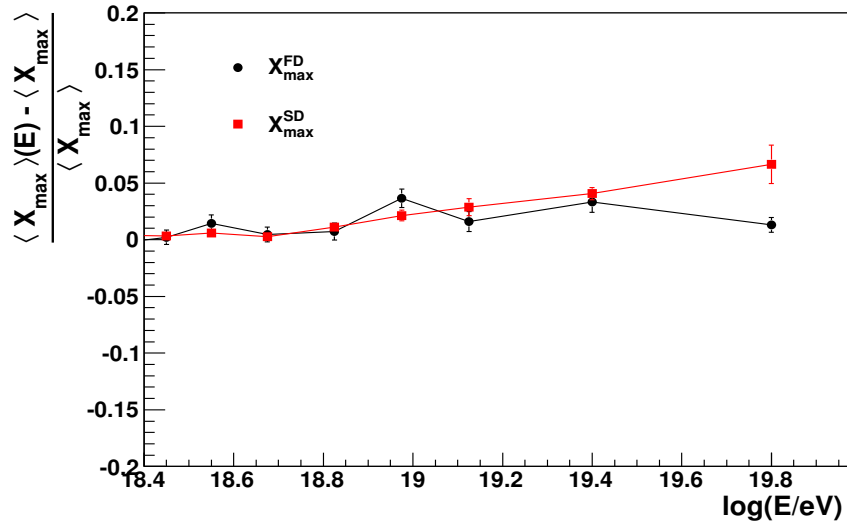


Figure 5.14: Fractional residuals between the average X_{\max} at a given energy and the average over the entire energy range, $\langle X_{\max} \rangle$, as a function of the energy for FD and SD data. They agree quite well.

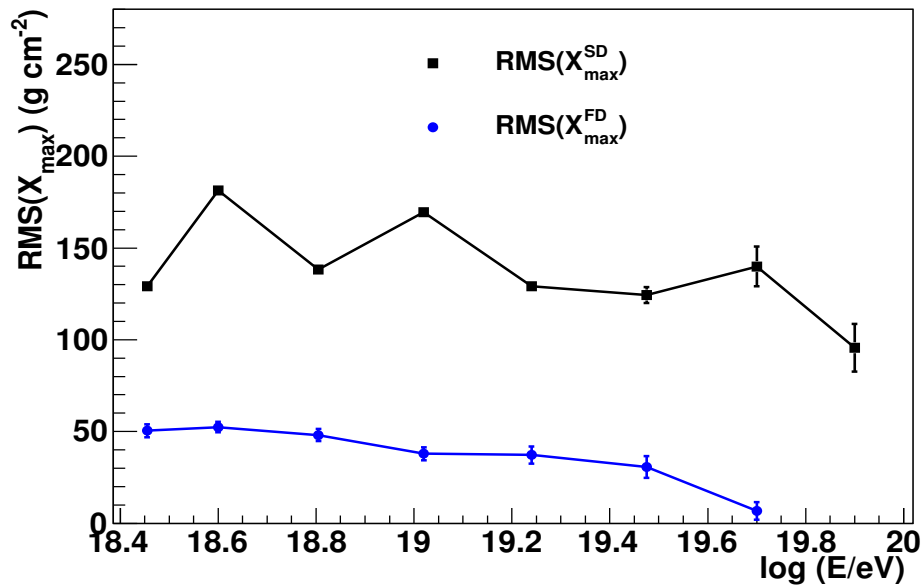


Figure 5.15: Comparison of X_{\max} fluctuations for SD and FD data.

5.4 Estimation of Uncertainties in X_{\max}^{SD}

The uncertainties involved in the method used for obtaining X_{\max}^{SD} based on Δ_{1000} parameter have several sources. Some of them are related with the detector itself, that means, the contributions from SD and FD measurements. Others are related with the treatment of risetime for defining the Δ_{1000} observable and all required calibration procedures. In this section the sources of uncertainties are explored and some estimations of their contributions are deduced.

Systematics from FD measurements The measurement of the FD energy scale, as mentioned in Section 2.2, is having a systematic uncertainty of 22%, being dominated by the contribution of the fluorescence yield. In the case of uncertainties corresponding to X_{\max} , the sources are calibration, atmospheric conditions, reconstruction and event selection. All contributions give rise to a systematic uncertainty of $\leq 13 \text{ gcm}^{-2}$ for the average depth of the shower maximum, $\langle X_{\max} \rangle$, and $\leq 6 \text{ gcm}^{-2}$ for the shower to shower fluctuations, $\text{RMS}(X_{\max})$. The measured $\langle X_{\max} \rangle$ and RMS values are independent of zenith angle, time periods and FD stations [3].

Systematics from SD measurements For the SD energy scale, as mentioned in Section 2.1, there are additional systematic uncertainties due to the calibration procedure. They amount to 7% at 10^{19} eV and 15% at 10^{20} eV, while the difference between the energy obtained from SD with respect to the one corresponding to FD is on average 2%, as shown in Figure 2.7(b).

Resolution of SD measurements Uncertainties from the treatment of risetime for obtaining Δ_{1000} are explored. Based on the method proposed in Ref. [175], to estimate the measurement uncertainty for individual values of Δ_{1000} , $\sigma_{\Delta_{1000}}$, it is necessary to obtain estimates of the contributions to this quantity from other sources. The expected contributions are described as following

- Random fluctuations introduced from uncertainties in the measurements of $t_{1/2}$, $t_{1/2}^{\text{BM}}(r, \theta, E)$ and $\sigma_{\Delta_{1000}}^{t_{1/2}}$.
- Random deviations introduced from uncertainties in the reconstruction procedure, $\sigma_{\Delta_{1000}}^{\text{rec}}$.
- Intrinsic fluctuations in the shower development, $\sigma_{\Delta_{1000}}^{\text{int}}$.

Contributions due to the estimation of the benchmark function for different energy ranges are not taken into account since they are $< 1\%$, as demonstrated later in this section. Contributions due to weather effects for this kind of study were demonstrated to be insignificant already in [175].

The quantity $\sigma_{\Delta_{1000}}$ is estimated from the residuals between measurements of Δ_{1000} and the average at a given shower energy range (ranges with $E \geq 3 \text{ EeV}$): $\Delta_{1000}^i - \langle \Delta_{1000} \rangle(E)$. The mean value of the residuals at a given number of triggered stations, N_S , corresponds

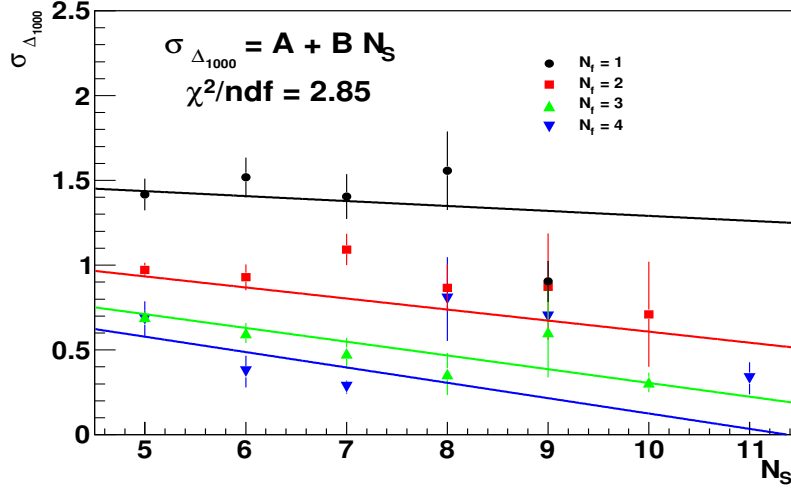


Figure 5.16: Estimated measurement uncertainties in Δ_{1000} as a function of the number of triggered stations, N_S .

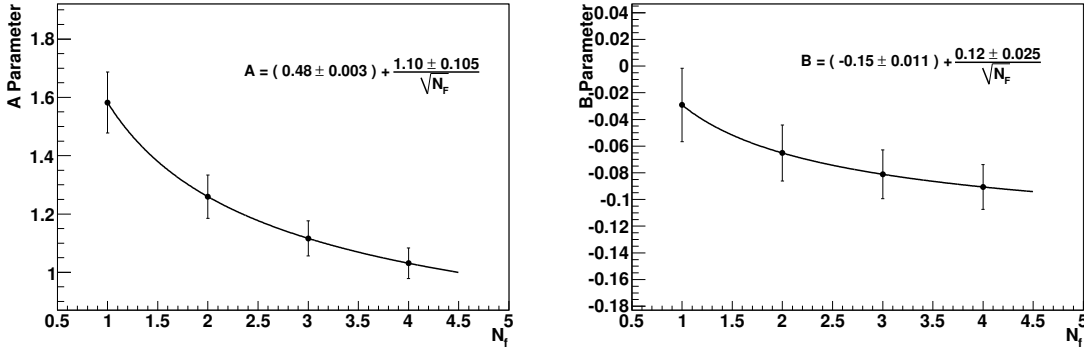


Figure 5.17: Parameters of $\sigma_{\Delta_{1000}}$ as a function of the number of stations considered for the fit of $t_{1/2}(r, \theta, E)$, N_F .

to $\sigma_{\Delta_{1000}}$. It is expected that $\sigma_{\Delta_{1000}}$ will be reduced in showers with increasing N_S as well as with increasing number of stations considered for the fit of $t_{1/2}(r, \theta, E)$, N_F . Figure 5.16 shows the parameterisation of $\sigma_{\Delta_{1000}}$ in terms of N_S , for events which satisfy the conditions for obtaining $\sigma_{\Delta_{1000}}^{t_{1/2}}$ and X_{\max}^{SD} , with parameters A and B being a function of N_F as shown in Fig. 5.17. It follows the form

$$\sigma_{\Delta_{1000}} = A + B N_S, \quad (5.3)$$

where

$$A = (0.48 \pm 0.003) + \frac{1.10 \pm 0.105}{\sqrt{N_F}}$$

$$B = (-0.15 \pm 0.011) + \frac{0.12 \pm 0.025}{\sqrt{N_F}}$$

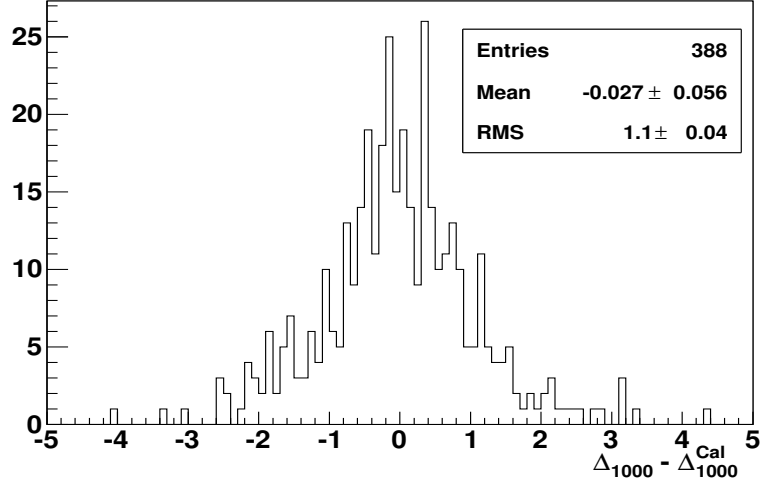


Figure 5.18: Residuals between the measured values of Δ_{1000} and those predicted from the calibration, $\Delta_{1000}^{\text{Cal}}$

From the parameterisations it is possible to estimate some of the contributions to $\sigma_{\Delta_{1000}}$. Contribution $\sigma_{\Delta_{1000}}^{\text{int}}$ can be estimated considering that fluctuations introduced by sampling and measurement uncertainties would be insignificant if N_s and the number of stations considered for the fit were infinite

$$\sigma_{\Delta_{1000}}^{\text{int}} \sim \lim_{N_F \rightarrow \infty} \sigma_{\Delta_{1000}} = 0.48 \pm 0.003 \sim 44.8 \pm 0.3 \text{ gcm}^{-2}. \quad (5.4)$$

The conversion from Δ_{1000} to X_{\max}^{SD} is made using the calibration obtained in Section 5.2 for the average energy of all considered SD events ($\langle \log(E/\text{eV}) \rangle = 18.6$). This is already a first estimation of the fluctuations of X_{\max} . The contribution of $\sigma_{\Delta_{1000}}^{t_{1/2}}$ is by definition 1 and the minimum value of $\sigma_{\Delta_{1000}}$ should come from the simplest scenario where $N_S = 3$ (the minimum necessary for SD event reconstruction) and $N_F = 1$. In this case $\sigma_{\Delta_{1000}} = 1.49$. Contributions of $\sigma_{\Delta_{1000}}^{\text{rec}}$ are estimated as following:

$$\begin{aligned} \sigma_{\Delta_{1000}}^{\text{rec}} &\sim \sqrt{\sigma_{\Delta_{1000}}^2 - (\sigma_{\Delta_{1000}}^{t_{1/2}})^2 - (\sigma_{\Delta_{1000}}^{\text{int}})^2} \\ &\sim \sqrt{(1.49)^2 - 1^2 - (0.48)^2} \\ &\sim 0.995 \end{aligned}$$

The fraction of each contribution to $\sigma_{\Delta_{1000}}$ is: $\frac{1^2}{1.49^2} = 45\%$ (for $\sigma_{\Delta_{1000}}^{t_{1/2}}$), $\frac{0.995^2}{1.49^2} = 44.6\%$ (for $\sigma_{\Delta_{1000}}^{\text{rec}}$) and $\frac{0.48^2}{1.49^2} = 10.4\%$ (for $\sigma_{\Delta_{1000}}^{\text{int}}$). The dominant contribution to the uncertainty is coming from the measurement of risetime and from the reconstruction procedure, a cross-check on this issue done with simulations, is discussed in Chapter 6.

Using this parameterisation for $\sigma_{\Delta_{1000}}$ it is possible to compare the fluctuations of the $\Delta_{1000}^{\text{Cal}}$ obtained from the calibration of $\sigma_{\Delta_{1000}}$ with X_{\max} , from the residuals between Δ_{1000} and the predicted $\Delta_{1000}^{\text{Cal}}$. Residuals are having a standard deviation of $\sigma_{\Delta_{1000}}^{\text{Meas}} = 1.1 \pm 0.04$ (see Fig. 5.18) while values obtained from equation 5.3, taking into account that for the same sample, $\langle N_S \rangle = 2.75$ and $\langle N_F \rangle = 1.92$, $\sigma_{\Delta_{1000}} = 1.1 \pm 0.09$. Both values are consistent.

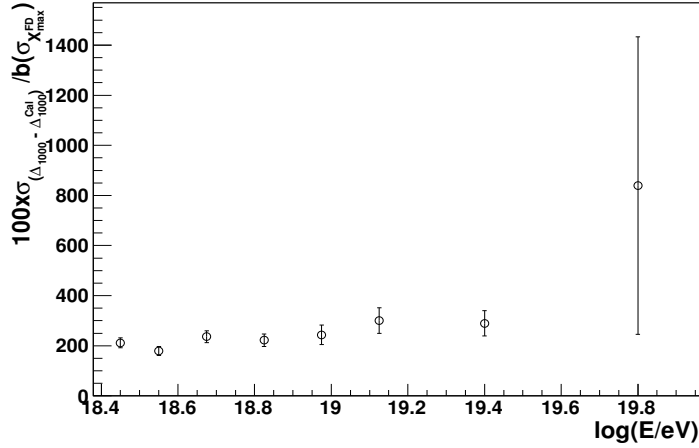


Figure 5.19: Comparison of range in $\sigma_{X_{\max}^{\text{FD}}}$ with fluctuations resulting from calibration of Δ_{1000} as a function of the energy. Parameter “b” is the slope of the calibration of Δ_{1000} with X_{\max}

Fluctuations in X_{\max}^{SD} can be also estimated from the fluctuations observed in the calibration of Δ_{1000} as evaluated from the slope, i.e. $\sigma_{\Delta_{1000}}/\sigma_{X_{\max}^{\text{SD}}} = b$. This fluctuations are compared with the corresponding range in $\sigma_{X_{\max}^{\text{FD}}}$ as shown in Fig. 5.19. For $19 < \log(E/\text{eV})$ fluctuations in calibration are around two times the FD fluctuations and for energies above, this value is at least three times larger. From this information, an estimation of the uncertainty introduced by extrapolation of the calibration can be obtained for the highest energy bin, it may introduce uncertainties of at least three times the fluctuations observed in X_{\max}^{FD} . According to the corresponding $\sigma_{X_{\max}^{\text{SD}}}$ for the $\sigma_{\Delta_{1000}}$, described before in this section, it is observed in Fig. 5.20 that $\sigma_{X_{\max}^{\text{SD}}}$ also decreases with increasing N_F . Values are going from $\sim 160 \text{ gcm}^{-2}$ to $\sim 60 \text{ gcm}^{-2}$. Nevertheless, since the average difference in X_{\max} between protons and iron at UHEs is $\sim 80 \text{ gcm}^{-2}$, the measurement uncertainty in X_{\max}^{SD} is too large to be used in composition measurements on an event-by-event basis.

Fluctuations in $\sigma_{X_{\max}^{\text{SD}}}$ shown in Fig. 5.20 can be also interpreted as the X_{\max}^{SD} resolution, which is having a minimum value of $\sim 60 \text{ gcm}^{-2}$. This is large compared with the resolution for X_{\max}^{FD} , which is at the level of $\sim 20 \text{ gcm}^{-2}$ [3]. This difference explains the separation between $\text{RMS}(X_{\max}^{\text{SD}})$ and $\text{RMS}(X_{\max}^{\text{FD}})$ observed in Fig. 5.15. Using the function obtained from the relation between $\sigma_{X_{\max}^{\text{SD}}}$ and N_F , the resolution of the SD detector as a function of the energy can be seen in Fig. 5.21. The mean value is around 100 gcm^{-2} at high energies. Another estimation of the SD resolution can be done observing the fluctuations of X_{\max}^{SD} with respect to the corresponding FD data. The plot in Fig. 5.22 shows these fluctuations as a function of energy, the mean value is about 100 gcm^{-2} , which is in good agreement with the estimation obtained in Fig. 5.21.

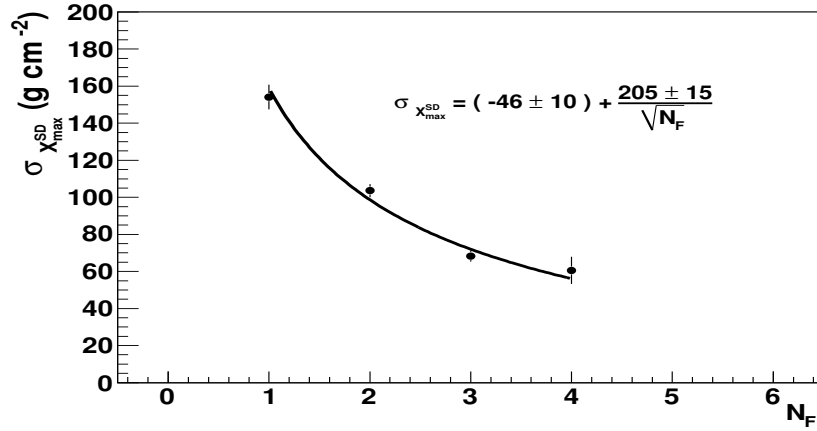


Figure 5.20: Uncertainties of X_{\max}^{SD} for data with energies between $\log(E/eV) = 18.5$ and $\log(E/eV) = 19.6$ and $1.0 \leq \sec\theta \leq 1.4$, arising from measurement of Δ_{1000} .

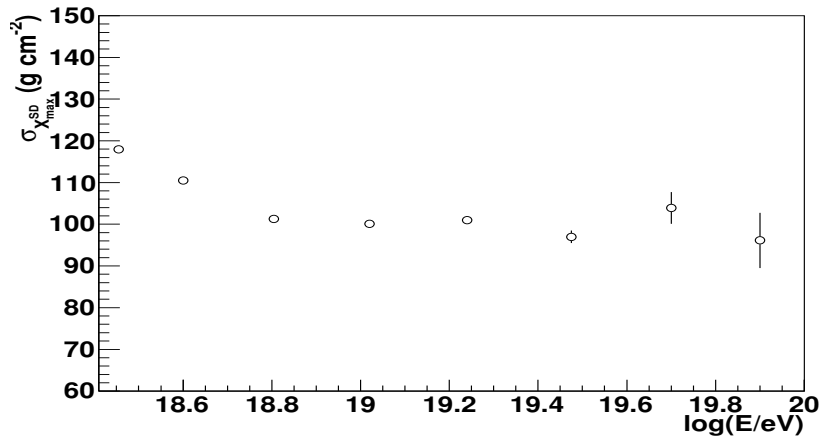


Figure 5.21: Estimation of the resolution for X_{\max}^{SD} as a function of the energy based on the number of stations N_F .

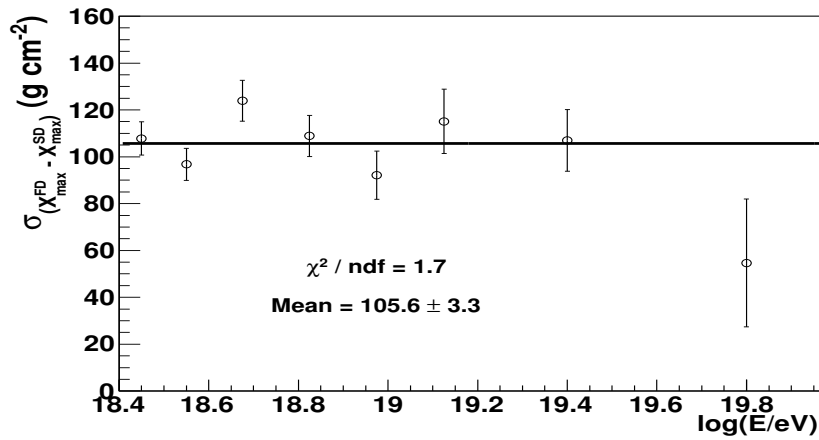


Figure 5.22: Estimation of the resolution of the SD detector for X_{\max}^{SD} .

Chapter 5. Δ_{1000} as a mass composition sensitive parameter

The event selection in SD is such that several events with particular non standard conditions passed the cuts contributing to the large fluctuations observed. Some examples are presented in the next lines. Since it is possible to use only one station to perform the fit of risetime as a function of the distance from the shower core, it can be the case that this unique station is an outlier of the event, resulting in a big value of Δ_{1000} . Figure 5.23 shows an example of this kind of events, the risetimes are non corrected for azimuthal asymmetry and the error bars are the measurement uncertainties. The unique station fulfilling the cuts is an outlier. The FADC traces for two of the PMTs contain contributions from incidental particles, resulting in an enormous measurement error. The corresponding $\Delta_{1000} = 20$ is also big. Figure 5.24

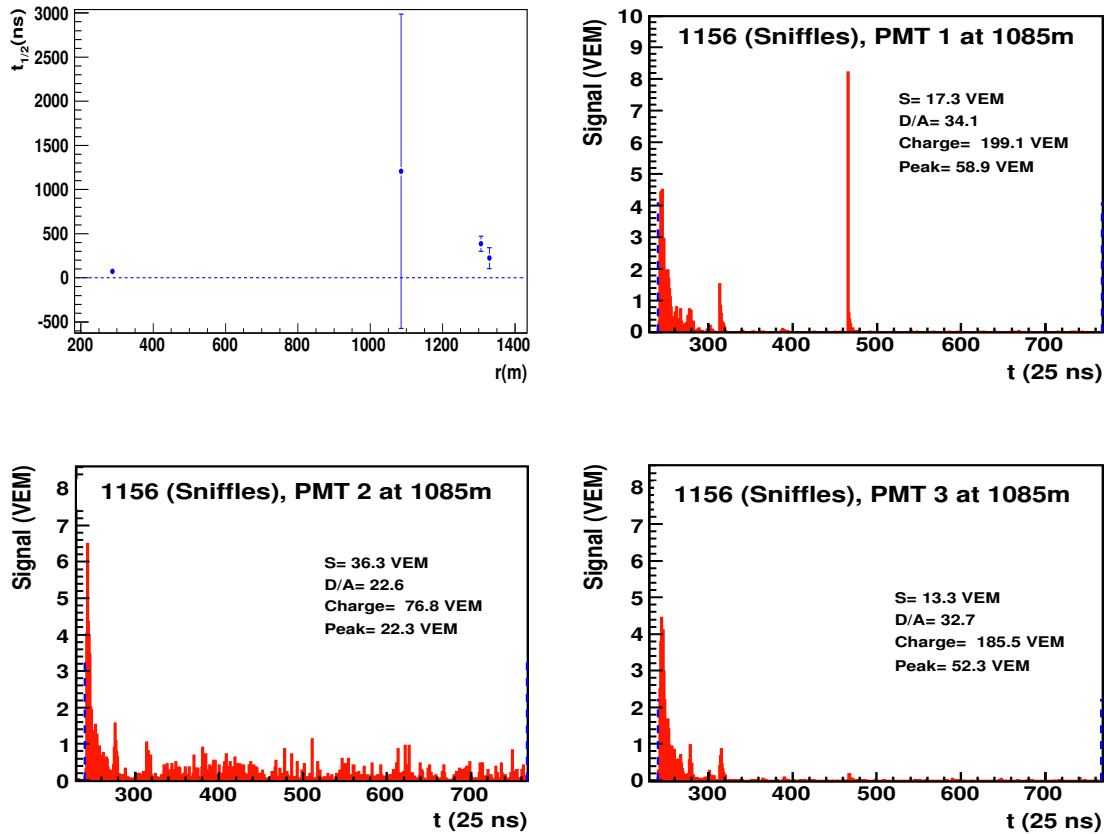


Figure 5.23: Event containing one station fulfilling the cuts, which is an outlier risetime (id 200717103531). The error bars correspond to the measurement uncertainty.

shows another example of events where the uncertainty of $t_{1/2}$ of some of the stations is huge, it corresponds to the outlier of the plots in Fig. 5.6, which has a $\Delta_{1000} = 11.4$. There are two stations fulfilling the conditions between 600 m and 1200 m but one of these has a big $t_{1/2}$ produced by accidental particles in one of its PMTs as it can be seen in the FADC trace. Since there is no cut on the measurement uncertainty of $t_{1/2}$, the event was not rejected. The fit of risetime as a distance from the shower core takes into account the parameterisation $\sigma_{t_{1/2}}$ but not the measurement uncertainty, thus, the event was properly processed. Another special event is shown in Fig. 5.25, values of risetime are all too large, corresponding to the case of lightning according to the VEM traces. The surrounding stations are reported as lightning as well. Nevertheless, the event passed the cut against lightning stations and was

still reconstructed as a T5.

Fluctuations of Δ_{1000} still need to be properly understood finding the ideal cuts for event selection such as the cuts needed on the measurement uncertainty of risetime, which has been observed in the exposed examples. This may allow an accurate deduction of the resolution of the SD detector and thus, to correct the $\text{RMS}(X_{\max})$ for estimating the shower to shower fluctuations.

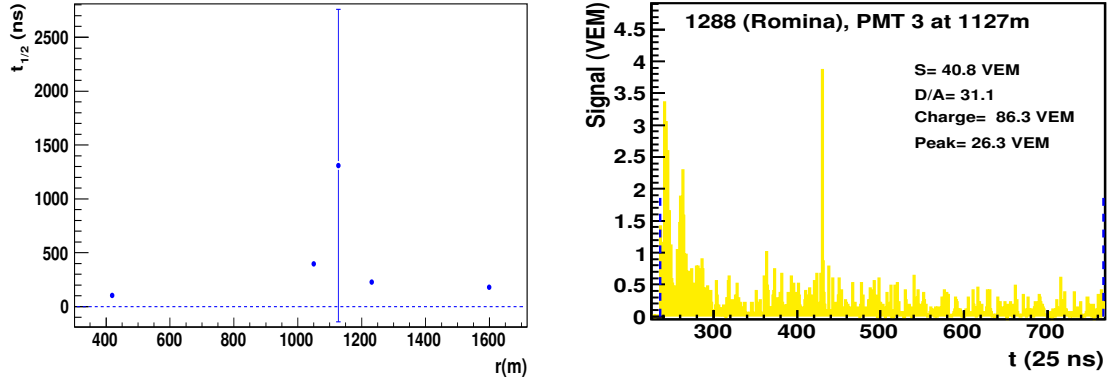


Figure 5.24: Event containing one outlier risetime passing the analysis cuts (id 200823705096).

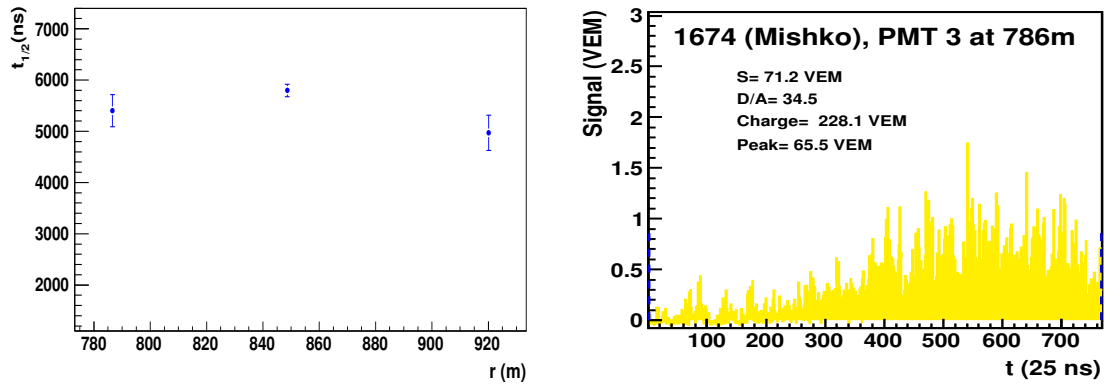


Figure 5.25: Event containing stations type lightning but passing the analysis cuts (id 200902604794).

Systematics from benchmarks The use of several benchmarks for five ranges of energy could introduce bias in the transition region from one to the other range. To explore this possibility, the parameters of the five benchmarks are expressed as function of energy. Using this continuous parameterisation, $X_{\max}^{\text{SD}}(BM)$, the analysis is repeated and the results are compared to the non-parametric approach.

The best parameterisation found agrees well with the original mean values of X_{\max}^{SD} as shown in Fig. 5.26. The fractional difference between both kind of quantities is in average less than 1%. The difference can be up to $\sim 6\%$ for high energies, where the statistics is low, but it is within the statistical uncertainties. It can be concluded that no significant systematic uncertainty is introduced by using several ranges for calculating the benchmark functions.

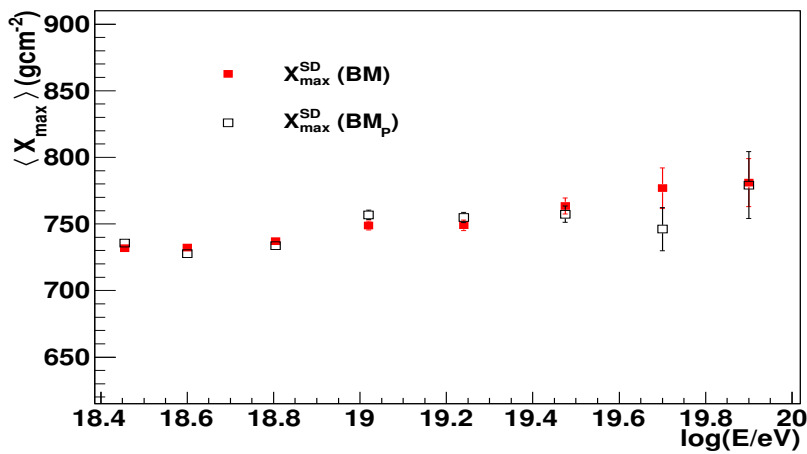


Figure 5.26: Comparison of X_{\max}^{SD} obtained from several fixed benchmarks, with the values obtained by using the parameterisation of the benchmarks as a function of the energy.

Systematics from Calibration of Δ_{1000} with X_{\max}^{FD} Uncertainties introduced by the calibration procedure of Δ_{1000} with X_{\max}^{FD} are estimated using the mean value of $\Delta_{1000}^{\text{Cal}}$, the value obtained from equation 5.2. The same events used for obtaining the calibration are considered. Seven bins of $X_{\max} - \langle X_{\max} \rangle$ are taken into account for obtaining the mean value and the corresponding statistical error in $\Delta_{1000}^{\text{Cal}}$. The statistical uncertainties from the calibration are obtained by fluctuating each one of the seven points in Fig. 5.27 within a Gaussian centered on the average $\Delta_{1000}^{\text{Cal}}$ value as suggested in Ref. [175, 187]. The standard deviation is given by the statistical error of the point. The procedure is repeated 1000 times. By each fluctuation a linear fit over all points is made and some values of $X_{\max} - \langle X_{\max} \rangle$ along the whole range are evaluated. The corresponding $\Delta_{1000}^{\text{Cal}}$ are stored in histograms which give the information about minimum and maximum values necessary to estimate an area bounding the fitted lines. The calculation is made for two areas, the 1σ area (continuous line in the plot) corresponds to the Gaussian with one standard deviation order and the 2σ area corresponds to two standard deviation order (dashed line in the plot).

A comparison of X_{\max}^{FD} with X_{\max}^{SD} showing the uncertainties introduced by the calibration procedure (1σ area) is shown in Fig. 5.28. Both samples are in good agreement within statistical and systematic uncertainties. Thus, it can be concluded that the calibration of Δ_{1000} with X_{\max}^{FD} is a reliable method on average basis within statistical and systematic uncertainties. Deductions about mass composition using the Δ_{1000} method are made in the next chapter.

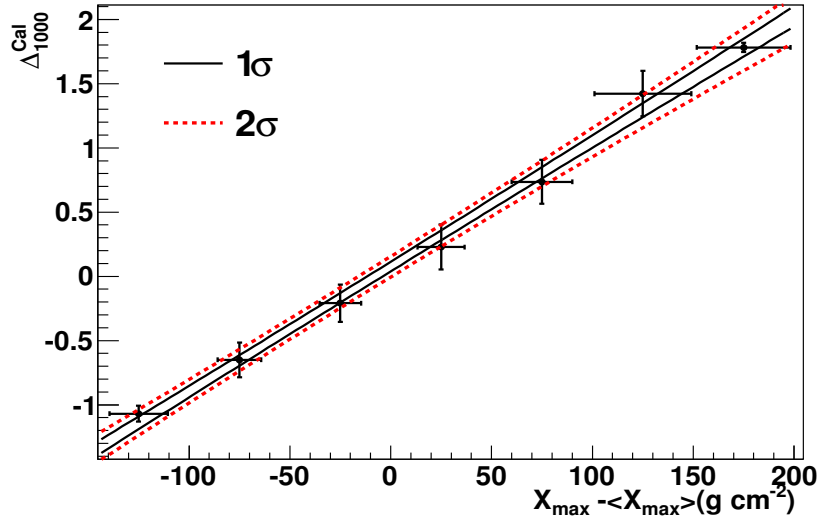


Figure 5.27: $\Delta_{1000}^{\text{Cal}}$ as a function of $X_{\max} - \langle X_{\max} \rangle$. The error bars show the spread of data and the lines show the areas 1σ and 2σ obtained from fluctuations over the statistical errors of each point.

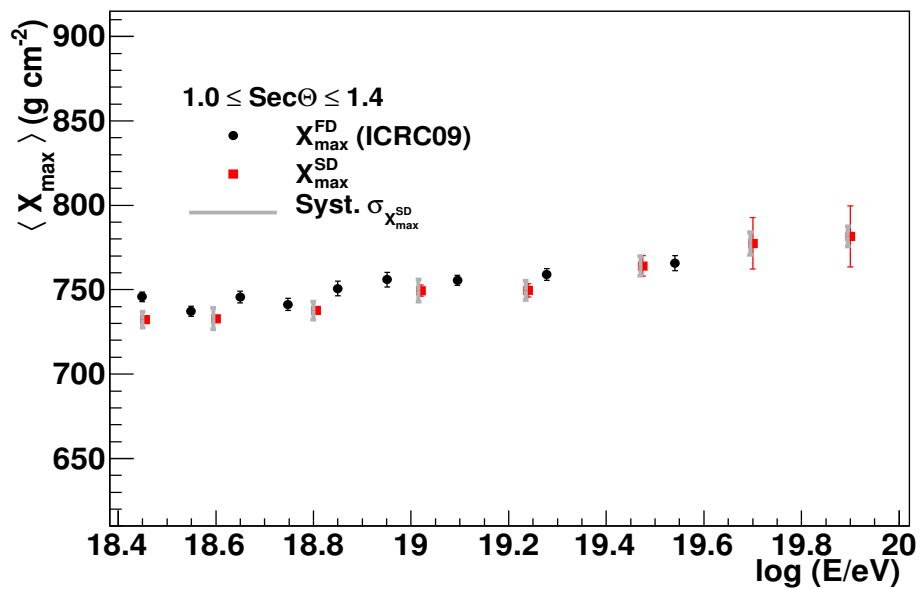


Figure 5.28: Comparison of the depth of the shower maximum obtained from FD and SD measurements showing the systematic errors introduced by the calibration procedure (1σ area). The notation \log refers to the decadic logarithm, \log_{10} .

Chapter 6

Estimation of the mass composition of ultra high energy cosmic rays using Δ_{1000}

The parameter Δ_{1000} has been used to estimate the depth of the shower maximum from measurements of the SD detector, X_{\max}^{SD} . In this chapter this method is used to determine the mass composition of Cosmic Rays using some of the techniques which include the treatment of X_{\max} . The rate of change of the mean X_{\max}^{SD} with the energy is compared with results obtained from FD measurements. This technique is also used with Monte Carlo SD data and compared with results from Monte Carlo FD data. The mean logarithmic mass calculation for estimating the mass composition, based on Monte Carlo data is also explored. Discussions about the Δ_{1000} parameter and depth of the shower maximum of some of the events which have been studied for finding correlations with AGNs by the Auger experiment are presented as well.

6.1 Determination of the mass composition of cosmic rays using the Elongation Rate, D_{10}

Comparison with simulated air showers The rate of change of $\langle X_{\max} \rangle$ with the energy is used for studying changes in the mass composition of cosmic rays as explained in Chapter 3. In Fig. 6.1 the mean depth of the shower maximum obtained from SD measurements using the method Δ_{1000} is compared with air shower simulations for different hadronic interaction models [173, 205–208]. The gray lines in every point correspond to the uncertainty introduced by the calibration of Δ_{1000} with X_{\max} . It can be seen that there are considerable differences for different hadronic interaction models. These differences are not totally exhaustive, since the hadronic interaction models do not cover the full range of possible extrapolations of low energy accelerator data. Nevertheless, assuming that the models provide a realistic description of hadronic interactions at ultra high energies, the comparison with SD data leads to conclude that the mass increases gradually with energy for $18.5 \geq \log(E/\text{eV})$ (log refers to the decadic logarithm, \log_{10}). As seen in Fig. 5.13, there is no systematic trend with zenith angle. The corresponding elongation rate is calculated above the energy at which the SD reaches the full

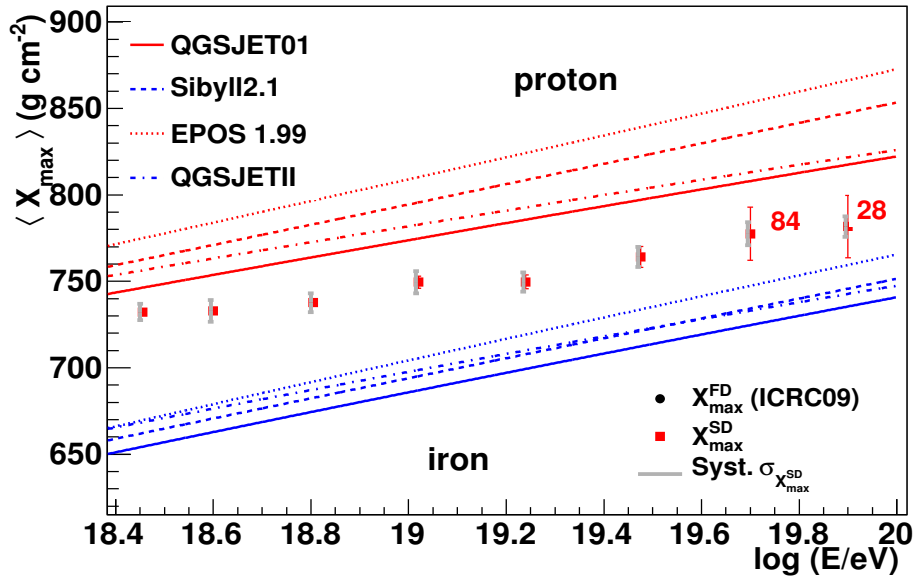


Figure 6.1: Comparison of the rate of change of $\langle X_{\max}^{\text{SD}} \rangle$ with the energy, with different hadronic interaction models. The numbers attached to the last two bins show the number of events at the given energy.

efficiency, $18.4 \approx \log(E/\text{eV})$, as mentioned in Chapter 2. Values of D_{10} for the whole sample and for three different ranges of zenith angle do agree within the uncertainties as shown in Fig. 6.2. For the whole sample, $D_{10} = 27 \pm 3 \text{ gcm}^{-2}\text{decade}^{-1}$, which is comparable with the values corresponding to the same range of energies for QGSJET01, Sibyll2.1, EPOS1.99 and QGSJET II models [209], as shown in table 6.1. Values of the models are calculated by averaging the predictions for pure iron and pure proton in each case. The values corresponding to pure composition are higher than the one from measurements, which can be interpreted as an increase of the average mass with energy.

		D_{10} ($\text{gcm}^{-2}\text{decade}^{-1}$)			
SD data	FD data	QGSJET01	Sibyll2.1	EPOS1.99	QGSJET II
27 ± 3	24 ± 3	52 ± 0.13	58 ± 0.01	62 ± 0.08	47 ± 0.2

Table 6.1: Values of the elongation rate for SD and FD data and for different models.

Comparison with FD measurements The mean depth of the shower maximum obtained from SD measurements, using the method Δ_{1000} , is compared with the latest FD measurements shown in Ref. [3], and with air shower simulations in Fig. 6.3. There is agreement between SD and FD measurements as shown before. The elongation rate of FD events for energies above $\log(E/\text{eV}) = 18.24$, according to Ref. [3] is $D_{10} = 24 \pm 3 \text{ gcm}^{-2}\text{decade}^{-1}$, which is quite close to the value obtained for SD measurements, of $D_{10} = 27 \pm 3 \text{ gcm}^{-2}$, for energies above $\log(E/\text{eV}) = 18.4$ calculated in the last paragraph.

6.1 Mass composition using the Elongation Rate, D_{10}

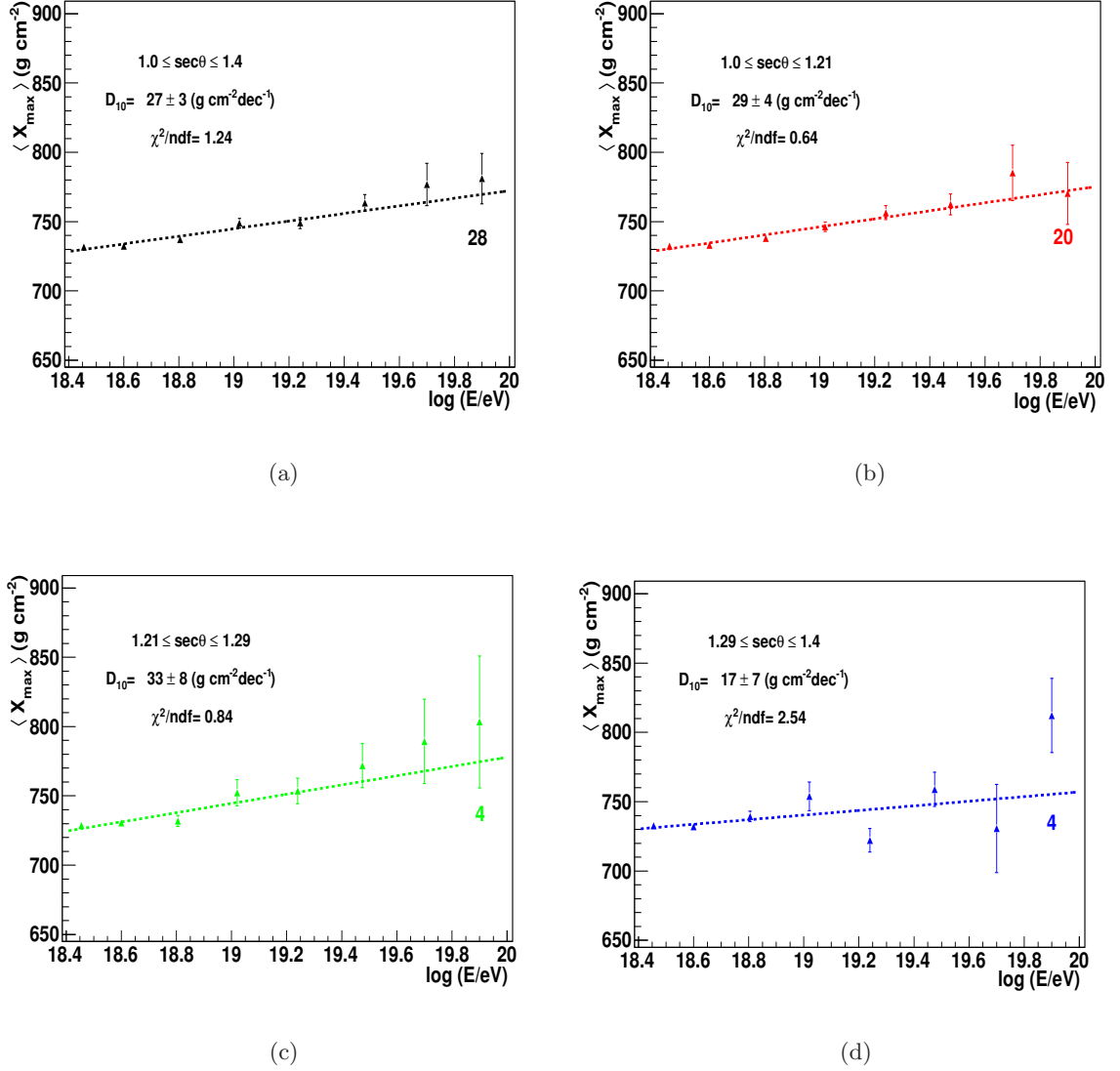


Figure 6.2: $\langle X_{\max}^{\text{SD}} \rangle$ as a function of the energy for three ranges of zenith angle. The corresponding elongation rate for energies above $\log(E/eV) = 18.4$ are shown.

The similar evolution with energy of both kind of measurements is supported by the fractional residuals shown in Fig. 5.14. The conclusion is, as mentioned before, that there is a gradual increase of the average mass of cosmic rays with the energy.

Nevertheless, no conclusions about the change of D_{10} below and above $\log(E/eV) = 18.24$ observed in FD, can be drawn because the SD detector is not fully efficient for those low energies and the corresponding extrapolation of the calibration may not be reliable.

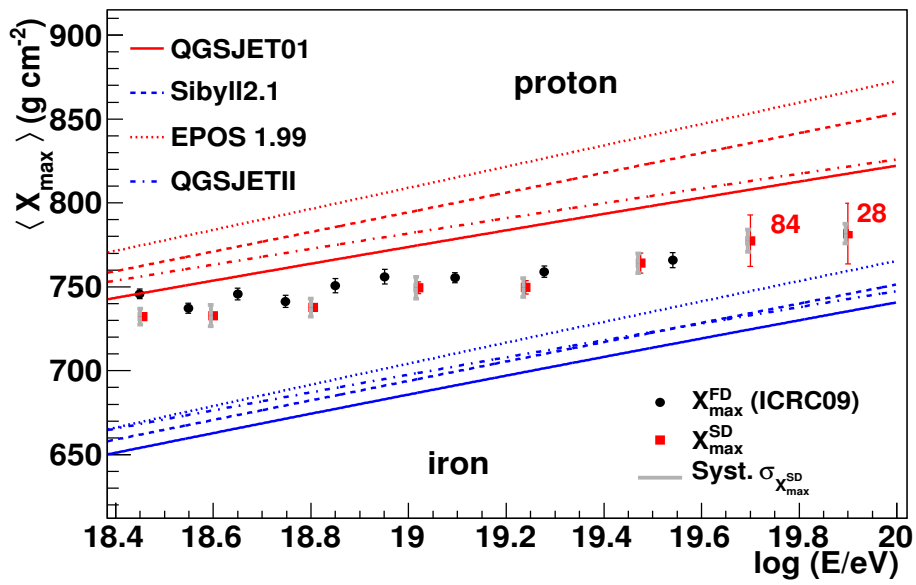


Figure 6.3: Comparison of the rate of change of $\langle X_{\max}^{\text{SD}} \rangle$ with $\langle X_{\max}^{\text{FD}} \rangle$ and with different hadronic interaction models, with energy.

6.2 A Monte Carlo Study of Δ_{1000}

Given that the X_{\max}^{SD} obtained with the method proposed in this work is comparable with FD results on average basis, the use of Monte Carlo air showers to cross-check its applicability is preserved after inaccuracies in the estimation of risetime (and thus, of Δ_{1000}) due to effects present in simulations as the shower thinning [210] and the lack of predicted muons in certain models [200,201]. Comparisons of calculated X_{\max}^{SD} with the X_{\max}^{MC} set in the simulated shower may give information about the accuracy of the method. Contributions to the systematic uncertainty due to the reconstruction procedure of the shower can be also estimated.

The Monte Carlo framework used for this study is CORSIKA (COsmic Ray SIMulations for KAscade, version 6735) [194,195]. It is a four-dimensional particle transport code that handles interactions and decays of particles in the atmosphere. Proton and iron were considered as primary particles, generated with fixed zenith angles and fixed energies as shown in Appendix B. The number of available showers after application of the required cuts for calculation of Δ_{1000} is shown in tables 6.2 and 6.3. The description of hadronic interactions

Primary	Energy (eV)						
	No.Ev	$1 \cdot 10^{18}$	$3.16 \cdot 10^{18}$	$1 \cdot 10^{19}$	$3.16 \cdot 10^{19}$	$1 \cdot 10^{20}$	$3.16 \cdot 10^{20}$
SD							
proton	4003	70	325	2773	230	383	222
iron	4156	106	397	2796	235	402	220
Hybrids (out of SD)							
proton	2383	3	99	1739	146	242	154
iron	2495	1	104	1816	162	257	155

Table 6.2: Number of available simulated air showers after application of cuts required for Δ_{1000} calculation according to the energy.

Primary	$\sec \theta$							
	1.	1.1	1.26	1.3	1.4	1.5	1.7	1.9
SD								
proton	132	241	279	265	2368	261	242	215
iron	168	275	282	297	2368	271	258	237
Hybrids (out of SD)								
proton	0	0	160	163	1558	186	175	141
iron	0	0	164	175	1626	181	175	174

Table 6.3: Number of available simulated air showers after application of cuts required for Δ_{1000} calculation according to the zenith angle.

is divided in two parts, low and high energetic hadron interactions with a transition energy of 200 GeV. The high energy hadronic simulations are simulated with the QGSJET II

model [206, 211] and at low energies the FLUKA model [212] is used. The electromagnetic component is described by EGS4 [213] implemented in CORSIKA. The detector simulation is included in the Offline framework as it is for data reconstruction [214]. The FD part of the simulation is obtained from ray-tracing of generated photons through the telescope optics to the camera response to generate a trigger. The background light is calculated from the recorded variance of the ADC traces after subtracting the electronic noise [215]. The SD part is done using the GEANT4 [196, 197] software package, which provides an abundant set of physics processes to handle interactions of particles with matter across a wide energy range.

Systematics from measurement Before using simulations to verify the method on average basis, it is still necessary to explore how the uncertainties due to the measurement are reproduced in Monte Carlo air showers. Four benchmarks for calculating Δ_{1000} , according to the fixed energies given for the Monte Carlo procedure are used. As discussed in Chapter 5, the measurement uncertainty is given by $\sigma_{\Delta_{1000}}$. The contributions to this quantity are coming from $\sigma_{\Delta_{1000}}^{t_{1/2}}$, $\sigma_{\Delta_{1000}}^{\text{rec}}$ and $\sigma_{\Delta_{1000}}^{\text{int}}$, random fluctuations introduced from uncertainties in the measurements of $t_{1/2}$ and $t_{1/2}^{\text{BM}}(r, \theta, E)$, random deviations introduced from uncertainties in the reconstruction procedure and intrinsic fluctuations in the shower development, respectively. In order to cross-check the fraction of each contribution, these are calculated using simulated iron and proton showers. The contributions are in good agreement with the values obtained from measurements as shown in Fig. 6.4 and in the Table 6.4. The contribution coming from the measurement of risetime and from the reconstruction procedure are dominating.

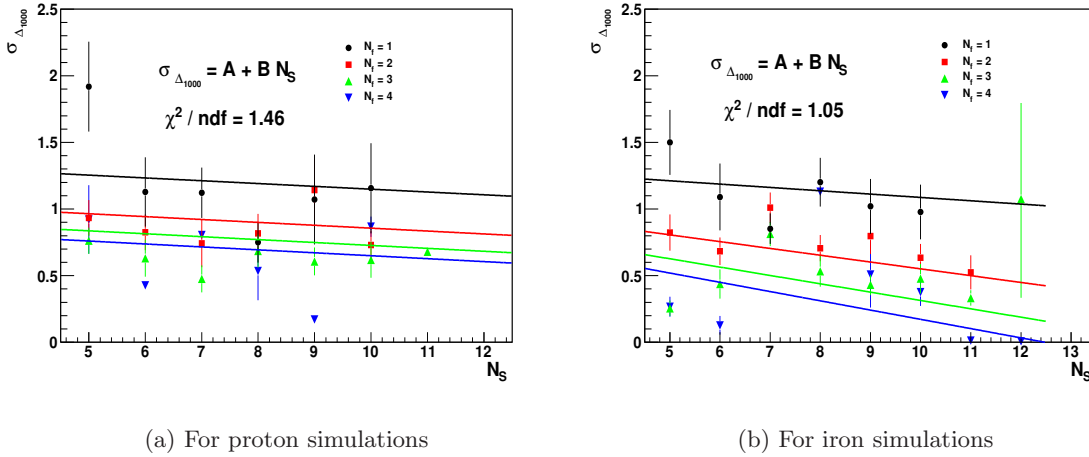
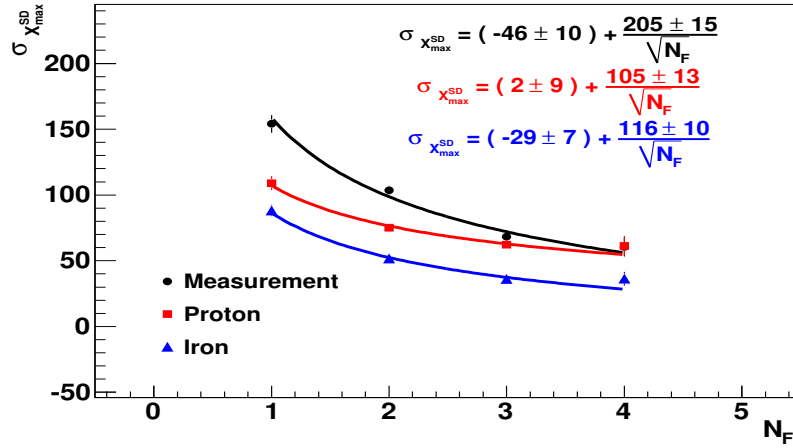


Figure 6.4: $\sigma_{\Delta_{1000}}$ as a function of N_s for simulated showers.

A cross-check with simulations is also done for the fluctuations $\sigma_{X_{\text{max}}^{\text{SD}}}$. Figure 6.5 shows that fluctuations in proton showers are decreasing from $\sim 110 \text{ gcm}^{-2}$ to $\sim 60 \text{ gcm}^{-2}$. In the case of iron showers, fluctuations are in the range from $\sim 90 \text{ gcm}^{-2}$ to $\sim 40 \text{ gcm}^{-2}$, lower than for proton and measured showers, which reflects the difference in the fluctuations introduced in simulations by the superposition model (See Chapter 3). It leads to expect less fluctuations of Δ_{1000} for the case of iron.

	$\sigma_{\Delta_{1000}}^{\text{int}}$		$\sigma_{\Delta_{1000}}^{\text{rec}}$		$\sigma_{\Delta_{1000}}^{t_{1/2}}$	
	Cont.	Frac.	Cont.	Frac.	Cont.	Frac.
Measurements	0.48	10.4%	0.995	44.6%	1	45%
proton	0.38	9%	0.73	32%	1	59%
iron	0.4	10%	0.66	27%	1	63%

 Table 6.4: Estimated contribution to the uncertainty in Δ_{1000} from the three considered sources.

 Figure 6.5: Uncertainties of $X_{\text{max}}^{\text{SD}}$ for data with energies between $\log(E/eV) = 18.5$ and $\log(E/eV) = 19.6$, and $1.0 \leq \sec\theta \leq 1.4$, arising from measurement of Δ_{1000} , compared with the fluctuations obtained from simulated events.

Use of Monte Carlo Simulations for estimating systematic errors Values for Δ_{1000} for simulations of proton and iron showers were obtained. The four benchmarks were calculated according to the Monte Carlo energy scale, $BM(E_{\text{MC}})$. The corresponding $X_{\text{max}}^{\text{SD}}$ was calculated following the same procedure as for measurements, for showers having energies above $\log(E/eV) = 18.5$. Figure 6.6 shows the lines obtained for $X_{\text{max}}^{\text{SD}}$, the lines are fitted to five mean values of $X_{\text{max}}^{\text{SD}}$ corresponding to each one of five energy ranges (for proton $\chi^2/ndf = 1.15$ and for iron $\chi^2/ndf = 3.4$). The comparison with the lines of QGSJET II shows that results of both masses are close to the model prediction. In the case of proton, the difference with the model is up to $\sim 20 \text{ gcm}^{-2}$. In the case of iron, the line is having almost the same behavior as the model. For testing the self-consistency of the method, the benchmarks corresponding to iron and proton are interchanged and the calibration for proton and iron showers is applied to the other sample of mass respectively. The behavior of the obtained lines (for proton $\chi^2/ndf = 3.4$ and for iron $\chi^2/ndf = 2.15$) is again similar to the one of the model in both cases but an offset of around 10 gcm^{-2} is observed.

The corresponding relative errors, calculated event-by-event with respect to the MC value of X_{max} , $X_{\text{max}}^{\text{MC}}$ are shown in figure 6.7. Errors are around 3% for the proton sample and for the iron one the errors are less than 2%. It means that the average X_{max} can be described with an error of $\sim 3.6\%$ (adding the errors in quadrature) by using the Δ_{1000} method. For

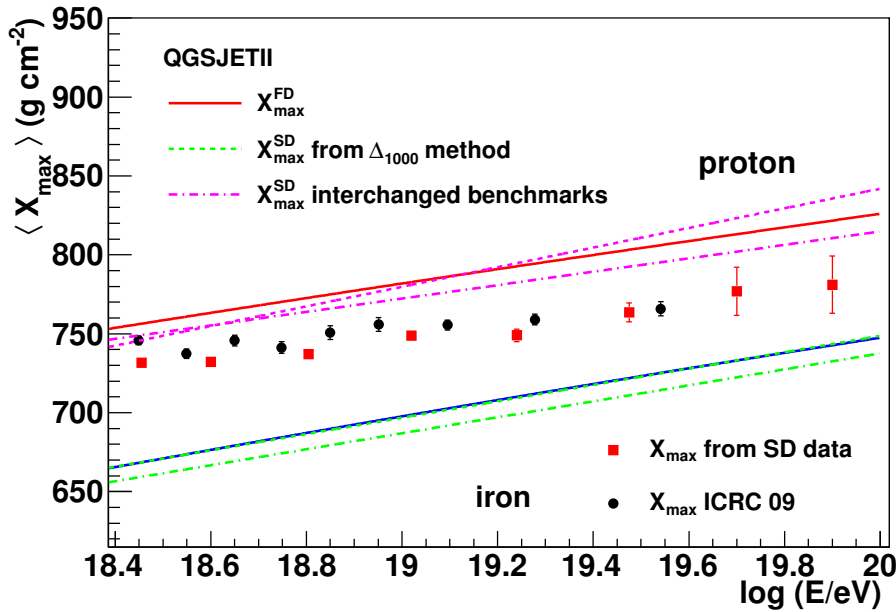
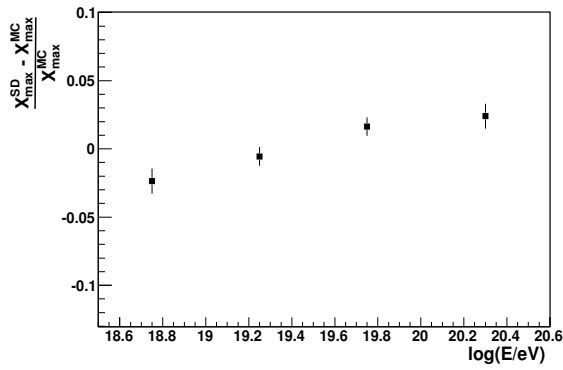


Figure 6.6: Comparison of X_{\max}^{SD} obtained from simulated showers with X_{\max}^{FD} from the QGSJET II model as a function of the Monte Carlo Energy.

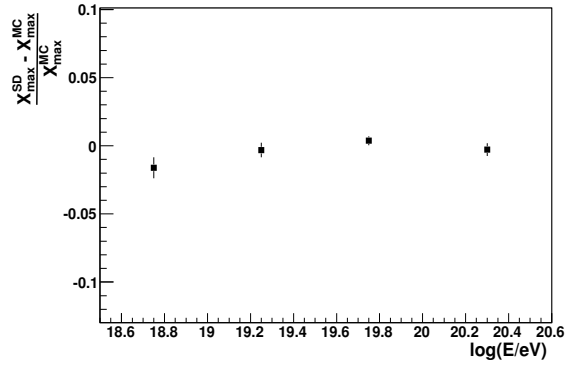
the values obtained by interchanging the benchmarks, values are up to 3% for energies above $\log(E/eV) = 19$ and up to 6% for lower energies for the proton sample. For the iron sample, errors are up to 6% for energies above $\log(E/eV) = 19$ and around 2% for lower energies. These values show that both kind of masses can be described by any of the both calibrations with an error of $\sim 6\%$, regarding the right use of the benchmarks, demonstrating the self-consistency of the method.

Since the estimation of errors in X_{\max}^{SD} is done by using the Monte Carlo energy, E_{MC} , as well as in the calculation of the benchmarks, systematics introduced by the SD energy calibration are not taken into account. Thus, the main sources of uncertainty left and described by this estimation are those corresponding to the reconstruction procedure, the calculation of risetime and its uncertainty, the calculation of Δ_{1000} and the intrinsic shower fluctuations, as well as the uncertainties from the calibration procedure of Δ_{1000} with X_{\max}^{FD} . The estimation of the uncertainty from these sources is found to be $\sim 3.6\%$, regarding the assumption that the model provides a realistic description of hadronic interactions at ultra high energies.

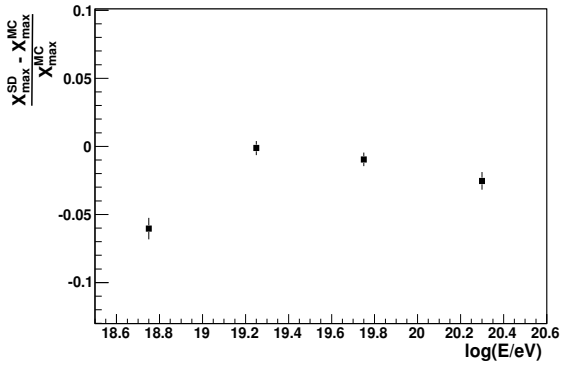
The shower to shower fluctuations, $RMS(X_{\max}^{SD})$, can be calculated for iron and proton showers and compared with the results obtained from measurements. Fluctuations related to the reconstruction procedure as well as those related to the calibration of Δ_{1000} with X_{\max}^{FD} and the resolution of the detector, are present in both kind of samples. The measurements are close to the proton sample according to Fig. 6.8(a) but no conclusion can be drawn since fluctuations in measurements still need to be properly understood as discussed in Section 5.4. Studies about how this fluctuations are reproduced in simulations are also necessary. Nevertheless, the difference between proton and iron showers is around $40\ g\ cm^{-2}$, which can be observed in Fig. 6.8(b) from a linear fit to the points shown in Fig. 6.8(a). This difference is comparable



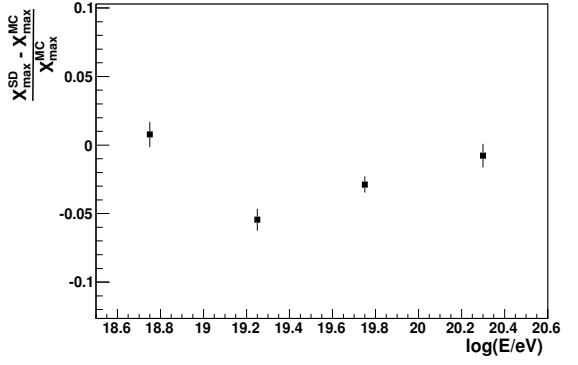
(a) proton showers



(b) iron showers



(c) proton showers, iron benchmarks

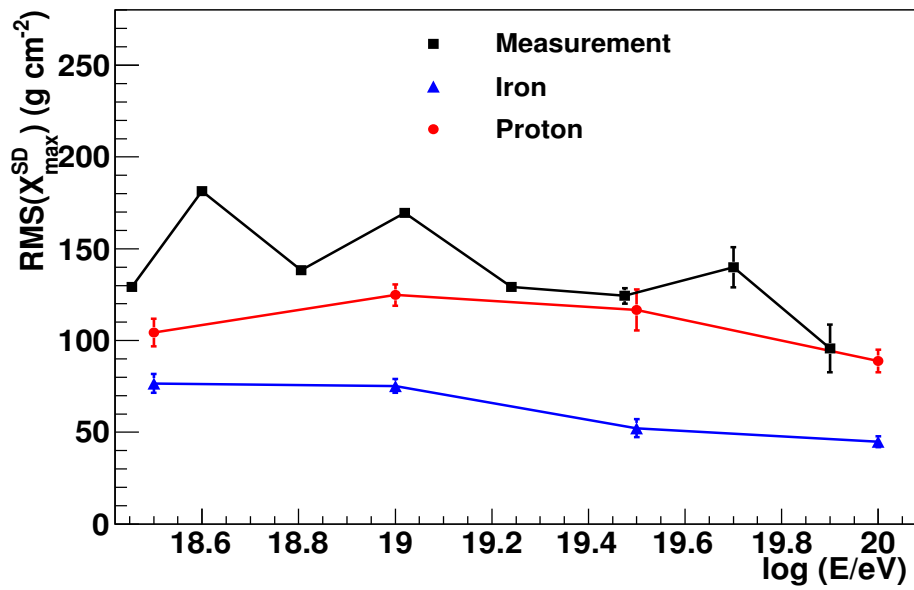


(d) iron showers, proton benchmarks

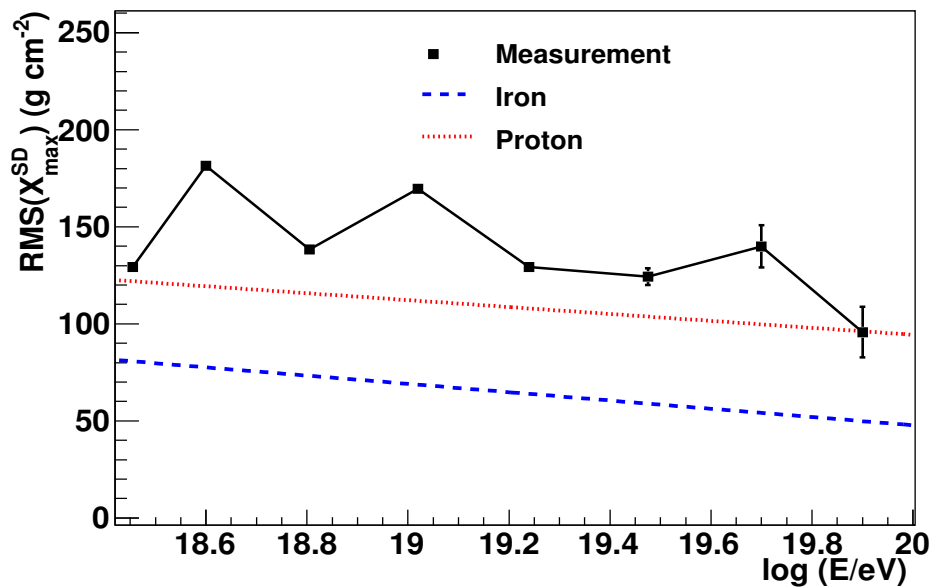
Figure 6.7: Relative error of X_{\max}^{SD} with respect to X_{\max}^{MC} as a function of $\log(E_{\text{MC}})$.

with the one founded for $\text{RMS}(X_{\max}^{\text{FD}})$ shown in Fig. 3.3.

The Δ_{1000} method has been tested with Monte Carlo showers, its robustness to reproduce X_{\max} on average basis has been proved leading to the same conclusion obtained from comparisons with X_{\max}^{FD} , namely a gradual increase of the mass with the energy. However, the fluctuations obtained from simulations do not provide reliable information to draw any conclusion about the mass composition of the measured showers yet since fluctuations in measurements still need to be studied.



(a) Comparison of the mean value per energy range.



(b) Comparison with a linear fit to the points.

Figure 6.8: Comparison of shower to shower fluctuations for X_{\max}^{SD} from simulations and measurements.

6.3 Determination of the mass composition of cosmic rays using the mean logarithmic mass, $\langle \ln A \rangle$

As described in Section 1.6, the mean logarithmic mass is proportional to the average depth of the shower maximum of protons and iron nuclei, and to the measured one with the relation

$$\langle \ln A \rangle = \ln A_{\text{Fe}} \cdot \frac{X_{\text{max}}^{\text{meas}} - X_{\text{max}}^p}{X_{\text{max}}^{\text{Fe}} - X_{\text{max}}^p}. \quad (6.1)$$

Using the $X_{\text{max}}^{\text{SD}}$ obtained from the Δ_{1000} method applied to measurements and the corresponding values of $X_{\text{max}}^{\text{Fe}}$ and X_{max}^p from different hadronic interaction models, several estimations of the mean logarithmic mass can be done.

Figure 6.9 shows $\langle \ln A \rangle$ of the SD data displayed in Fig. 6.1 with reference to three hadronic interaction models. The linear fits show that the estimated values of the mass are increasing at a constant rate of $\frac{d \ln A}{d \log E} = 1.24 \pm 0.15 \text{ decade}^{-1}$, $\frac{d \ln A}{d \log E} = 0.89 \pm 0.19 \text{ decade}^{-1}$ and $\frac{d \ln A}{d \log E} = 1.12 \pm 0.16 \text{ decade}^{-1}$ when the EPOS, QGSJET II and SIBYLL models are used respectively. The absolute values of the logarithmic mass are intermediate between protons ($\ln A = 0$) and iron ($\ln A \simeq 4$). A comparison of this values with hybrid events is shown in Appendix C. Applying the Δ_{1000} method it is possible to obtain values for X_{max}^p and

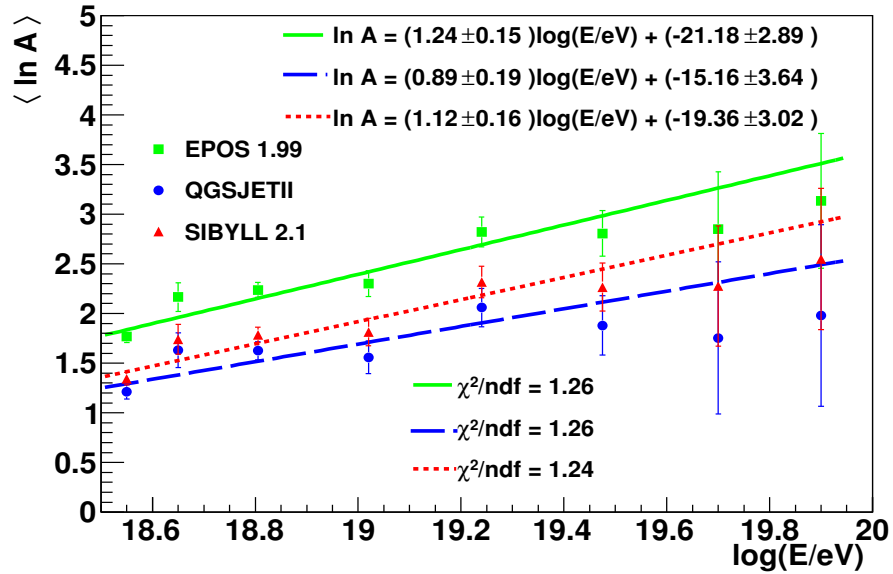


Figure 6.9: The mean logarithmic mass of UHECR measured with the SD detector, using the $X_{\text{max}}^{\text{SD}}$ parameter with reference to three different hadronic interaction models.

$X_{\text{max}}^{\text{Fe}}$ as shown in Section 6.2. The values obtained for the QGSJET II model (Fig. 6.6) are used for estimating the mean logarithmic mass for the SD sample. A comparison with the results obtained from three choices for X_{max}^p and $X_{\text{max}}^{\text{Fe}}$ is shown in Fig. 6.10. The reference X_{max}^p and $X_{\text{max}}^{\text{Fe}}$ is either taken from the model itself or from the reconstructed $X_{\text{max}}^{\text{SD}}$ for pure proton and iron simulation. The third option is given by the interchanged benchmarks. The mass increases in all three cases. The increase in the case of interchanged benchmarks

$(\frac{d \ln A}{d \log E} = 0.71 \pm 0.19 \text{ decade}^{-1})$ is similar to the one presented for the model itself. In the case of the results obtained with reference to the Δ_{1000} method, the increase is faster ($\frac{d \ln A}{d \log E} = 1.35 \pm 0.19 \text{ decade}^{-1}$). The apparent difference in $\langle \ln A \rangle$ for the three cases are an estimate of the systematic uncertainty of the whole calibration procedure.

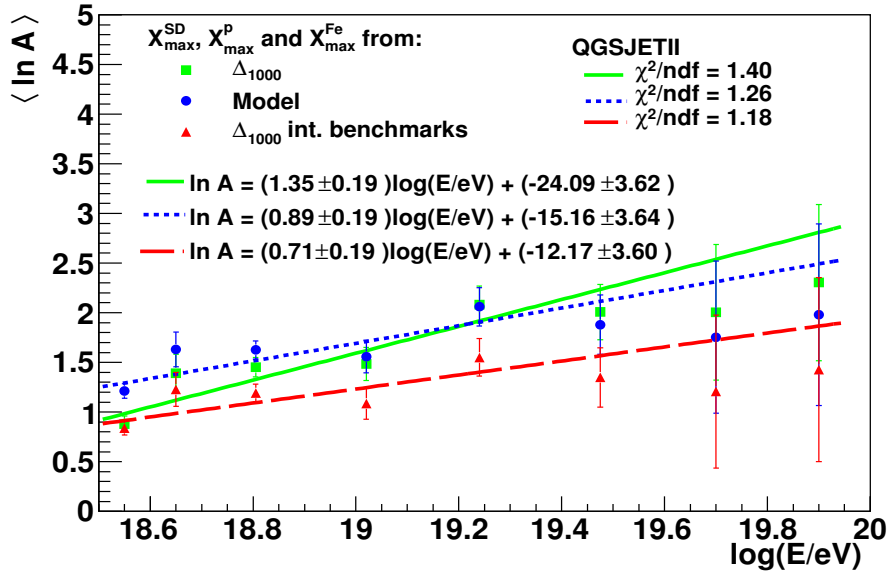


Figure 6.10: The mean logarithmic mass based on X_{\max}^{SD} parameter with reference to the QGSJET II hadronic model and with reference to the values obtained applying the Δ_{1000} method to Monte Carlo air showers (lines shown in Fig. 6.6).

6.4 Analysis on AGN correlated events

The Pierre Auger Collaboration has reported a correlation between the arrival direction of cosmic rays with energies above 57 EeV and the position of active galactic nuclei (AGNs) lying within ~ 75 Mpc. This result demonstrates the anisotropy of the arrival directions of the highest energy cosmic rays and their extragalactic origin. The most of the cosmic rays reaching Earth in that energy range are, thus, protons from nearby astrophysical sources [4]. Figure 6.11 shows an Aitoff projection of the celestial sphere in galactic coordinates with circles of radius 3.1° centered at the arrival directions of the 27 cosmic rays with highest energy explored. The positions of the 472 AGN within ~ 75 Mpc derived from the 12th edition of the Veron-Cetty catalog are indicated by red asterisks. The dashed line is the super-galactic plane. The shading indicates the relative exposure of the sky to the Auger Observatory.

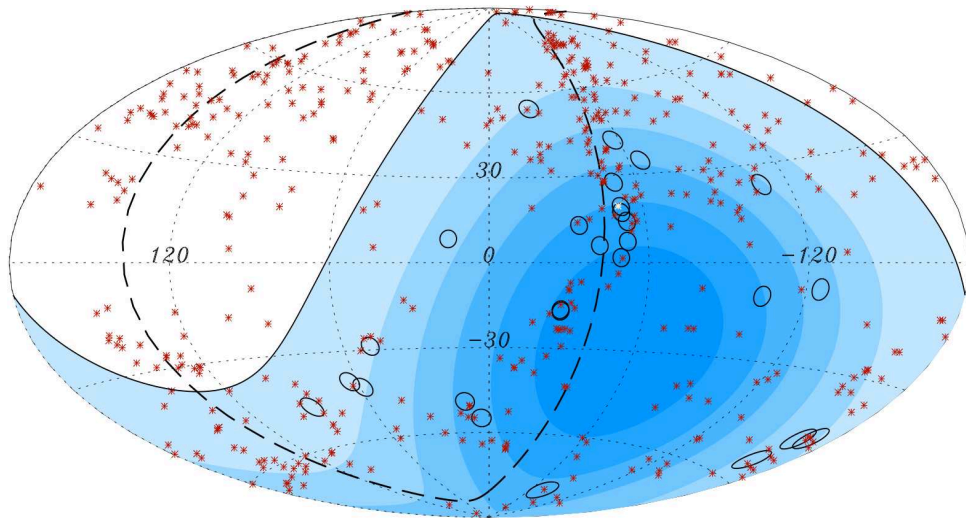


Figure 6.11: Aitoff projection of the 27 events with energy above ~ 57 EeV used in the search for correlation with AGN by the Auger Collaboration [4].

Studies on X_{\max} show, however, an increase of the mass with the energy, as it was also observed from the estimations of X_{\max}^{SD} . This would indicate the intervention of magnetic fields much weaker than current estimates, or that the magnetic fields may be structured in such a way as to preserve correlation with the distribution of nearby matter even if the observed arrival directions are far from the positions of the actual sources. Further measurements of the anisotropy of the arrival directions of UHECRs, complemented with studies on mass composition should provide more information about the nature of their sites of acceleration, as well as about properties of galactic and intergalactic magnetic fields. With this motivation, the Δ_{1000} is used to obtain information on the primary mass of the AGN events.

A sample of events detected until March 2009, which has been used by the Auger Collaboration for updating the studies on the correlation of the highest energy cosmic rays with nearby extragalactic matter are explored. Only 39 of those events fulfill the conditions for obtaining Δ_{1000} .

The values of X_{\max}^{SD} are shown in Fig. 6.12 as a function of the energy in comparison with the models QGSJET01, SIBYLL 2.1, EPOS 1.99 and QGSJETII. The uncertainties of the points

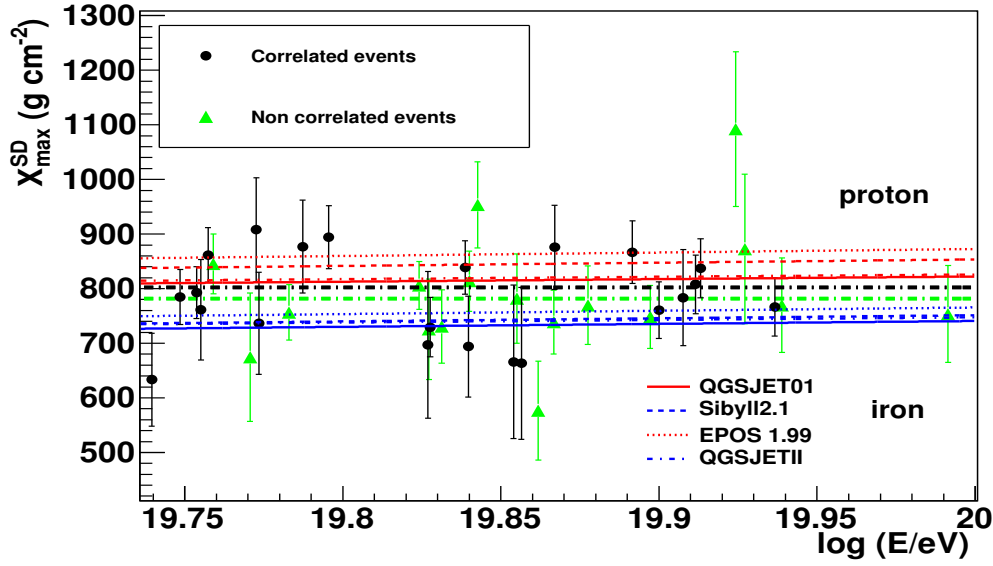
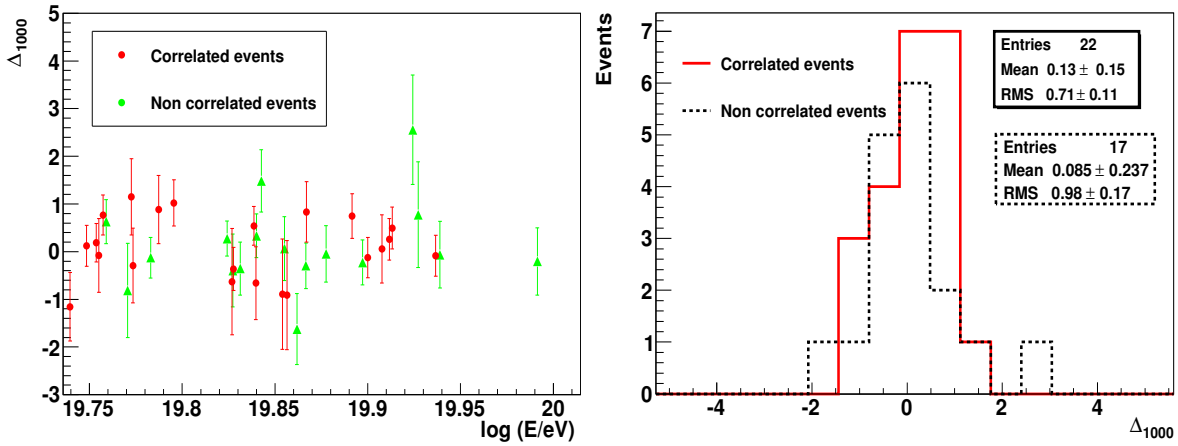


Figure 6.12: X_{\max}^{SD} of the 39 high energy cosmic rays explored by the Pierre Auger Collaboration for studies on correlation with nearby extragalactic matter, the errors are too large to draw a firm conclusion on an event-by-event basis.



(a) Δ_{1000} individual values.

(b) Δ_{1000} distributions.

Figure 6.13: Comparisons of Δ_{1000} values for correlated and non correlated events.

are those obtained from the calibration of Δ_{1000} with X_{\max}^{FD} . The black and green dashed lines show the average value for correlated ($802 \pm 14 \text{ g cm}^{-2}$) and non correlated ($782 \pm 17 \text{ g cm}^{-2}$) events respectively. The difference is not large and is within the errors, moreover, the calculation of the corresponding X_{\max}^{SD} is conservative since the uncertainties are such that it is not possible to draw a firm conclusion on an event-by-event analysis.

Furthermore, there are no significant differences between the Δ_{1000} values of both samples as observed in Fig. 6.13(a). But the corresponding Δ_{1000} distributions may give more information

about the difference with respect to the mass composition of the events. As shown in Fig. 6.13(b), the spread of the correlated events is slightly smaller than that for the non correlated ones, but the difference in the estimated RMS values is only 1.6σ . Thus, it can be concluded that there is no significant difference between both samples of events.

Summary and Conclusions

In the present work, the mass composition of Ultra High Energy Cosmic Ray has been investigated. The capacity of the Pierre Auger Observatory as hybrid detector has provided the opportunity to define a mass-sensitive parameter based on the time traces of the surface detector and at the same time, the possibility of calibrating it with the depth of the shower maximum measured by the fluorescence detector. The estimations of the mass composition derived from the elongation rate, as obtained from the surface detector data, offer results supported by high statistics. The results are in good agreement with the ones obtained from the fluorescence detector, concluding a gradual increase of the average mass of cosmic rays with the energy. The main procedures performed to achieve that result are described in the following paragraphs.

Treatment of risetime The risetime, $t_{1/2}$, is the feature of the time trace from which the new mass-sensitive observable is defined. For obtaining a well described risetime, some treatments were needed.

- Definition and parameterisation of the risetime uncertainty, $\sigma_{t_{1/2}}$, based on the characteristics of the surface detector and data treatment. The parameterisation has at most a 7% error with respect to the value obtained from the data. The result was confirmed with Monte Carlo showers validating the use of the parameterisation for simulations.
- Correction of the azimuthal asymmetry observed in $t_{1/2}$ with a bias of less than 5% for distances between 600 m and 1800 m from the shower core and less than $\sim 12\%$ for larger distances.
- Parameterisation of risetime as a function of the distance from the shower core, taking into account the existing dependence of $t_{1/2}$ on the zenith angle and on the energy of the shower. An average parameterisation was obtained for all valid points of all events, giving reasonable initial values when performing individual fits, even if a standard event-by-event one can not be performed ensuring the increase of statistics.
- Studies on the parameter $t_{1/2}(1000\text{ m})$ as mass composition sensitive parameter. No clear dependency on the energy is observed, a bias with respect to the zenith angle for inclined showers is observed and comparisons with Monte Carlo showers are not reliable. This leads to conclude that $t_{1/2}(1000\text{ m})$ is not a suitable mass composition sensitive observable, when Monte Carlo Data are used as reference.

Definition and treatment of the parameter Δ_{1000} The parameter Δ_{1000} is proposed as an alternative for exploiting the mass sensitivity of the risetime of FADC traces, since the direct use of $t_{1/2}$ parameter has been demonstrated to be limited. A method for finding its correlation with X_{\max} has been developed.

- The observable Δ_{1000} measures the difference of $t_{1/2}$ at 1000 m between two fits to the risetime as a function of the distance from the shower core, normalized to the measurement uncertainty, $\sigma_{t_{1/2}}$. The parameter does not present a bias until $\sec \theta = 1.4$ and for energies between $\log(E/\text{eV}) = 18.4$ and $\log(E/\text{eV}) = 19.6$.
- A calibration of Δ_{1000} with X_{\max} considering the data set used for the latest results on X_{\max} presented by the Pierre Auger Collaboration is performed. The fit does not show any bias with respect to the energy (energies between $\log(E/\text{eV}) = 18.5$ and $\log(E/\text{eV}) = 19.6$) and zenith angle ($1.0 \leq \sec \theta \leq 1.4$).
- The parameter X_{\max}^{SD} , obtained from the calibration is compared with the estimation of X_{\max} obtained from measurements of the fluorescence detector for energies above $\log(E/\text{eV}) = 18.4$. Both observables agree well on average. The parameter X_{\max}^{SD} does not present any systematic trend with the zenith angle. The X_{\max} fluctuations $\text{RMS}(X_{\max}^{\text{SD}})$ and $\text{RMS}(X_{\max})$ are, nevertheless not comparable. Corrections with respect to effects of the event selection, measurement uncertainties and detector resolution have still to be taken into account.
- The uncertainties of the parameter X_{\max}^{SD} come from several sources, being the mean contributions due to the measurement and treatment of $t_{1/2}$ and to the reconstruction procedure according to studies with fluctuations of Δ_{1000} .
- The resolution of SD measurements as estimated from fluctuations of Δ_{1000} gives a minimum value of $\sim 60 \text{ gcm}^{-2}$ and a mean value of $\sim 100 \text{ gcm}^{-2}$, which are large compared with $\sim 20 \text{ gcm}^{-2}$ corresponding to FD measurements. The measurement uncertainty in X_{\max}^{SD} is too large to be used in composition measurements on an event-by-event basis.
- Studies about fluctuations of the parameter Δ_{1000} related to the event selection are needed. For instance, the conditions for selecting adequate $t_{1/2}$ values have to be improved. That may allow to deduce more accurately the resolution of the SD detector and thus, to correct for $\text{RMS}(X_{\max}^{\text{SD}})$. An improvement of the calibration obtained by using the Δ_{1000} method and of estimations about systematic uncertainties are also expected.

Mass composition using X_{\max}^{SD} The main goal of this work, estimations of the mass composition supported by high statistics, can be performed using the Δ_{1000} method.

- Results using the elongation rate, D_{10} , point to a gradual increase of the average mass of cosmic rays with the energy. The value obtained from SD measurements for energies above $\log(E/\text{eV}) = 18.4$ is $D_{10} = 27 \pm 3 \text{ gcm}^{-2}$ which is similar to the one obtained from FD measurements $D_{10} = 24 \pm 3 \text{ gcm}^{-2} \text{ decade}^{-1}$.

- Using the Δ_{1000} method it is possible to reproduce the $\langle X_{\max} \rangle$ value provided by Monte Carlo simulations with an error of $\sim 3.6\%$. The self-consistency of the method on average was also demonstrated.
- A gradual increase of the mean logarithmic mass, $\langle \ln A \rangle$, with the energy is also found by using several hadronic interaction models and X_{\max}^{SD} .
- No significant difference in mass composition of the highest energy events which were analyzed for anisotropy studies by the Pierre Auger Collaboration, by using the Δ_{1000} method was found. Both, correlating and non-correlating events have a similar Δ_{1000} within statistical uncertainties.
- The Δ_{1000} method allows to obtain results on X_{\max} from SD measurements with 15 times more events than those obtained from FD measurements for energies above $10^{19.4}$ eV.
- The energy range of measurements for X_{\max} of the Pierre Auger Observatory has been extended to $10^{19.9}$ eV i.e. by a factor of 2.3 with respect to the one reached with FD analysis, which is of about $10^{19.5}$ eV.
- The data of the Pierre Auger Observatory suggest that for energies above $10^{19.6}$ eV the average mass is getting heavier with energy but it still remains in a mixed mass composition.

Bibliography

- [1] *Information* , <http://www-bdnew.fnal.gov/tevatron>.
- [2] *Information* , <http://lhc.web.cern.ch>.
- [3] J. ABRAHAM et al., (2010), astro-ph.HE/arXiv:1002.0699.
- [4] J. ABRAHAM et al., *Science* **318**, 939 (2007), arXiv:0711.2256 [astro-ph].
- [5] T. STANEV, “*High Energy Cosmic Rays*“, Springer, 2004.
- [6] R. CLAY and B. DAWSON, “*Cosmic Bullets. High Energy Particles in Astrophysics*“, Helix Books. Perseus., 1997.
- [7] A. M. ROCHA, “*El discreto encanto de las partículas elementales*“, volume 68, Fondo de Cultura Económica, 1996.
- [8] J. OTAOLA and J. V. GALICIA, “*Los rayos cósmicos: mensajeros de las estrellas*“, volume 108, Fondo de Cultura Económica, 1995.
- [9] V. HESS, *Z. Phys.* **13**, 1084 (1912).
- [10] R. A. MILLIKAN, *Phys. Rev.* **22**, 198 (1922).
- [11] D. SKOBEŁTZYN, *Z. Phys.* **43**, 354 (1927).
- [12] A.H. COMPTON AND L. ÁLVAREZ, *Phys. Rev.* **43**, 835 (1933).
- [13] J. CLAY, *Proc. Amsterdam* **30**, 1115 (1927).
- [14] P. AUGER AND P. EHRENFEST AND R. MAZE AND J. DAUDIN & R. A. FRÉON, *Rev. Mod. Phys.* **11**, 288 (1939).
- [15] CLARK ET. AL., *Phys. Rev.* **122**, 637 (1961).
- [16] J. LINSLEY, *Proc. 19th Int. Cosmic Ray Conf., San Diego, California* **9** (1985).
- [17] K. GREISEN, *Phys. Rev. Lett.* **16**, 748 (1966).
- [18] G. ZATSEPIN and V. KUZ’MIN, *Sov. Phys. JETP Lett.* **4**, 78 (1966).
- [19] T. ABU-ZAYYAD et al., Prepared for 26th International Cosmic Ray Conference (ICRC 99), Salt Lake City, Utah, 17-25 Aug 1999.
- [20] J. ABRAHAM et al., *Nucl. Instrum. Meth.* **A523**, 50 (2004).
- [21] F. SCHÜSSLER, private communication.
- [22] G. KULIKOV and G. KRISTIANSEN, *Sov. Phys. JETP* **35**, 441 (1959).
- [23] A. D. ERLYKIN and A. W. WOLFENDALE, *J. Phys.* **G23**, 979 (1997).
- [24] A. D. ERLYKIN and A. W. WOLFENDALE, *Astropart. Phys.* **18**, 151 (2002).

- [25] R. NAM, S. NIKOLSKY, V. PAVLUCHENKO, A. CHUBENKO, and V. YAKOVLEV, *Proc. 14th Int. Cosmic Ray Conf, Munich* , 2258 (1975).
- [26] V. PTUSKIN and V. ZIRAKASHVILI, *A&A* , 755 (2005).
- [27] J. CANDIA, E. ROULET, and L. N. EPELE, *JHEP* **12**, 033 (2002).
- [28] T. ANTONI et al., *Astropart. Phys.* **24**, 1 (2005).
- [29] T. ABU-ZAYYAD et al., *Astrophys. J.* **557**, 686 (2001), astro-ph/0010652.
- [30] D. BIRD et al., *Astrophys. J.* **424**, 491 (1994).
- [31] V. P. EGOROVA et al., *Nucl. Phys. Proc. Suppl.* **136**, 3 (2004).
- [32] M. NAGANO et al., *J. Phys.* **G18**, 423 (1992).
- [33] T. K. GAISSER, Prepared for 28th International Cosmic Ray Conferences (ICRC 2003), Tsukuba, Japan, 31 Jul - 7 Aug 2003.
- [34] D. BIRD et al., *Phys. Rev. Lett.* **71**, 3401 (1993).
- [35] A. HILLAS, *Conf. on Cosmology, Galaxy Formation and Astro-Particle Physics on the Pathway to the SKA, Oxford, England* (2006), astro-ph/0607109.
- [36] D. DE MARCO and T. STANEV, *Phys. Rev.* **D72**, 081301 (2005).
- [37] T. WIBIG and A. W. WOLFENDALE, *J. Phys.* **G31**, 255 (2005).
- [38] D. ALLARD, E. PARIZOT, and A. OLINTO, *Astropart. Phys.* **27**, 61 (2007), astro-ph/0512345.
- [39] D. ALLARD, A. OLINTO, and E. PARIZOT, *submitted to Astron. Astrophys.* (2007), astro-ph/0703633.
- [40] V. BEREZINSKY, *Proc. 30th Int. Cosmic Ray Conf., Merida, Mexico* (2007), arXiv:0710.2750 [astro-ph].
- [41] V. BEREZINSKY, S. GRIGOREVA, and B. HNATYK, *Nucl. Phys. (Proc. Suppl.)* **151**, 497 (2006).
- [42] T. ABU-ZAYYAD et al., *Astropart. Phys.* **23**, 157 (2005), astro-ph/0208301.
- [43] M. TAKEDA et al., *Phys. Rev. Lett.* **81**, 1163 (1998), astro-ph/9807193.
- [44] R. ABBASI et al., *submitted to Phys. Rev. Lett.* (2007), astro-ph/0703099.
- [45] T. YAMAMOTO FOR THE PIERRE AUGER COLLABORATION, *Proc. 30th Int. Cosmic Ray Conf., Merida, Mexico* (2007), arXiv:0707.2638 [astro-ph].
- [46] T. STANEV, R. ENGEL, A. MÜCKE, R. PROTHEROE, and J. RACHEN, *Phys. Rev.* **D62**, 093005 (2000), astro-ph/0003484.
- [47] A. R. BELL, *Mon. Not. Roy. Astron. Soc.* **182**, 147 (1978).
- [48] E. FERMI, *Phys. Rev.* **75**, 1169 (1949).
- [49] L. O. DRURY, *Contemp. Phys.* **35**, 231 (1994).
- [50] M. NAGANO and A. A. WATSON, *Rev. Mod. Phys.* **72**, 689 (2000).
- [51] R. ALOISIO, V. BEREZINSKY, P. BLASI, and S. OSTAPCHENKO, *Phys. Rev.* **D77**, 025007 (2008).
- [52] P. BLASI, *Mod. Phys. Lett.* **A20**, 3055 (2005).
- [53] L. N. EPELE and E. ROULET, *JHEP* **10**, 009 (1998).
- [54] F. W. STECKER and M. H. SALAMON, *Astrophys. J.* **512**, 521 (1999).
- [55] J. W. CRONIN, *Nucl. Phys. Proc. Suppl.* **138**, 465 (2005).

- [56] R. ENGEL, Talk presented in the International School on Astroparticle Physics, Belgirate, Italy, 2005.
- [57] F. AHARONIAN et al., *Nature*. **432**, 75 (2004), astro-ph/0411533.
- [58] A. HILLAS, *J. Phys.* **G31**, R95 (2005).
- [59] C. T. HILL, *Nucl. Phys.* **B224**, 469 (1983).
- [60] V. BEREZINSKY, M. KACHELRIESS, and A. VILENKIN, *Phys. Rev. Lett.* **79**, 4302 (1997).
- [61] R. ALOISIO, V. BEREZINSKY, and M. KACHELRIESS, *Phys. Rev.* **D69**, 094023 (2004).
- [62] J. R. ELLIS, V. E. MAYES, and D. V. NANOPOULOS, *Phys. Rev.* **D74**, 115003 (2006).
- [63] T. J. WEILER, *Astroparticle Physics* **11**, 303 (1999).
- [64] D. FARGION, B. MELE, and A. SALIS, *Astrophys. J.* **517**, 725 (1999).
- [65] M. RISSE and P. HOMOLA, *Mod. Phys. Lett.* **A22**, 749 (2007), astro-ph/0702632.
- [66] J. ABRAHAM et al., *Astropart. Phys.* **29**, 243 (2008).
- [67] J. ABRAHAM et al., *Phys. Rev. Lett.* **100**, 211101 (2008).
- [68] BLÜEMER, J. AND KAMPERT, K. H., *Phys. Blätter* **56 (3)**, 39 (2000).
- [69] F. A. AHARONIAN and J. W. CRONIN, *Phys. Rev.* **D50**, 1892 (1994).
- [70] J. ABRAHAM et al., *Astropart. Phys.* **29**, 188 (2008).
- [71] T. GAISSER, *Cosmic Ray and Particle Physics*, Cambridge University Press, 1990.
- [72] R. ULRICH, Measurement of the Proton-air Cross Section using Hybrid Data of the Pierre Auger Observatory, PhD thesis, GAP-2008-004.
- [73] C. GRUPEN, *Astroparticle Physics*, Springer, 2005.
- [74] T. BERGMANN, *PhD thesis, Wissenschaftliche Berichte FZKA-7354* (2007).
- [75] B. ROSSI and K. GREISEN, *Rev. Mod. Phys.* **13**, 240 (1941).
- [76] J. ALVAREZ-MUNIZ, R. ENGEL, T. GAISSER, J. ORTIZ, and T. STANEV, *Phys. Rev.* **D66**, 033011 (2002), astro-ph/0205302.
- [77] D. HECK, private communication.
- [78] J. BLUEMER, R. ENGEL, and J. R. HOERANDEL, (2009), astro-ph.HE/arXiv:0904.0725.
- [79] G. NAVARRA, Prepared for 28th International Cosmic Ray Conferences (ICRC 2003), Tsukuba, Japan, 31 Jul - 7 Aug 2003.
- [80] M. AGLIETTA et al., *Astropart. Phys.* **21**, 223 (2004).
- [81] M. AGLIETTA et al., *Astropart. Phys.* **10**, 1 (1999).
- [82] M. AMENOMORI et al., *Phys. Rev.* **D62**, 072007 (2000).
- [83] M. AMENOMORI et al., Prepared for 28th International Cosmic Ray Conferences (ICRC 2003), Tsukuba, Japan, 31 Jul - 7 Aug 2003.
- [84] Y. HAYASHI et al., *Proc. 29th Int. Cosmic Ray Conf., Pune, India*, 243 (2005).
- [85] M. N. DYAKONOV et al., *Proc. 23th Int. Cosmic Ray Conf., Calgary, Canada* **4**, 303 (1993).
- [86] A. BORIONE et al., *Nucl. Instrum. Meth.* **A346**, 329 (1994).
- [87] T. ABU-ZAYYAD et al., *Phys. Rev. Lett.* **84**, 4276 (2000).
- [88] M. AVE et al., *Astropart. Phys.* **19**, 61 (2003).

- [89] M. AVE, J. KNAPP, M. MARCHESINI, M. ROTH, and A. A. WATSON, Prepared for 28th International Cosmic Ray Conferences (ICRC 2003), Tsukuba, Japan, 31 Jul - 7 Aug 2003.
- [90] M. T. DOVA et al., *Astropart. Phys.* **21**, 597 (2004).
- [91] M. AVE, J. A. HINTON, R. A. VAZQUEZ, A. A. WATSON, and E. ZAS, *Phys. Rev. Lett.* **85**, 2244 (2000).
- [92] M. AVE, J. A. HINTON, R. A. VAZQUEZ, A. A. WATSON, and E. ZAS, *Phys. Rev.* **D65**, 063007 (2002).
- [93] K. SHINOZAKI et al., *Astrophys. J.* **571**, L117 (2002).
- [94] K. SHINOZAKI et al., Prepared for 28th International Cosmic Ray Conferences (ICRC 2003), Tsukuba, Japan, 31 Jul - 7 Aug 2003.
- [95] J. ABRAHAM et al., *Astropart. Phys.* **27**, 155 (2007), astro-ph/0606619.
- [96] G. I. RUBTSOV et al., *Phys. Rev.* **D73**, 063009 (2006).
- [97] M. TAKEDA et al., *Astropart. Phys.* **19**, 447 (2003).
- [98] R. U. ABBASI et al., *Phys. Rev. Lett.* **92**, 151101 (2004).
- [99] . J. ABRAHAM et al., (2009), arXiv:0906.2354.
- [100] H. SALAZAR and L. NELLEN, Prepared for 27th International Cosmic Ray Conference (ICRC 2001), Hamburg, Germany, 7-15 Aug 2001.
- [101] X. BERTOU et al., *Nucl. Instrum. Meth.* **A568**, 839 (2006).
- [102] M. AGLIETTA FOR THE PIERRE AUGER COLLABORATION, *Proc. 29th Int. Cosmic Ray Conf., Pune, India* (2005).
- [103] P. GHIA, A compact 3ToT as SD physics trigger for vertical ($\theta < 60^\circ$) showers, GAP-2004-018.
- [104] S. DAGORET-CAMPAGNE, The Central Trigger, User Guide and Reference Manual, GAP-2004-020.
- [105] P. L. GHIA and G. NAVARRA, Analysis of $E_0 \approx 10^{18}$ eV events with the AUGER-EA surface detector, GAP-2003-007.
- [106] E. PARIZOT, I. LHENRY, D. ALLARD, P. GHIA, and G. NAVARRA, First steps towards the definition of a “quality trigger” (T5) for the SD acceptance calculations, GAP-2004-023.
- [107] D. VEBERIČ and M. ROTH, SD Reconstruction, Offline Reference Manual, GAP-2005-035.
- [108] I. MARIŞ, Measurement of the Ultra High Energy Cosmic Ray Flux using Data of the Pierre Auger Observatory, PhD thesis, GAP-2008-026.
- [109] EVENT SELECTION GROUP, The Official SD Event Sselection as of March 2005, GAP-2005-023.
- [110] C. MEDINA and X. BERTOU, Using compact 3 TOT as a starting point for SD reconstruction, GAP-2004-030.
- [111] CDAS SOFTWARE GROUP, Event reconstruction, release v4r4.
- [112] C. BONIFAZI and A. LETESSIER-SELVON, De-biasing the Station Start Time, GAP-2006-050.
- [113] A. M. HILLAS, *Acta Phys. Acad. Sci. Hung.* .
- [114] A. M. HILLAS, *Proc. 12th Int. Cosmic Ray Conf., Tasmania, Australia* **3**, 1001.59 (1971).
- [115] D. NEWTON, J. KNAPP, and A. A. WATSON, *Astropart. Phys.* **26**, 414 (2007).
- [116] M. AVE et al., *Nucl. Instrum. Meth.* **A578**, 180 (2007).

- [117] M. AVE, P. BAULEO, and T. YAMAMOTO, Signal Fluctuation in the Auger Surface Detector Array, GAP-2003-030.
- [118] P. BAULEO, A. CASTELLINA, R. KNAPIK, G. NAVARRA, and J. HARTON, Auger Surface Detector Signal Accuracy – Results from production tanks data, GAP-2004-047.
- [119] D. BARNHILL FOR THE PIERRE AUGER COLLABORATION, *Proc. 29th Int. Cosmic Ray Conf., Pune, India* (2005), astro-ph/0507590.
- [120] T. SCHMIDT, I. C. MARIŞ, and M. ROTH, Fine Tuning of the LDF parameterisation and the Influence on S1000, GAP-2007-106.
- [121] K. KAMATA and J. NISHIMURA, *Prog. Theoret. Phys. Suppl.* **6**, 93 (1958).
- [122] K. GREISEN, *Progress in Cosmic Ray Physics*, volume 3, North-Holland, Amsterdam, 1956.
- [123] I. MARIŞ et al., Messungen von Lateralverteilungen hochenergetischer Luftschauer mit dem Pierre Auger Observatorium, Poster, Zeuthen, 2005.
- [124] M. AGLIETTA, I. D. MITRI, S. MAGLIO, S. MALDERA, I. MARIŞ, D. MARTELLO, G. NAVARRA, and M. ROTH, Recovery of Saturated Signals of the Surface Detector, GAP-2008-030.
- [125] J. ABRAHAM et al., *Phys. Rev. Lett.* **101**, 061101 (2008).
- [126] J. HERSIL, I. ESCOBAR, D. SCOTT, G. CLARK, and S. OLBERT, *Phys. Rev. Lett.* **6**, 22 (1961).
- [127] J. ABRAHAM et al., (2009), arXiv:0906.2189.
- [128] J. A. ABRAHAM et al., (2009), arXiv:0907.4282.
- [129] H. GEMMEKE et al., *IEEE Trans. Nucl. Sci.* **47**, 371 (2000).
- [130] J. BRACK, R. MEYHANDAN, G. HOFMAN, and J. MATTHEWS, *Astropart. Phys.* **20**, 653 (2004).
- [131] C. ARAMO et al., (2005), astro-ph/0507577.
- [132] B. KEILHAUER, J. BLUMER, R. ENGEL, H. O. KLAGES, and M. RISSE, *Astropart. Phys.* **22**, 249 (2004).
- [133] S. Y. BENZVI et al., *Nucl. Instrum. Meth.* **A574**, 171 (2007).
- [134] P. ALLISON FOR THE PIERRE AUGER COLLABORATION, *Proc. 29th Int. Cosmic Ray Conf., Pune, India* (2005).
- [135] S. Y. BENZVI et al., *Astropart. Phys.* **28**, 312 (2007).
- [136] S. BENZVI FOR THE PIERRE AUGER COLLABORATION, *Proc. 30th Int. Cosmic Ray Conf., Merida, Mexico* (2007), astro-ph/0706.3236.
- [137] R. BALTRUSAITIS et al., *Nucl. Instr. Meth* **240**, 420 (1985).
- [138] M. MOSTAFA, Checking the alignment of the FD cameras, GAP-2005-102.
- [139] R. BALTRUSAITIS et al., *Nucl. Instrum. Meth.* **A240**, 410 (1985).
- [140] B. DAWSON, Fluorescence Detector Techniques, GAP-1996-017.
- [141] B. DAWSON et al., Present and Possible Future Implementations of Fluorescence Yield in FD Analysis, GAP-1996-017.
- [142] B. DAWSON, Suggested Improvements for the Treatment of FD Light in the Offline, GAP-2004-055.
- [143] P. SOKOLSKY, “*Introduction to Ultrahigh Energy Cosmic Ray Physics*“, Addison-Wesley, 1989.
- [144] M. UNGER, B. R. DAWSON, R. ENGEL, F. SCHUSSLER, and R. ULRICH, *Nucl. Instrum. Meth.* **A588**, 433 (2008).

- [145] M. NAGANO et al., *Astropart. Phys.* **22**, 235 (2004).
- [146] F. KAKIMOTO et al., *Nucl. Instrum. Meth.* **A372**, 527 (1996).
- [147] M. AVE et al., *Astropart. Phys.* **28**, 41 (2007).
- [148] A. M. HILLAS, *J. Phys. G* **8**, 1461 (1982).
- [149] J. W. ELBERT et al., *Proc. 18th ICRC* (1983).
- [150] M. GILLER, G. WIECZOREK, A. KACPERCZYK, H. STOJEK, and W. TKACZYK, *J. Phys.* **G30**, 97 (2004).
- [151] F. NERLING et al., Description of Cherenkov light production in high-energy air showers, 2005, submitted to *Astro. Part. Phys.*, astro-ph/0506729.
- [152] T.K. GAISSER AND A.M. HILLAS, *Proc. 15th Int. Cosmic Ray Conf., Plovdiv, Bulgaria*, **8**, 353, 1977 .
- [153] Z. CAO et al., *Proc. 28th Int. Cosmic Ray Conf. 2003* .
- [154] H. BARBOSA et al., *Astropart. Phys.* **22**, 159 (2004).
- [155] T. PIEROG et al., *Proc. 29th Int. Cosmic Ray Conf., Pune, India* (2005).
- [156] R. KNAPIK et al., (2007), astro-ph/arXiv:0708.1924.
- [157] M. UNGER, R. ENGEL, F. SCHÜSSLER, and R. ULRICH, Lateral shower light distributions in the Cherenkov-Fluorescence-Matrix Profile Reconstruction, GAP-2008-052.
- [158] T. PIEROG, R. ENGEL, D. HECK, S. OSTAPCHENKO, and K. WERNER, (2007).
- [159] B. R. DAWSON, (2007), astro-ph/arXiv:0706.1105.
- [160] S. A. ET AL, *Nucl. Instrum. Meth.* **A580**, 1485 (2007).
- [161] *Offline Software* , <http://offline.p-ng.si/index.html>.
- [162] *ROOT, the object-oriented data analysis framework* , <http://root.cern.ch>.
- [163] I.C.MARIŞ, F.SCHUESSLER, R.ULRICH, and M. UNGER, Data Summary Trees and Shower Visualization for Reconstructed Auger Events, GAP-2006-081.
- [164] *The Auger Observer* , <http://observer.fzk.de>.
- [165] F. SCHÜSSLER, Measurement of the Energy Spectrum of Ultra-High Energy Cosmic Ray using Hybrid Data of the Pierre Auger Observatory, PhD thesis, GAP-2008-155.
- [166] W. HEITLER, “*The Quantum Theory of Radiation*“, Oxford University Press, 1954.
- [167] T. K. GAISSER, T. J. L. MCCOMB, and K. E. TURVER, In *Kyoto 1979, Proceedings, 16th International Cosmic Ray Conference, Vol. 9*, 275-280.
- [168] J. LINSLEY and A. A. WATSON, *Phys. Rev. Lett.* **46**, 459 (1981).
- [169] J. LINSLEY, *Proc. 15th Int. Cosmic Ray Conf.* **12**, 89 (1977).
- [170] J. ENGEL, T. K. GAISSER, T. STANEV, and P. LIPARI, *Phys. Rev.* **D46**, 5013 (1992).
- [171] T. PIEROG, R. ENGEL, and D. HECK, *Czech. J. Phys.* **56**, A161 (2006).
- [172] M. UNGER, R. ENGEL, F. SCHÜSSLER, and R. ULRICH, Measurement of $\langle X_{max} \rangle$ as a function of Energy, GAP-2007-005.
- [173] E. J. AHN, J. BELLIDO, S. BENZVI, R. ENGEL, F. SCHÜSSLER, R. ULRICH, and M. UNGER, Measurement of the Depth of Shower Maximum of Cosmic Rays above 10^{18} eV, GAP-2009-078.
- [174] R. ULRICH et al., (2009), astro-ph.HE/arXiv:0906.0418.

- [175] B. SMITH, The Mass Composition of Cosmic Rays Above 1 EeV Inferred Using the Spread in Arrival Times of Air Shower Particles, PhD thesis, GAP-2008-161.
- [176] A. CASTELLINA and G. NAVARRA, Separating the electromagnetic and muonic components in the FADC traces of the Auger Surface Detectors, GAP-2006-065.
- [177] X. GARRIDO, A. CORDIER, S.DAGORET-CAMPAGNE, B. KEGL, D. MONNIER-RAGAIGNE, and M. URBAN, Measurement of the number of muons in Auger tanks by the FADC jump counting method, GAP-2007-060.
- [178] R. COY et al., *Astropart. Phys.* **6**, 263 (1997).
- [179] P. YOUNK, LDF parameterisation with the 750 m infill array, GAP-2009-047.
- [180] L. CAZÓN, Modelling the Muon time Distriburion in Extensive Air Showers, PhD thesis, Universidad de Santiago de Compostela, 2004.
- [181] E. ARMENGAUD, O. DELIGNY, J. LAMBLIN, and G. MAURIN, Fitting a variable radius of curvature, GAP-2003-108.
- [182] D. BARNHILL, Composition Analysis of Ultrahigh Energy Cosmic Rays Using the Pierre Auger Observatory Surface Detector, PhD thesis, GAP-2005-082.
- [183] M. HEALY, D. BARNHILL, K. ARISAKA, J. LEE, and P. BOGHRAT, A Study of composition trends using rise time and curvature data, GAP-2006-092.
- [184] H. DUC, A Study of the Time Spread of the Signals Recorded with the Water Tanks of the Pierre Auger Observatory, Mphil thesis, University of Leeds, 2005.
- [185] K. S. CABALLERO MORA, M. ROTH, I. C. MARIŞ, and T. SCHMIDT, *J. Phys. Conf. Ser.* **116**, 012007 (2008).
- [186] M. T. DOVA et al., (2009), astro-ph.IM/arXiv:0903.1755.
- [187] F. ARQUEROS, D. G. PINTO, M. MONASOR, M.T.DOVA, A. MARIAZZI, and H. WAHLBERG, Inferring X_{max} from asymmetry in risetime, GAP-2008-179.
- [188] H. WAHLBERG, Prepared for 31st International Cosmic Ray Conference (ICRC 2009), Łódź, Poland, 7-15 Jul 2009.
- [189] C. WILEMAN, The spread in the Arrival Times of Particles in Air-Showers for Photon and Anisotropy Searches above 10 EeV, PhD thesis, GAP-2008-160.
- [190] A. LÓPEZ-AGUERA and G. RODRIGUEZ, Electronic Noise Control Protocole, GAP-2004-058.
- [191] C. FRACCHIOLLA, C. BONIFAZI, A. LETESSIER-SELVON, and O. B. BIGAS, Angular Resolution with the Super-Hexagon, GAP-2008-095.
- [192] A. A. WATSON and J. G. WILSON, *J. Phys.* **A7**, 1199 (1974).
- [193] E. M. PUGH and G. H. WILSON, “*The analysis of physical measurements*“, Addison-Wesley, 1966.
- [194] D. HECK, J. KNAPP, J. CAPDEVIELLE, G. SCHATZ, and T. THOUW, *FZKA-6019* (1998).
- [195] *CORSIKA web page*, <http://www-ik.fzk.de/corsika>.
- [196] S. AGOSTINELLI et al., *Nucl. Instrum. Meth.* **A506**, 250 (2003).
- [197] J. ALLISON et al., *IEEE Trans. Nucl. Sci.* **53**, 270 (2006).
- [198] P.BILLOIR, P. D. SILVA, and X. BERTOU, Checking the origin of the Asymmetry of the Surface Detector signals., GAP-2002-074.
- [199] B. D. HIEU and A. WATSON, Analysis of the risetime and its uncertainty for events recorded by the surface detector in the Pierre Auger Observatory, GAP-2005-April.

- [200] R. ENGEL FOR THE PIERRE AUGER COLLABORATION, *Proc. 30th Int. Cosmic Ray Conf., Merida, Mexico* (2007), arXiv:0706.1921v1 [astro-ph].
- [201] A. CASTELLINA FOR THE PIERRE AUGER COLLABORATION, *Proc. 31st Int. Cosmic Ray Conf., Łódź, Poland* (2009), arXiv:0906.2189 [astro-ph].
- [202] R. WALKER and A. A. WATSON, *J. Phys.* **G7**, 1297 (1981).
- [203] D. ALLARD FOR THE PIERRE AUGER COLLABORATION, *Proc. 29th Int. Cosmic Ray Conf., Pune, India* (2005).
- [204] J. ABRAHAM et al., (2009), arXiv:0906.2319.
- [205] N. N. KALMYKOV and S. S. OSTAPCHENKO, *Phys. Atom. Nucl.* **56**, 346 (1993).
- [206] S. S. OSTAPCHENKO, *Nucl. Phys. Proc. Suppl.* **151**, 143 (2006).
- [207] T. PIEROG and K. WERNER, *Phys. Rev. Lett.* **101**, 171101 (2008).
- [208] E.-J. AHN, R. ENGEL, T. K. GAISSER, P. LIPARI, and T. STANEV, *Phys. Rev.* **D80**, 094003 (2009).
- [209] M. UNGER, private communication.
- [210] M. Z. F. SCHMIDT, J. KNAPP, Results from the Simulation of an Unthinned Proton Shower at $5 * 10^{18}$ eV, GAP-2005-095.
- [211] S. OSTAPCHENKO, *Phys. Lett.* **B636**, 40 (2006), hep-ph/0602139.
- [212] G. BATTISTONI et al., *AIP Conf. Proc.* **896**, 31 (2007).
- [213] W. NELSON, H. HIRAYAMA, and D. ROGERS, *SLAC-0265* (1985).
- [214] J. OEHLSCHLAEGER and I. MARIŞ, private communication.
- [215] R. CARUSO FOR THE PIERRE AUGER COLLABORATION, *Proc. 29th Int. Cosmic Ray Conf., Pune, India* .

Acronyms

ADST	Advanced Data Summary Tree
AERA	Auger Engineering Radio Array
AGN	Active Galactic Nuclei
AMIGA	Auger Muons and Infill for the Ground Array
asl	above sea level
CDAS	Central Data Acquisition System
CLF	Central Laser Facility
CMB	Cosmic Microwave Background
CORSIKA	COsmic Ray SIMulations for KAscade
DSAs	Diffusive Shock Acceleration
EAS	Extensive Air Showers
FADC	Flash Analog Digital Converter
FD	Fluorescence Detector
FOV	Field of view
GPS	Global Positioning System
GZK	Greisen Zatsepin Kuzmin
HEAT	High Elevation Auger Telescopes
HV	High Voltage
IBR	Infrared Background Radiation
KASCADE	KARlsruhe Shower Core and Array DETector
LDF	Lateral Distribution Function
LED	Light-Emitting Diode
LHC	Large Hadron Collider
LIDAR	Light Detection and Ranging
LTP	Lateral Trigger Probability
NIST	National Institute of Standards and Technology
NKG	Nishimura Kamata Greisen lateral distribution function
PLD	Programmable Logic Device

PMT	PhotoMultiPlier
SD	Surface Detector
SDP	Shower Detector Plane
SHDM	Super Heavy Dark Matter
SNRs	Super Nova Remnants
SPR	Single Particle Response
T1	local station trigger
T2	second station trigger
T3	second level lowest Central Data Acquisition System (CDAS) trigger
T4	physics trigger
T5	quality trigger
TD	Topological Defects
Thr2	second level threshold trigger
ToT	Time Over Threshold trigger
UHECR	Ultra High Energy Cosmic Ray
UV	Ultra Violet
VAOD	Vertical Aerosol Optical Depth
VCT	Vertical and Central Through-going muon
VEM	Vertical Equivalent Muon
4C1	configuration of one station with 3 close neighbors

Appendix A

Validation of risetime results for data used in Δ_{1000} analysis

FADC trace structure Since the time when risetime studies of measurement uncertainty calculation and asymmetry correction (Chapter 4) were performed, the FADC traces have been restructured in the Offline software framework [161]. It may affect the value of risetime. The new structure is used for the Δ_{1000} analysis, therefore the observation of differences between both kinds of risetimes is important. A set of traces containing the old and the new FADC structure are used for this purpose. Figure A.1 show the relative difference of risetimes for the range of zenith angles used in the Δ_{1000} analysis ($\sec\theta \in [1.0, 1.4]$). Since the difference is $\sim 2\%$ the use of the current risetime results for Δ_{1000} analysis is justified. A more detailed verification concerning the measurement uncertainty is shown in the next paragraph.

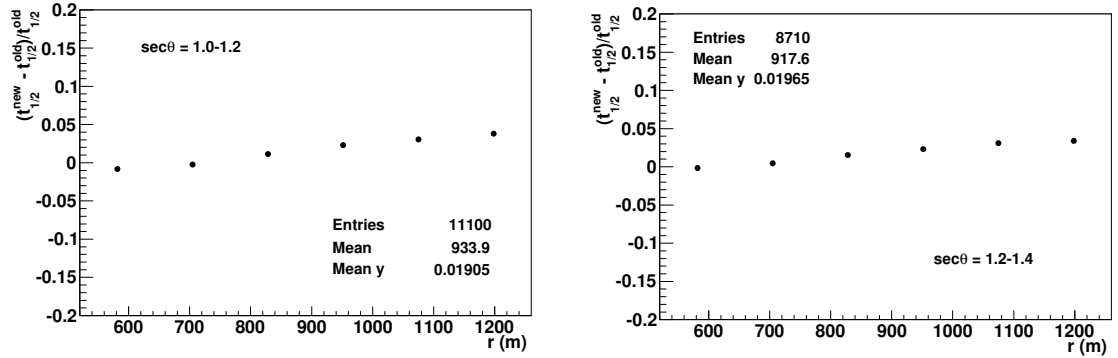
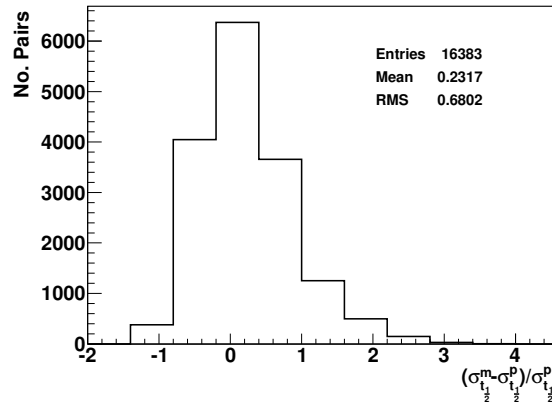
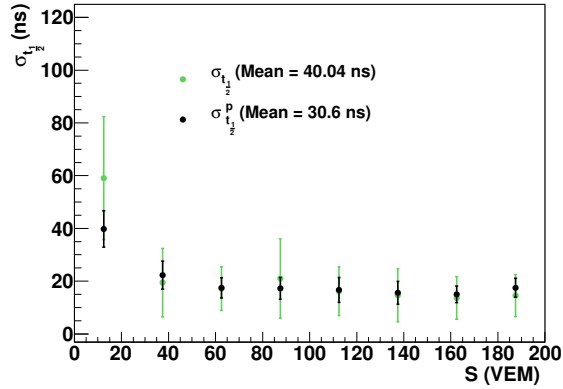


Figure A.1: The relative difference between risetimes from old and new structure of FADC trace in the range $\sec\theta \in [1.0, 1.4]$.

Measurement uncertainty In order to verify the use of the measurement uncertainty, $\sigma_{t_{1/2}}$, calculated in Chapter 4, the average fractional difference with respect to the parameterisation, $\sigma_{t_{1/2}}^p$, is analyzed for a set of data fulfilling the conditions for the Δ_{1000} analysis. Events must have energies higher than 1 EeV and $\sec\theta \in [1.0, 1.4]$, containing at least one station with $S > 15$ VEM located between 600 m and 1200 m. According to Fig. A.2(a), the distribution is centred around 0. Figure A.2(b) shows good agreement between expected and measured value of $\sigma_{t_{1/2}}$ within the spread. No systematic bias with S, r and E is observed (see Fig. A.3). The bias with $\sec\theta$ already found in Chapter 4 is reduced as shown in Fig. A.3(d). The set of data presents the same behavior than the data used for obtaining $\sigma_{t_{1/2}}^p$, meaning that the use of parameterised $\sigma_{t_{1/2}}$ for Δ_{1000} analysis is valid.

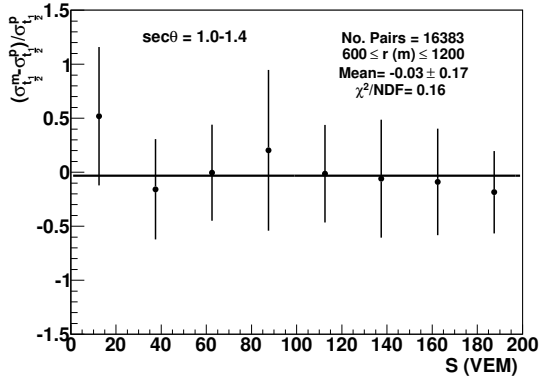


(a)

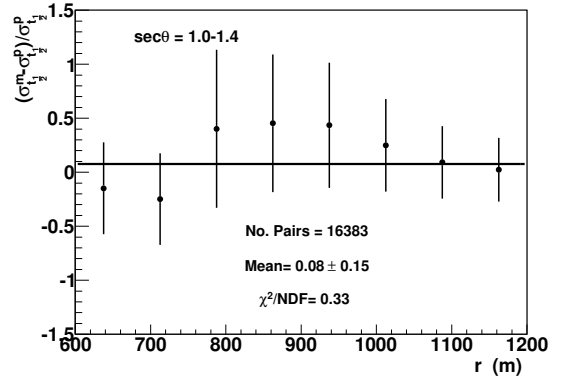


(b)

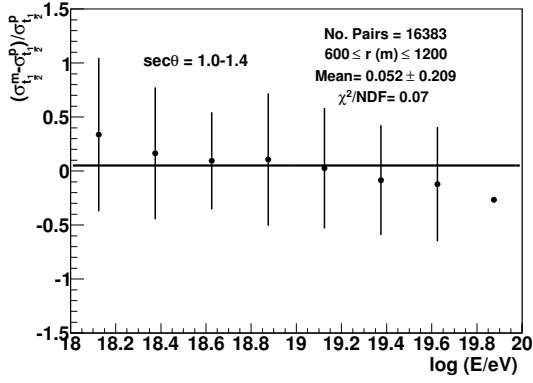
Figure A.2: (a) The average fractional difference in $\sigma_{t_{1/2}}$ for data fulfilling conditions for Δ_{1000} analysis. (b) Comparison between measured and expected value of $\sigma_{t_{1/2}}$.



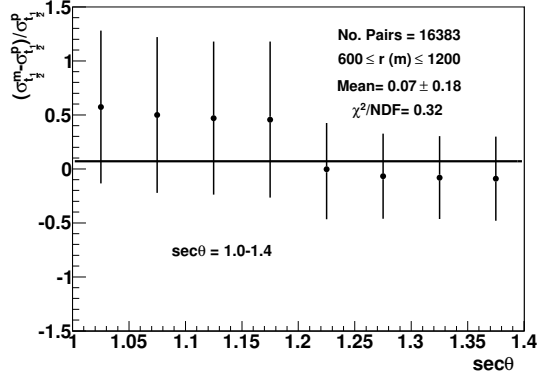
(a)



(b)



(c)



(d)

Figure A.3: The average fractional difference in $\sigma_{t_{1/2}}$ as a function of : (a) signal, (b) distance to the core, (c) energy of the shower and (d) $\sec\theta$ for data fulfilling conditions for Δ_{1000} analysis.

Appendix B

Information about simulated showers for studies of Δ_{1000} parameter

Monte Carlo showers simulated with CORSIKA for comparison of results about Δ_{1000} parameter described in Chapter 6, before application of required cuts.

Primary	No.Ev	Energy (eV)					
		$1 \cdot 10^{18}$	$3.16 \cdot 10^{18}$	$1 \cdot 10^{19}$	$3.16 \cdot 10^{19}$	$1 \cdot 10^{20}$	$3.16 \cdot 10^{20}$
SD							
proton	5043	700	600	2850	240	420	233
iron	5055	700	600	2850	240	435	230

Table B.1: Number of available simulated air showers before application of cuts required for Δ_{1000} calculaton according to the energy.

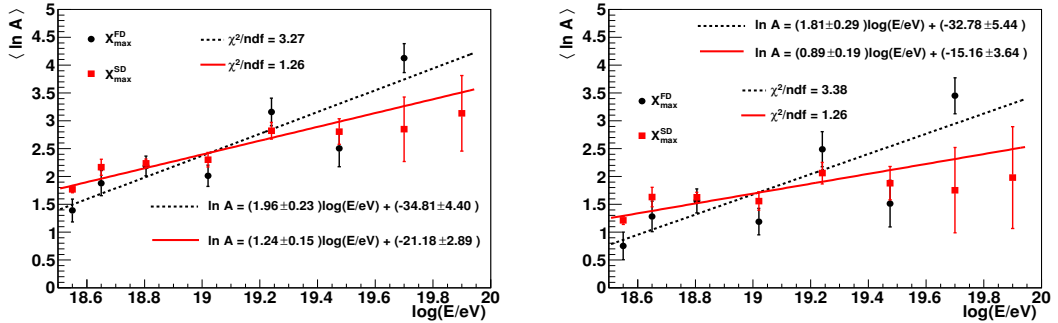
Primary	sec θ								
	1.	1.1	1.26	1.3	1.4	1.5	1.7	1.9	
SD									
proton	264	399	396	396	2390	400	398	400	
iron	278	398	397	397	2390	398	399	398	

Table B.2: Number of available simulated air showers before application of cuts required for Δ_{1000} calculaton according to the zenith angle.

Appendix C

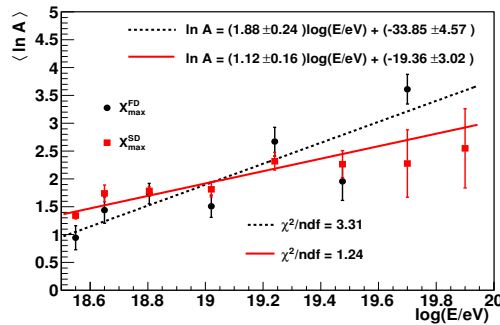
Comparison of results of $\langle \ln A \rangle$

Comparisons of the mean logarithmic mass of the sample of hybrid events used for obtaining the calibration of Δ_{1000} with X_{max}^{FD} , with the results of the whole SD sample is shown in Fig. C.1. The FD results are calculated using the X_{max}^{FD} and the SD ones are calculated using the X_{max}^{SD} with reference to three hadronic interaction models. The FD sample shows also an increase of the mass with the energy but at a faster rate ($\frac{d \ln A}{d \log E} = 1.96 \pm 0.23 \text{ decade}^{-1}$, $\frac{d \ln A}{d \log E} = 1.81 \pm 0.29 \text{ decade}^{-1}$ and $\frac{d \ln A}{d \log E} = 1.88 \pm 0.24 \text{ decade}^{-1}$ for EPOS, QGSJET II and SIBYLL 2.1 respectively) in comparison with the SD one.



(a) Epos 1.99

(b) QGSJET II



(c) SIBYLL 2.1

Figure C.1: The mean logarithmic mass, using the X_{max}^{SD} parameter compared with the one obtained using X_{max}^{FD} with reference to three different hadronic interaction models.

Acknowledgements

I would like to thank Prof. Dr. Johannes Blümer for supervising this work and for his support as referee. I thank Prof. Dr. Günter Quast for being co-referee of this dissertation. I would specially like to thank Dr. Markus Roth for giving me the opportunity to join the Karlsruhe group within the Pierre Auger Collaboration and for patiently supporting and advising my work during my whole stay in Karlsruhe.

I want to express my gratitude to my colleagues for fruitful discussions, support and ideas. The people who have worked at Karlsruhe, Dr. Lorenzo Cazón Boado, Dr. Till Bergmann, Talianna Schmidt, Dr. Ioana Mariş, Dr. Fabian Schüssler, Dr. Ralf Ulrich, Dr. Jürgen Oehlschläger, Dr. Klaus Bekk, Dr. Ralph Engel, Dr. Hans-Otto Klages, Dr. Dieter Heck, Dr. Tanguy Pierog, Dr. Danays Morejón González, Dr. Alessio Tamburro, Dr. Dariusz Góra, Dr. Juan Carlos Arteaga Velázquez, Dr. Inés Valiño Rielo, Dr. Hans Dembinski, Dr. Andrey Konstantinov, Dr. Francesco Salamida, Dr. Bianca Keilhauer, Steffen Müller, Fatima Messar, Pablo Robert, Marco Haag, Heike Bolz and Sabine Bucher. I am specially grateful to Dr. Michael Unger for careful revisions and discussions of this work. I thank the people who helped me correct the first versions of my manuscript, Dr. Tom Paul, Jan Weseler, Dr. Donghwa Kang, Dr. Radomir Smida, Detlef Maurel and Dr. Javier González.

The people who have worked in the Pierre Auger Collaboration, Dr. Christopher Wileman, Dr. Benjamin Smith, Dr. Arnulfo Zepeda, Dr. Gonzalo Rodríguez Fernández, Dr. José Valdés Galicia and the regular attenders to the Mass Composition telephone meeting, specially Dr. María Teresa Dova and Prof. Alan Watson. I would like to express my gratitude to Dr. Lukas Nellen for introducing me to the field of cosmic rays and for his continuous support.

This work would not have been possible without the financial support of DAAD (Deutscher Akademischer Austausch Dienst) and CONACyT (Consejo Nacional de Ciencia y Tecnología). I am also grateful to my Alma Mater UNAM (Universidad Nacional Autónoma de México) for giving me the opportunity to open my mind to the universal knowledge.

Many thanks to my parents Enrique Caballero Valencia and María Teresa Mora Valenzuela, my sister Wendolyne Caballero Mora and my friends who have continuously provided support and encouragement during my PhD adventure in Germany.